New Layered Materials and Functional Nanoelectronic Devices

Jaeeun Yu

Submitted in partial fulfillment of the
requirements for the degree of
Doctor of Philosophy
in the Graduate School of Arts and Sciences

COLUMBIA UNIVERSITY

2018

ABSTRACT

New Layered Materials and Functional Nanoelectronic Devices

Jaeeun Yu

This thesis introduces functional nanomaterials including superatoms and carbon nanotubes (CNTs) for new layered solids and molecular devices. Chapters 1-3 present how we incorporate superatoms into two-dimensional (2D) materials. Chapter 1 describes a new and simple approach to dope transition metal dichalcogenides (TMDCs) using the superatom $Co_6Se_8(PEt_3)_6$ as the electron dopant. Doping is an effective method to modulate the electrical properties of materials, and we demonstrate an electron-rich cluster can be used as a tunable and controllable surface dopant for semiconducting TMDCs via charge transfer. As a demonstration of the concept, we make a p-n junction by patterning on specific areas of TMDC films.

Chapter 2 and Chapter 3 introduce new 2D materials by molecular design of superatoms. Traditional atomic van der Waals materials such as graphene, hexagonal boron-nitride, and TMDCs have received widespread attention due to the wealth of unusual physical and chemical behaviors that arise when charges, spins, and vibrations are confined to a plane. Though not as widespread as their atomic counterparts, molecule-based layered solids offer significant benefits; their structural flexibility will enable the development of materials with tunable properties. Chapter 2 describes a layered van der Waals solid self-assembled from a structure-directing building block and C_{60} fullerene. The resulting crystalline solid contains a corrugated monolayer of neutral fullerenes and can be mechanically exfoliated. Chapter 3 describes a new method to functionalize electroactive superatoms with groups that

can direct their assembly into covalent and non-covalent multi-dimensional frameworks. We synthesized $Co_6Se_8[PEt_2(4\text{-}C_6H_4COOH)]_6$ and found that it forms two types of crystalline assemblies with $Zn(NO_3)_2$, one is a three-dimensional solid and the other consists of stacked layers of two-dimensional sheets. The dimensionality is controlled by subtle changes in reaction conditions.

CNT-based field-effect transistor (FETs), in which a single molecule spans an oxidatively cut gap in the CNT, provide a versatile, ground-state platform with well-defined electrical contacts. For statistical studies of a variety of small molecule bridges, Chapter 4 presents a novel fabrication method to produce hundreds of FETs on one single carbon nanotube. A large number of devices allows us to study the stability and uniformity of CNT FET properties. Moreover, the new platform also enables a quantitative analysis of molecular devices. In particular, we used CNT FETs for studying DNA-mediated charge transport. DNA conductance was measured by connecting DNA molecules of varying lengths to lithographically cut CNT FETs.

Contents

List of Figures

List of Tables

Acknowledgments

First and foremost, I would like to thank my advisor, Prof. Colin Nuckolls. I am very fortunate being in the Nuckolls group. I have had great opportunities to collaborate other research groups in Physics and Engineering Departments. It was a valuable experience for me to learn cutting-edge science and technology as well as to explore my research interests. I also want to thank him for his patience. I couldn't have come this far without his support and patience. Thank you.

I would like to thank my committee members, Prof. Jonathan Owen, Dr. Michael Steigerwald, Prof. Xavier Roy, and Prof. James Hone. Jon and Mike are on my graduate committee since my 1st year of Columbia. I want to thank them for their advice and support in the second year defense and the original research proposal. Mike and Xavier are leaders in the superatom team. I am fortunate to have opportunities to work with you and your group on applications of superatoms. Thanks to Jim, I learned about two-dimensional semiconducting materials. The Hone group is one of the leading group in the field, and Jim and his group allow other researchers (including me) to work in their lab as well as share their knowledge and techniques. I want to thank Jim and all his group members for their consideration.

I participated in a collaborative project with Prof. Philip Kim and Dr. Chul-Ho Lee, and I would like to thank Philip and Chul-Ho. As a Korean, it has been a great pleasure working with Philip. Chul-Ho is the one who taught me from exfoliation of 2D materials to fabricate the complicated heterostructure devices and to analyze the electrical data. Chul-Ho and his wife Hye-Kyoung are generous and kind people. Thanks so much.

I spent five and a half years in Nuckolls group. I want to thank all of the group members I was with during these years. As a big group including interdisciplinary collaborating groups, I can't name all of my colleagues, but I would like to mention some of them whom I worked with. Thanks to Christine, Christopher, Anouck, Bonnie, Alexandra, and Dan for superatom projects and Bumjung, Delphine, and Qizhi for CNT projects. I am really lucky to work with all of you on exciting scientific projects. I want to thank Dr. Delphine Bouilly for her support and advice. Delphine is one of the most optimistic people that I have known. She helped me going through this Ph.D. program. I would also like to thank Sunwoo, Daniel, and Ghidewon in Hone lab for their help.

I would like to thank our group coordinators - KO Campbell, Liz Powell, and Ryan Hastie - and Chemistry Department staff- Alix Lamia, Dani Farrell, and Alison Doyle - for their help and consideration. I would particularly like to thank Ryan for all of her kindness and support. I would also like to thank CNI cleanroom team members - Dr. Nava Ariel-Sternberg, James Vichiconti, Nirit Porecki-Shamay, and Melody Gonzalez. It has been an exceptional experience for me to work in a new cleanroom. I am happy to help the CNI team as well as users. I want to thank James for teaching me all his knowledge and skills to install equipment.

Over the past almost six years, I have been acquainted with many Korean researchers from SK to JS. I am truly thankful to all of you. In particular, I want to express my gratitude to JH Lee, J. Kang, J. Woo, and H. Min. I feel very lucky having such good friends. I would also love to thank my classmates - Archana, Andrés, and Theta whom I spent a lot of time and have been through this program together. Thank you all for being very supportive.

Finally, my deepest thank to my family - grandfather S. Jeong, grandmother J. Choi, father S. Yoo, mother Y. Jeong, sister Jackie, and aunt K. Jeong - for all of their moral and financial support. I would love to give a special thank to my grandfather and grandmother for their unconditional love to their children and grandchildren. Love you all.

Jaeeun (Jen) Yu
May 2017

For my family.

Chapter 1

Patterning superatom dopants on transition metal dichalcogenides[1]

1.1 Introduction

In this chapter we describe a new chemical strategy to chemically dope two-dimensional (2D) transition metal dichalcogenides (TMDCs) using a metal chalcogenide molecular cluster as the dopant.

Metal chalcogenide molecular clusters are attractive building blocks for making new electronic materials because of their diversity and atomic definition.[1, 2] They can act as nanoscale building blocks, combining with C_{60} and other electron-poor building blocks to form superatomic solid-state compounds.[3–5] In 2013, Roy *et al.* have presented the new

---

[1] This chapter is reproduced from the work published in Nano Lett. **16**, 3385 (2016). Copyright 2016, American Chemical Society. Device fabrication and characterization were performed by myself with assistance from Chul-Ho Lee and Minyong Han.

type of solid-state material formed with three clusters and C_{60} via charge transfer (Figure 1.1a).[3] For example, $Co_6Se_8(PEt_3)_6$ and C_{60} assembled into a binary solids with molar ratio of 1:2, which is a relative structure of the ionic solids (CdI_2) as depicted in Figure 1.1b. Raman spectroscopy characterized the charge state of each building block. The result showed that the cluster donates two electrons to two neighboring C_{60}, thus resulting in a compound as $[\text{cluster}^{2+}][C_{60}^{-}]_2$. The cluster behaves as an individual atom in a binary solid-state compound, and it has been termed as a superatom here.

Moreover, the electronic states and the capability of doping can be easily tuned in superatoms by changing the metal atoms, the chalcogen atoms, and the capping ligands.[5, 9, 10] Figure 1.2 shows that redox potentials are modulated by substituting the chalcogen atoms and the phosphine ligands. The arrow in Figure 1.2 indicates that charge transfer occurs between cobalt chalcogenide clusters and iron oxide acceptors.

Doping plays a vital role in electronic materials as an effective method to modulate the electrical properties of materials. Whereas traditional 3D semiconductors are doped by introducing atomic substitutions in the crystalline lattice,[11] doping of 2D materials has been achieved via three routes.[12] Figure 1.3 demonstrates examples of three doping methods for graphene. Substitutional doping is to add the electron donor or acceptor atoms at carbon sites in graphene (*e.g.* B, N, or P). The well-known example of covalent functionalization of graphene is graphene oxide (GO) which is oxidatively derived from graphite. The hydroxyl groups in GO enable further reactions to have various functional groups in the nanosheet. These two methods involve covalent modification and they are often irreversible processes.

In contrast, surface charge transfer doping method is realized from the interaction between dopants and 2D materials. Chemical dopants are physically adsorbed on graphene

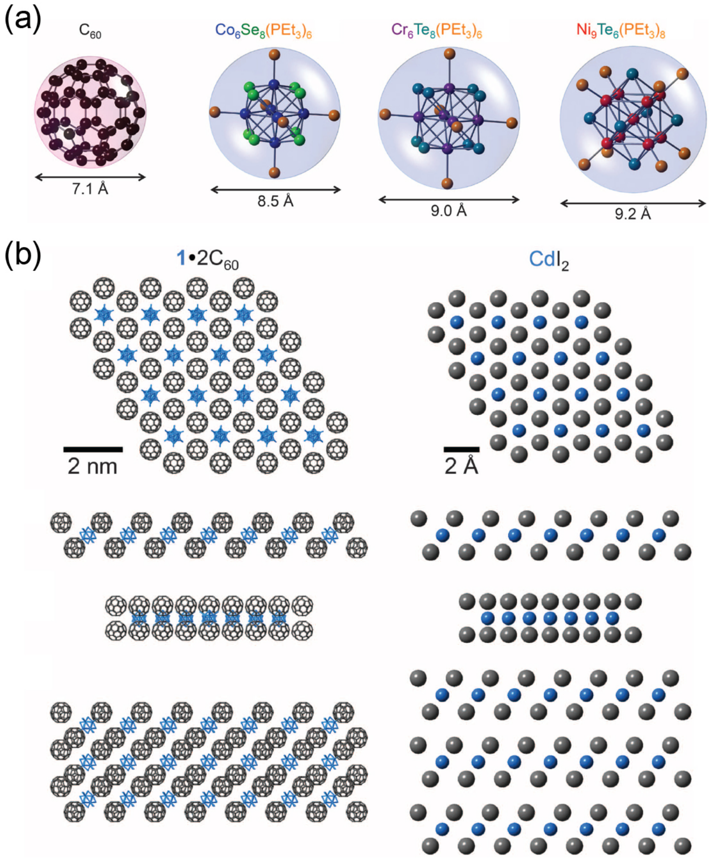

Figure 1.1: (a) Molecular structures of the superatoms as determined by single-crystal X-ray diffraction (SCXRD). (b) Top-down and edge-on views of $[Co_6Se_8(PEt_3)_6][C_{60}]_2$ and CdI_2. The ethyl groups on the phosphine ligands are omitted to clarify the view. Adapted from Ref. [3]

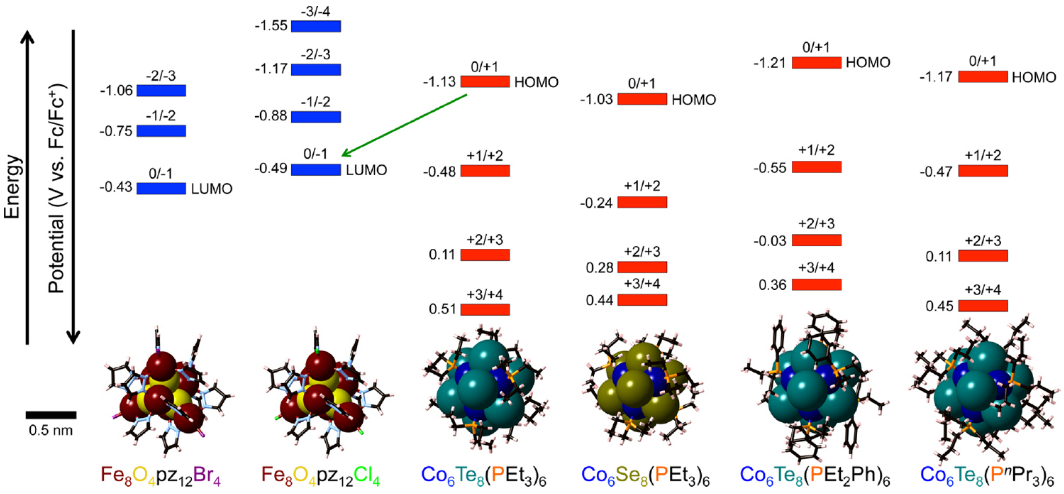

Figure 1.2: Molecular structures and reduction potentials of various superatoms as determined by SCXRD and cyclic voltammetry (CV), respectively. The clusters are illustrated on the same size scale. Adapted from Ref. [5]

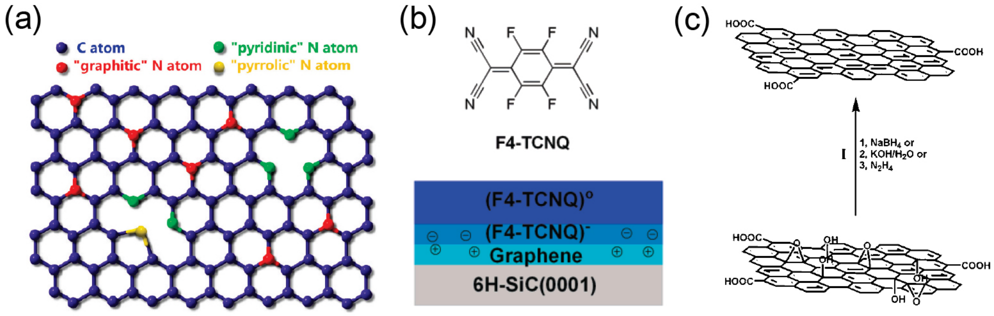

Figure 1.3: Chemical doping methods for graphene: (a) substitutional doping - N-doped graphene, (b) surface charge transfer doping - F4-TCNQ deposited on graphene, and (c) Covalent functionalization - reduction of graphene oxide to graphene. Adapted from Ref. [6–8]

Table 1.1: Molecular n-doping methods for 2D materials.

2D materials	**Graphene**		**WS_2**		**MoS_2**		**WSe_2**	
Processing	CVD	low pressure CVD	mechanical exfoliation		mechanical exfoliation		mechanical exfoliation	
Layer thickness	monolayer	monolayer	multilayer (~5 nm)	multilayer (3.5-5 nm)	trilayer	trilayer	monolayer to ~10 nm	
Dopants	N-DMBI[a]	ethylene amines[b]	LiF	Cl	K	benzyl viologen	SiN_x	PPh_3
Doping process	spin-coated	vapor-phase	immersed in solution	immersed in DCE[c]	K vapor in vacuum	immersed in solution	plasma enhanced CVD	spin-coated
Air sensitivity	stable (one month)	stable (90 °C 20 min)	stable (2 weeks)		reversible	stable	stable	stable (8 days)
Carrier concentration (cm^{-2})	$\sim 1 \times 10^{13}$	$\sim 1 \times 10^{13}$	$\Delta V_{th} = 20$ V	6.0×10^{11}	$\sim 1 \times 10^{13}$	1.2×10^{13}	7.4×10^{11} - 9.5×10^{13}	8×10^{11}
Contact resistance			$0.9\ k\Omega \cdot \mu m$	$0.7\ k\Omega \cdot \mu m$		$1.1\ k\Omega \cdot \mu m$		
Mobility ($cm^2/V{\cdot}s$)	>1000 (electron)	~2000 (electron)	34	60	~25	24.7	~70	18.9
Device applications	back-gated FET (SiO_2)		back-gated FET (SiO_2)		back-gated FET (SiO_2) top-gated FET (ZrO_2)		back-gated FET (SiO_2)	photodetector
Reference	[13]	[14]	[15]	[16]	[17]	[18]	[19]	[20]

---

[a] (4-(1,3-dimethyl-2,3-dihydro-1H-benzoimidazol-2-yl)phenyl)dimethylamine

[b] triethylenetetramine, tetraethylenepentamine, pentaethylenehexamine, and poly(ethyleneimine)

[c] 1,2-dichloroethane

and charge transfer occurs in the interface. Surface transfer doping is the most widely used method because it has a wide range of deposition techniques and dopants with complementary electronic states towards various semiconductors.[21, 22] Table 1.1 summarizes details of charge transfer n-doping techniques for 2D materials from literature. For instance, potassium metal,[17] benzyl viologen,[18] and silicon nitride (SiN_x)[19] have been used to dope TMDCs such as MoS_2 and WSe_2. These surface-adsorbed dopants were able to dope materials up to the degenerate level. Superatoms with tunable electronic properties as shown in Figure 1.2 would be the key to achieving carrier doping in a controlled manner.

Here we explore how an electron-rich metal chalcogenide molecular cluster can be used as a tunable and controllable surface dopant for semiconducting TMDCs via charge transfer. To demonstrate the utility of this method, we fabricate a p-n junction by spatially confining the area of the WSe_2 that is doped. Lateral p-n junctions in WSe_2 have been created using electric field effects from multiple gate electrodes on the channel.[23, 24] We further find that we can passivate and stabilize the doped films from the ambient by covering them with a self-assembled hydrocarbon layer.

1.2 Electron doping of MoS_2 and WSe_2

In this study, we used the electron-rich octahedral superatom $Co_6Se_8(PEt_3)_6$ as an electron dopant[3] for MoS_2 and WSe_2. To study the doping process, we fabricated back-gated field-effect transistors (FETs) from mechanically exfoliated mono- or few-layer MoS_2 and WSe_2 with channel lengths of $1 - 2$ μm.[25] To create the devices we first exfoliated the TMDC layers to a Si substrate, whose surface is passivated with a 285 nm thick layer of thermally

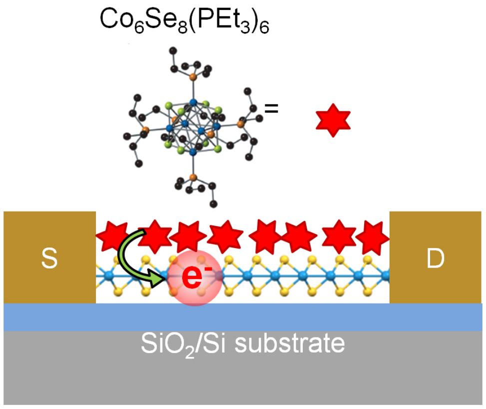

Figure 1.4: Schematic of a back-gated TMDC FET doped with electron-rich molecular clusters, $Co_6Se_8(PEt_3)_6$.

grown SiO_2, and then determined the exact number of MoS_2 and WSe_2 atomic layers by photoluminescence (PL) and Raman spectroscopy.[26–28] We patterned source and drain electrodes on the TMDC films using e-beam lithography. We created Al/Cr/Au (40/5/40 nm) electrodes for MoS_2[29] and Pd/Au (20/30 nm) electrodes for WSe_2.[30] To dope the 2D semiconductor, we immersed the device into a toluene solution of $Co_6Se_8(PEt_3)_6$ (0.01 – 1 mg/mL) for 10 min, followed by rinsing with fresh toluene. Figure 1.4 displays a schematic of a superatom-doped device. Atomic force microscopy (AFM) strongly suggests that the molecular cluster is adsorbed on the surface of the van der Waals materials (Figure 1.5). For instance, the trilayer WSe_2 film was ∼2 nm in thickness before doping and the surface roughness became ∼1 to 2 nm upon superatom adsorption, corresponding to the diameter of the superatoms.[5] The electrical properties of FETs were measured at room temperature in a N_2-filled glovebox for each TMDC film, before and after superatom doping.

Figure 1.6a displays typical transfer characteristics for a trilayer MoS_2 back-gated FET

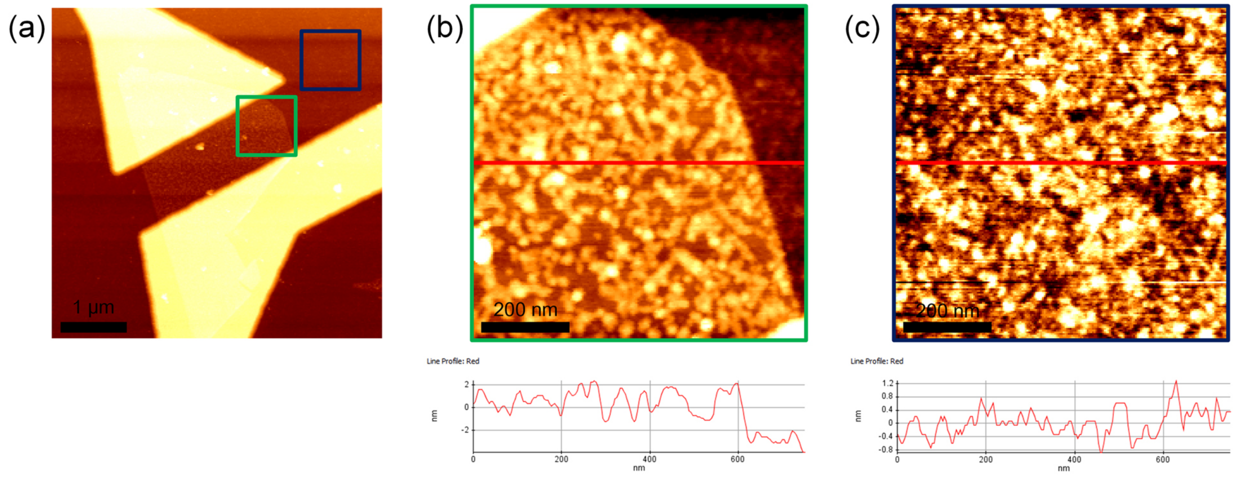

Figure 1.5: (a) AFM image of the superatom-doped WSe_2 FET. The green and blue lines indicate the areas imaged for the surface of WSe_2 and SiO_2, respectively. AFM images and height profiles of the surface of (b) trilayer WSe_2 and (c) SiO_2 after doping with 0.1 mg/mL of $Co_6Se_8(PEt_3)_6$.

before and after superatom doping. The as-prepared MoS_2 device exhibits n-type transistor characteristics with a large on/off current ratio ($\sim 10^5$) before doping. The carrier density of the pristine sample is estimated to be $2.0\times10^{12}\ cm^{-2}$ at $V_g = 0$ V from the measured threshold voltage (V_{th}). Compare to this pristine device characteristic, the transfer characteristic of the channel after immersion in superatom solution exhibits remarkable changes. First, the conductance of the device increased compared with that of the pristine one. Second, the transfer characteristic exhibits a weak n-type response to the gate voltage, without any apparent "off" current, indicating that the superatoms donate their electrons and heavily dope the MoS_2 film. The large number of carriers introduced by the superatoms at zero gate bias implies that charge transfer has occurred when the superatoms adsorb to the surface.

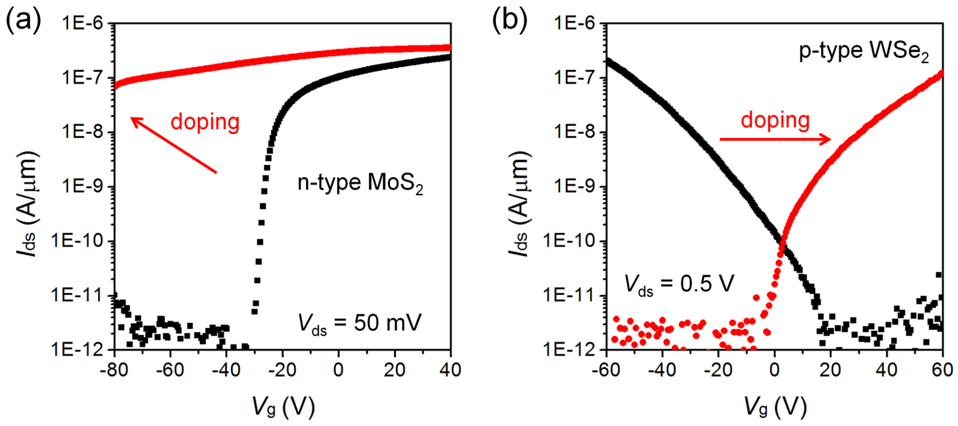

Figure 1.6: Transfer characteristics of the few-layer (a) MoS$_2$ and (b) WSe$_2$ FETs. The black and red curves are before and after doping with superatoms, respectively.

We used Raman spectroscopy to determine A_{1g} mode of MoS$_2$ shows any change upon the superatom doping and to further understand the charge transfer,[18] but we found that the laser interfered with the superatom adsorbates.

While the electron-rich superatom doping turns the pristine moderate n-type MoS$_2$ FET into the heavily n-doped channel, similar chemical treatment also affect p-type WSe$_2$ FETs. Figure 1.6b displays how superatom adsorption affects the p-type WSe2 layers. As shown by the black curve in this plot, the majority of WSe$_2$ FET devices with Pd source-drain contacts show typical p-type semiconductor characteristics before molecular cluster doping.[30] Once the pristine device is immersed in the $Co_6Se_8(PEt_3)_6$ solution, however, the transfer characteristics of WSe$_2$, exhibits strong electron transporting (n-type) behavior (red curve in Figure 1.6b). This change is consistent with injection of electrons into the WSe$_2$ layer from the molecular cluster. The shift in transfer characteristics at zero gate voltage implies that at equilibrium, the electron is transferred to the WSe$_2$ layer. We note that even after superatom doping, the current still depends strongly on the gate voltage with an excellent on/off characteristic ($\sim 10^5$). This is a strong contrast compared to previous chemical doping studies where doped WSe_2 devices exhibited degenerate doping with a suppressed on/off ratio.[17, 19] The difference between superatoms and these stronger dopants is in their redox potentials; the first redox potential of the $Co_6Se_8(PEt_3)_6$ superatom (-0.4 eV, relative to the standard hydrogen electrode (SHE))[5] lies between the conduction band edge (-0.7 eV vs. SHE) and the valence band edge (0.5 eV vs. SHE) of WSe_2.[31] We therefore anticipate that superatoms donate electrons to WSe_2 to compensate hole carriers introduced by applied gate field in the WSe_2 FETs.

1.3 Doping of WSe_2 in a controlled manner

The device characteristics and the degree of doping are directly linked to both the time that WSe_2 is exposed to the superatoms solution and the concentration of the superatom solution used for doping. When using a concentrated doping solution (1 mg/mL), the hole conductance of the WSe_2 decreases immediately, while the electron conductance increases over time and reaches a maximum value within 10 min of immersion time (Figure 1.7). A control experiment was conducted to check the organic solvent would affect the device characteristics. It should be noted that the threshold voltage (V_{th}) did not show the noticeable change when the device was immersed in toluene up to 10 min, although the hole current is slightly decreased.

When using a lower doping solution concentration (0.1 mg/mL), the transfer characteristics of a bilayer of WSe_2 maintains an ambipolar transport behavior, even for exposure times

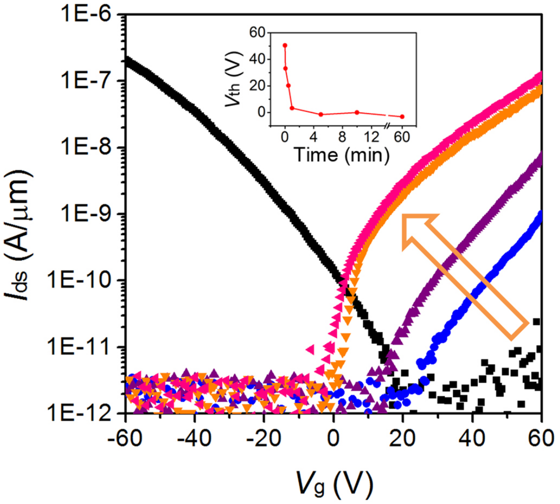

Figure 1.7: Transfer characteristics of a few-layer WSe$_2$ FET at V_{ds} = 0.5 V as a function of doping time. The black curve is before doping and the other curves are after 5 sec, 30 sec, 1 min, and 10 min doping with 1 mg/mL of $Co_6Se_8(PEt_3)_6$. Inset image is the plot of threshold voltage (V_{th}) changes as a function of molecular doping time.

that saturate the doping level (Figure 1.8a). Similarly, the electron conductance increases as the concentration of superatom solution increases. Figure 1.8b depicts the linear relationship between the concentration of cluster dopants in solution and the 2D sheet carrier density (n_{2D}) of WSe$_2$ after cluster doping. This could be explained by an equilibrium between clusters on the TMDC surface and clusters in solution. The 2D electron sheet density of n-doped WSe$_2$ devices can be estimated by $n_{2D} = (qR_s\mu_{FE})^{-1}$, where q is the electron charge, R_s is the sheet resistance at gate voltage +60 V, and μ_{FE} is the field-effect mobility. The electron mobility was extracted from $\mu_{FE} = (\frac{L}{WC_{ox}V_{ds}})(\frac{dI_{ds}}{dV_g})$, where L and W are the channel length and width and C_{ox} is the gate oxide capacitance per unit area. The extracted values of μ_{FE} and n_{2D} are 0.15 cm^2/Vs and 4.1×10^{12} cm^{-2}, respectively, for the

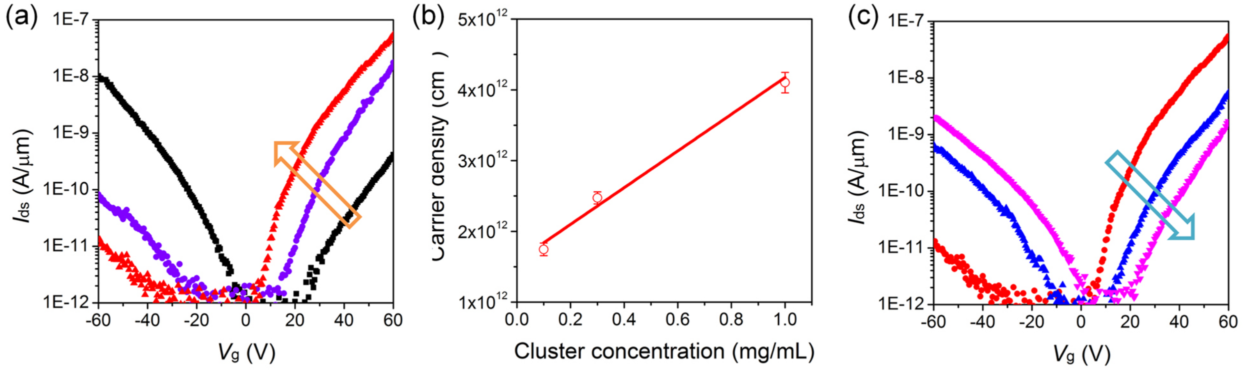

Figure 1.8: (a) Transfer characteristics of a bilayer WSe_2 FET doped with 0.1 mg/mL (purple) and 1 mg/mL (red) concentrations of the cluster. (b) The plot of the two-dimensional (2D) sheet carrier density (n_{2D}) of WSe_2 after doping as a function of the concentration of superatoms in solution. A bilayer WSe_2 device was immersed into 0.1 mg/mL, 0.3 mg/mL, and 1 mg/mL solutions, subsequently, for 10 minutes at each step. (c) Transfer characteristics of the doped device from Figure 1.8a after removal of clusters in toluene for 1 h (blue) and 24 h (pink).

doped WSe_2 with a concentrated (1 mg/mL) doping solution. Interestingly, the extracted mobilities for doped devices (in Figure 1.8a and 1.8b) showed similar values $\sim 0.1\ cm^2/Vs$, independent of the doping concentration.

Moreover, when immersing the doped device (from Figure 1.8a) in toluene solvent, the attached clusters dissociate from the surface, resulting in de-doping of WSe_2 (Figure 1.8c). For pristine WSe_2 device (black curve in Figure 1.8a), the extracted V_{th} for holes and electrons are -12 V (± 1 V) and 35 (± 4 V), respectively. After the doped device was immersed in toluene for 24 h (pink curve in Figure 1.8c), the extracted V_{th} for holes and electrons are -9

V (± 2 V) and 29 (± 4 V), respectively. These values are in good agreement with the initial V_{th} values.

These results demonstrate that we can controllably dope the WSe$_2$ films using electron-rich superatoms.

1.4 Lateral WSe$_2$ p-n junction formed by chemical doping

By combining this doping process with a lithographic mask, we can dope selected areas of a film of WSe$_2$. Using this local doping approach, we created a lateral p-n junction from a WSe$_2$ film. We first fabricated the mask from a few-layer hexagonal boron nitride (h-BN) flake.[32] We exfoliated h-BN flakes with a thickness of $10 - 30$ nm on a silicon wafer with thermally grown SiO$_2$ on its surface.[33] The deposited h-BN samples were patterned via e-beam lithography followed by inductively coupled plasma etching using a gas mixture of O$_2$ and CHF$_3$.[34] We then transferred the patterned h-BN mask onto the target WSe$_2$ flake (4 nm thick) using a polypropylene carbonate-coated polydimethylsiloxane (PPC-PDMS) stamp.[32, 34] By positioning the patterned h-BN, we introduced dopants through the opening over the channel in the device. To complete the device we created the source and drain electrodes through the h-BN windows (Figures 1.9).

Figure 1.10a shows a schematic and an optical image of the fabricated multi-terminal device, including the fully h-BN-protected, partially h-BN-protected and unprotected areas. This particular device made from a few-layer WSe$_2$ films exhibits the ambipolar transport characteristics. As shown in figure 1.10b, the unprotected device is very electron-doped, com-

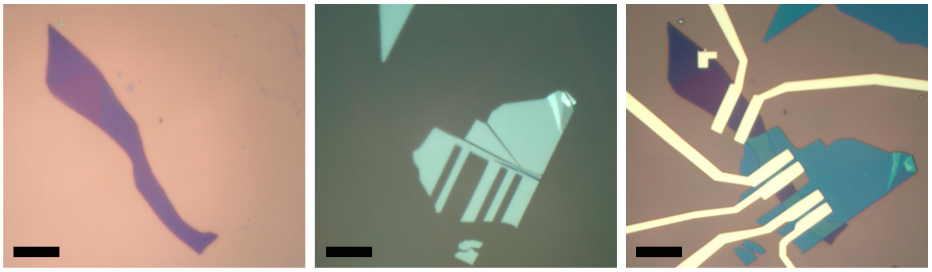

Figure 1.9: A series of optical images depict the fabrication process of the h-BN/WSe_2 heterostructure: i) Exfoliated WSe_2 on SiO_2/Si substrate, ii) Prepatterned h-BN picked up by PPC/PDMS substrate, iii) Transfer of the prepatterned h-BN on the target WSe_2 and formation of metal contacts. The scale bars are 10 μm.

pared to the fully h-BN-protected one, indicating doping by superatoms. It should be noted that the doping effect is less than the result shown in Figure 1.6b at the same concentration of cluster solution (1 mg/mL) because we use 4-nm thick WSe_2 for this experiment.

Using the selected-area doping method employing patterned h-BN encapsulation, we can create a lateral p-n junction device (indicated by dashed lines in the optical image in Figure 2a). Figure 2c displays the current - voltage ($I_{ds} - V_{ds}$) characteristics of the junction at various gate voltages after doping. We observe a remarkable change of the $I_{ds} - V_{ds}$ curve from symmetric to diode-like behaviour at gate voltages ranging from 20 to 40 V (Figure 1.10d), yielding a rectification ratio of three orders of magnitude at $V_{ds} = 1.5$ V. This diode behaviour is similar to the previous result from heterojunction of monolayer WSe_2 and MoS_2.[35] We also note that our observed rectification is more efficacious than the lateral MoS_2 p-n junction formed by $AuCl_3$ doping for the dark current.[36] When the gate voltage is not in the range resulting in a p-n junction, the device forms a p-p junction ($V_g < 0$ V) or

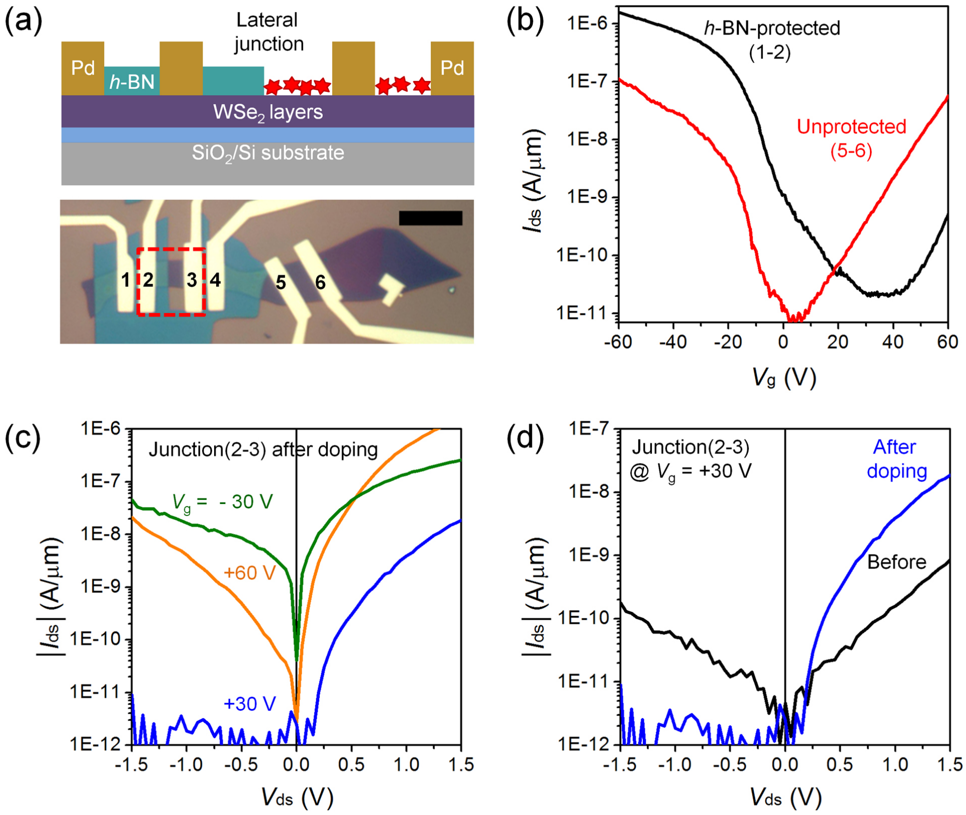

Figure 1.10: (a) Top: Schematic diagram of the h-BN/WSe_2 heterostructure devices subsequent to superatom doping. Bottom: Optical image of the multi-terminal devices fabricated on 4-nm thick WSe_2. The scale bar is 10 μm. (b) Transfer characteristics of the h-BN-protected (black) and the unprotected (red) WSe_2 FET at $V_{ds} = 0.5$ V after exposed to 1 mg/mL of $Co_6Se_8(PEt_3)_6$ solution. (c) Current – voltage ($I_{ds} - V_{ds}$) characteristics at various gate voltages measured across the junction (between electrodes 2 and 3) after doping. (d) $I_{ds} - V_{ds}$ curves of the lateral junction device at $V_g = +30$ V before (black) and after selective chemical doping (blue). (e) Expected band diagrams for p-p, n-n and p-n junctions at different gate voltages.

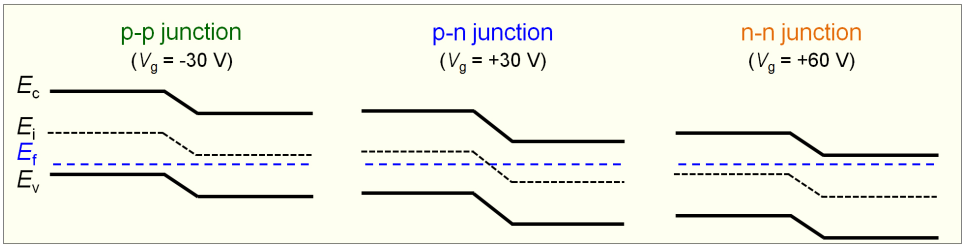

Figure 1.11: Expected band diagrams for p-p, n-n and p-n junctions at different gate voltages.

n-n junction ($V_g > 40$ V) (Figure 1.10e). In this case, the device exhibits rather symmetric $I_{ds} - V_{ds}$ curves (Figure 1.10c) as expected from the band alignment diagram in Figure 1.11.

In addition, we calculated the ideality factor from the Schockley diode equation: $I_{ds} = I_s \left(exp \left(\frac{V_{ds}}{nV_T} \right) \right)$, for $V_{ds} >$ 50-100 mV, where I_s is the reverse bias saturation current and V_T is the thermal voltage (25.85 mV at 300 K). The ideality factor, n, is extracted from the slope by plotting $ln(I_{ds})$ versus V_{ds} at forward bias. The ideality factor of the p-n junction is ~1.6, estimated from the $I_{ds} - V_{ds}$ curve at $V_g = 30$ V. This value deviates from that of an ideal diode presumably due to recombination occurring at the WSe_2/SiO_2 interface.

As a control experiment, we built a device in which the WSe_2 channel is fully covered by h-BN and measured its electrical properties before and after immersion in a solution of the dopant $Co_6Se_8(PEt_3)_6$. We find that h-BN is an efficient barrier to doping of the WSe_2: the device characteristics are essentially unaffected by the doping process (Figure 1.12a), confirming our hypothesis that h-BN prevents surface charge transfer to WSe_2. Moreover, $I_{ds} - V_{ds}$ curves for both devices are symmetric in both forward and reverse bias. Rectification ratios at all gate voltages are smaller than 15 at $V_{ds} = 1.5$ V (Figures 1.12b and 1.12d).

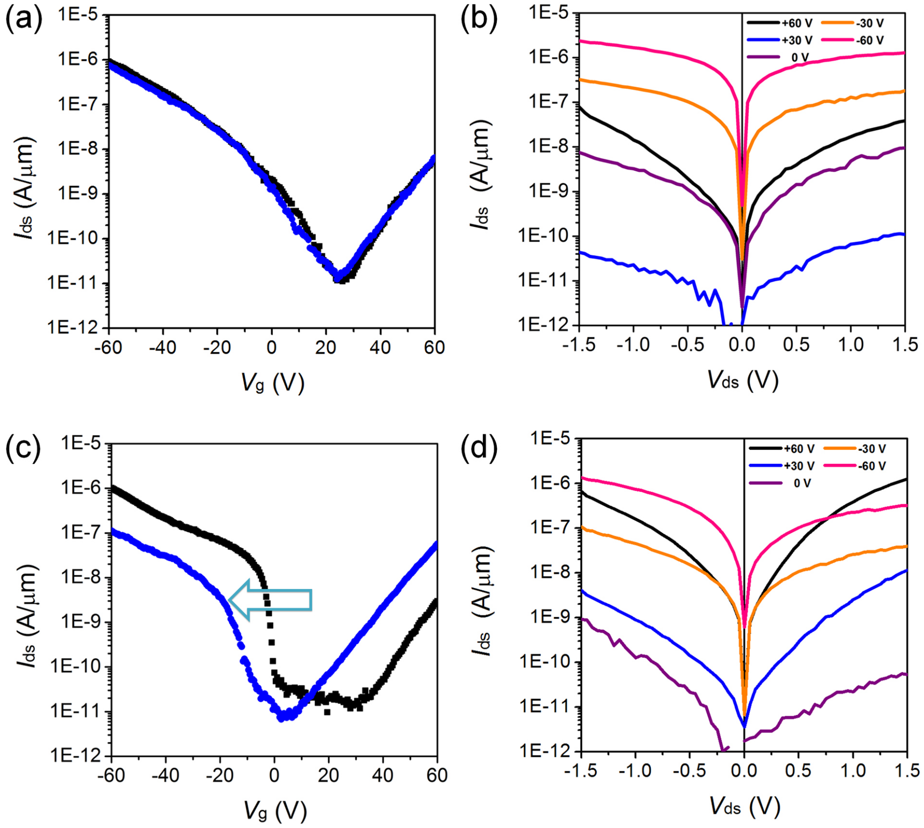

Figure 1.12: (a,c) Transfer characteristics of (a) the h-BN-covered (3-4) and (c) the unprotected (5-6) WSe$_2$ FET at V_{ds} = 500 mV before and after immersed into the $Co_6Se_8(PEt_3)_6$ solution. (b,d) Corresponding $I_{ds} - V_{ds}$ curves at various gate voltages from devices (a,c), respectively, after superatom doping.

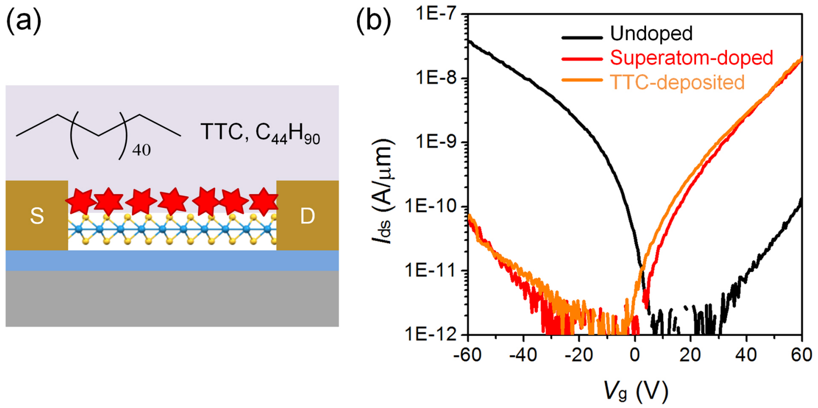

Figure 1.13: (a) Schematic of a superatom-doped WSe_2 FET with hydrocarbon passivation layer. (b) Transfer characteristics of trilayer WSe_2 FETs before (black) and after doping (red), and after TTC deposition (orange).

1.5 Lifetime enhancement of superatom-doped FETs protected with organic layer

We also tested the environmental stability of the doped WSe_2 FETs as the superatoms are somewhat sensitive to ambient conditions.[10] Figure 1.14a a displays the change in the device characteristics when we exposed the doped device to ambient conditions. We observe that the p-type transport characteristics of the WSe_2 are completely restored after ~11 hours. We speculate that the ability of the superatom to donate electrons as a dopant disappears as it is oxidized in air.

To improve the lifetime of our molecular cluster-doped WSe_2 FETs, we deposited a thin passivation layer of tetratetracontane (TTC, $C_{44}H_{90}$, Figure 1.13a).[37] We selected TTC because it can be thermally evaporated at low temperature (~50 °C), as a passivation layer. The relatively low temperature process we used prevents damages to our devices that would arise from higher temperature processing.[2] Figure 1.13b confirms that evaporation of the 150 nm thick layer of TTC does not affect the device characteristic of the doped WSe_2. The doped WSe_2 FET protected with a TTC layer maintains its original n-type semiconductor behavior after exposure to the ambient for 10 minutes, while the unpassivated device shows significant V_{th} shift (from 18 to 37 V) over the same time period (Figure 1.14a and 1.14b). For both devices, we extract the conductance value at gate voltage +60 V and plot it as a function of air exposure time in Figure 1.14c. Overall, we observe that TTC-passivated devices degrade much slower than unprotected ones.

1.6 Conclusion

We have demonstrated a new method to controllably dope MoS_2 and WSe_2 films. We find that the superatom $Co_6Se_8(PEt_3)_6$ is able to transfer electrons to the films. Upon doping, WSe_2 layers change their semiconductor characteristics from hole transporting to electron transporting. As a demonstration of the power of this technique, we fabricated a p-n junction by doping a portion of the channel in the WSe_2 device. We can use crystalline hydrocarbon layers to encapsulate the doped films and improve their ambient stability. This general method should be applicable to a variety of different TMDCs and superatoms with tailored electrochemical potentials.

---

[2] We deposited hydrocarbons instead of applying the h-BN layer on top of the superatom-doped device because h-BN cannot serve as a passivation material due to the top-contacted device architecture.

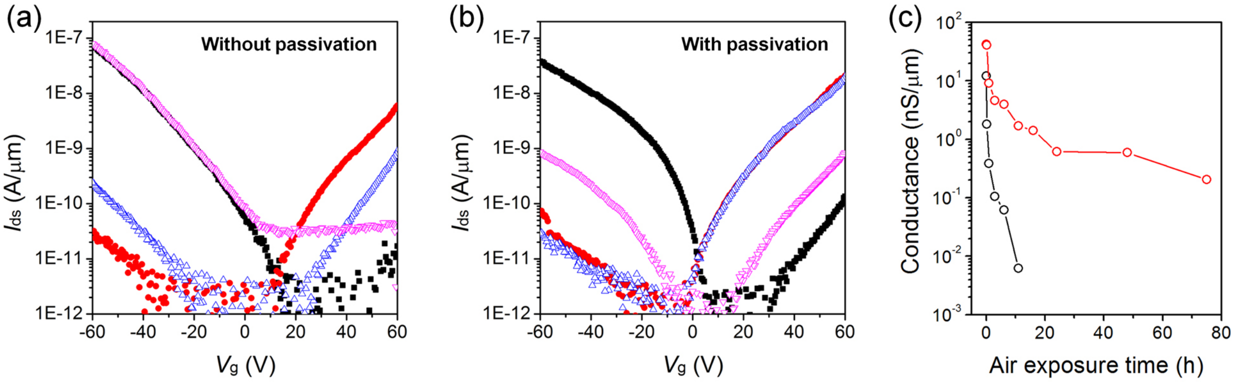

Figure 1.14: Transfer characteristics of trilayer WSe_2 FETs after exposure to an ambient condition (a) without and (b) with TTC-passivated layer. The black and red curves are before and after the superatom doping with 0.1 mg/mL of $Co_6Se_8(PEt_3)_6$, and the blue and pink curves are after 10 min and 11 h of exposure time. (c) The plot of conductance change at $V_g = +60$ V as function of exposure time to an ambient condition. The unpassivated device is shown in black and the passivated one is shown in red.

1.7 Experimental section

1.7.1 Fabrication of MoS_2 and WSe_2 devices

MoS_2 (SPI Supplies) and WSe_2 (Nanoscience Instruments) crystals were mechanically exfoliated on a Si substrate with a 285 nm SiO_2 capping layer. Atomic force microscopy (AFM, PSIA XE-100 and Bruker Dimension Fastscan AFM) was employed to measure the thickness of each flake. The thickness of MoS_2 and WSe_2 in all the tested devices was further confirmed by Raman spectroscopy and photoluminescence (PL) measurements (inVia, Renishaw). We

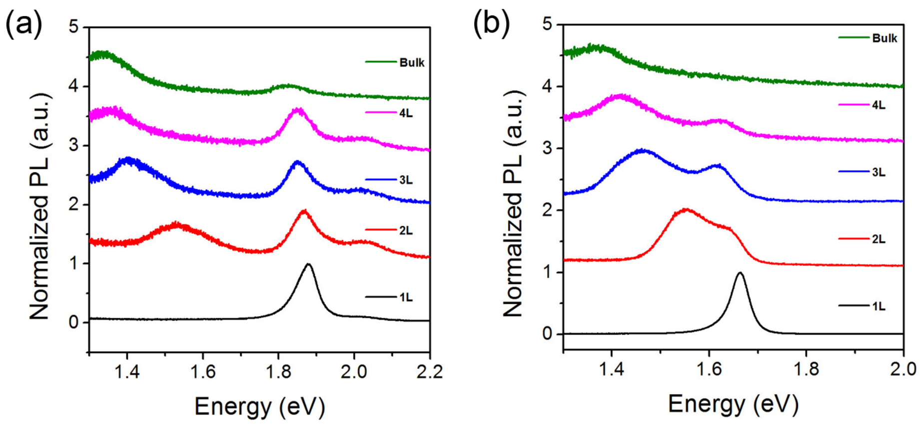

Figure 1.15: Normalized PL spectra of (a) MoS_2 and (b) WSe_2 thin layers under 532-nm laser excitation.

patterned source and drain electrodes on the TMDC films using e-beam lithography. The source/drain electrodes were patterned by e-beam lithography, followed by deposition of Al/Cr/Au (40/5/40 nm) for MoS_2 and Pd/Au (20/30 nm) for WSe_2. The conductance of the TMDC films was measured using an Agilent 4155C Semiconductor parameter analyzer and SUSS MicroTec EP4 probe station inside a glove box under nitrogen atmosphere.

1.7.2 Fabrication of the h-BN/WSe_2 heterostructure devices

For the h-BN/WSe_2 heterostructure devices (Figure 1.9), we started by exfoliating h-BN layers with thickness $10-30$ nm on a SiO_2/Si substrate. The patterned Poly(methyl methacrylate) (PMMA) was used as an etching mask for a dry etching process using inductively coupled plasma (ICP, Oxford 80) with a mixture of CHF_3 and O_2 gases. The typical etch rate was ∼30 nm/min. PMMA mask was removed in acetone. Then, a polypropylene carbonate (PPC) film of approximately 1 μm thickness was directly coated on a transparent poly-

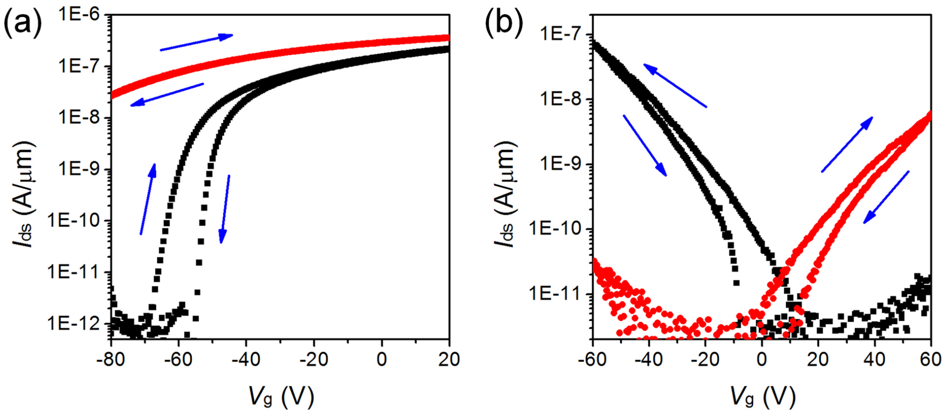

Figure 1.16: Hysteresis in transfer characteristic of (a) bilayer MoS_2 and (b) trilayer WSe_2 FETs. The black and red curves are before and after doping with $Co_6Se_8(PEt_3)_6$.

dimethylsiloxane (PDMS) stamp. The pre-patterned h-BN was picked up by PPC-PDMS stamp at 40 °C and transferred onto the target WSe_2 flake at 80 °C. After the dissolution of the PPC film in acetone, the second e-beam lithography process was followed to define the metal leads. Finally, the metals of Pd 50 nm/Au 50 nm were deposited.

1.7.3 Chemical doping experiments

The superatom dopant $Co_6Se_8(PEt_3)_6$ was synthesized according to a published procedure.[9] The $Co_6Se_8(PEt_3)_6$ superatom was dissolved in toluene with various concentrations ($0.01-1$ mg/mL). The fabricated device was immersed into the cluster solution for 10 min, followed by rinsing with fresh toluene to remove residual clusters non-selectively bound to the SiO_2 surface. Figure 1.5c showed only the surface roughness of SiO_2, indicating that the cluster was removed by rinsing with toluene. The preparation of cluster solution and the doping experiments were performed inside a glove box. AFM images (Figure 1.5) were acquired at room temperature under ambient conditions.

1.7.4 Hydrocarbon passivation of devices

Tetratetracontane (TTC, >97.0 % purity) was purchased from TCI chemical Co. and used as received. For the passivated device, a 150 nm thick TTC layer was deposited on the superatom-doped WSe_2 FET by thermal vacuum evaporation at a pressure of 1×10^{-6} *torr*. The evaporation rate of the TTC was 1 nm/sec.

Chapter 2

van der Waals Solids from Self-Assembled Nanoscale Building Blocks[1]

2.1 Introduction

The development of facile methods for isolation and manipulation of two-dimensional (2D) materials has fueled an explosion of interest in layered van der Waals structures. These solids exhibit strong in-plane bonding and comparatively weak interactions between the layers, allowing them to be exfoliated.[38–41] Fullerenes are attractive molecular building blocks for assembling functional materials,[42, 43] yet C_{60} crystallizes into a three dimensional solid held

---

[1] This chapter is based on work published in Nano Lett. **16**, 1445 (2016). Copyright 2016, American Chemical Society. My contribution to this study was focused on morphological characterization by AFM and mechanical exfoliation of van der Waals solids.

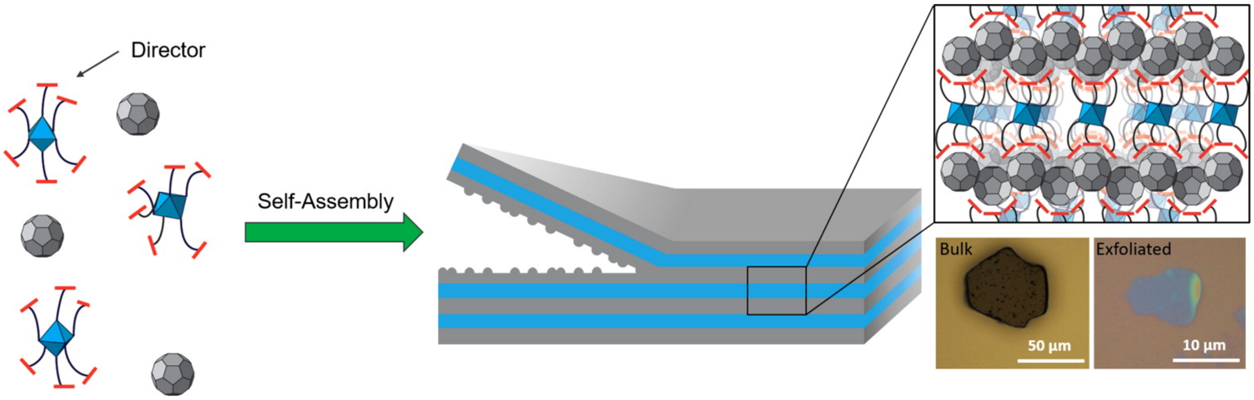

Figure 2.1: Schematic of a nanoscale director organizing a monolayer of fullerenes. Additional fullerenes that are not held in the ligand sphere have been omitted from the schematic. Optical microscope images show a crystal of the layered van der Waals material before and after exfoliation.

together by isotropic van der Waals interactions.[44] As a result, C_{60} cannot be exfoliated into discrete layers, unlike other nanostructured forms of carbon such as graphene[45] and carbon nanotubes.[46] Ionic solids of C_{60} with layered structures have been reported,[47, 48] but these solids also cannot be exfoliated because the components are held together by electrostatic interactions. While theory suggests that neutral C_{60} could form mechanically stable, free-standing monolayers,[49] these structures do not assemble spontaneously from solution and have only been prepared as epitaxial layers through carefully controlled vapor growth or on chemically modified surfaces.[50] As with many other 2D materials, unique emergent properties may arise in low-dimensional C_{60} arrays.[51–54]

In this chapter, we describe the self-assembly of fullerene monolayers into a layered van der Waals material. We employ a structurally adaptable transition metal chalcogenide cluster that associates with C_{60} and thereby directs the spontaneous assembly of C_{60} into neutral, corrugated monolayers. The director- and fullerene-layers form a two-dimensional van der Waals solid whose interlayer bonding is strong enough and whose intralayer bonding is weak enough that the material may be mechanically exfoliated (Figure 2.1).

2.2 Design of a nanoscale director

The reaction of the PEt_2phen (PEt_2phen = diethyl(9-ethynylphenanthrene)phosphine) ligand, elemental Se, and $Co_2(CO)_8$ in refluxing toluene provides the nanoscale director, $Co_6Se_8(PEt_2phen)_6$. Single crystal X-ray diffraction (SCXRD) confirms that the inorganic core of $Co_6Se_8(PEt_2phen)_6$ is isostructural with the parent cluster $Co_6Se_8(PEt_3)_6$.[10] The similarity between the two compounds is further supported by electronic absorption spectroscopy where the spectrum (Figure 2.2a) shows three longer-wavelength absorptions characteristic of the Co_6Se_8 core,[10] in addition to the absorptions due to the phenanthrene groups in the UV region. The electrochemical properties of $Co_6Se_8(PEt_2phen)_6$ (Figure 2.2b) also show three $[Co_6Se_8]$-centered reversible oxidations, but our director is less reducing than $Co_6Se_8(PEt_3)_6$ due to the diminished electron-donating ability of the PEt_2phen ligand compared to PEt_3.

We have previously reported that $Co_6Se_8(PEt_3)_6$ forms hierarchical solids with C_{60};[3] however, while $Co_6Se_8(PEt_3)_6$ is functionally spherical, $Co_6Se_8(PEt_2phen)_6$ can be anisotropic. The ligands on $Co_6Se_8(PEt_2phen)_6$ can reorganize to a thermodynamically stable unit with a shape that is complementary to C_{60}. When we combine $Co_6Se_8(PEt_2phen)_6$ and five equivalents of C_{60} in toluene, thin, flat, and hexagonal brown

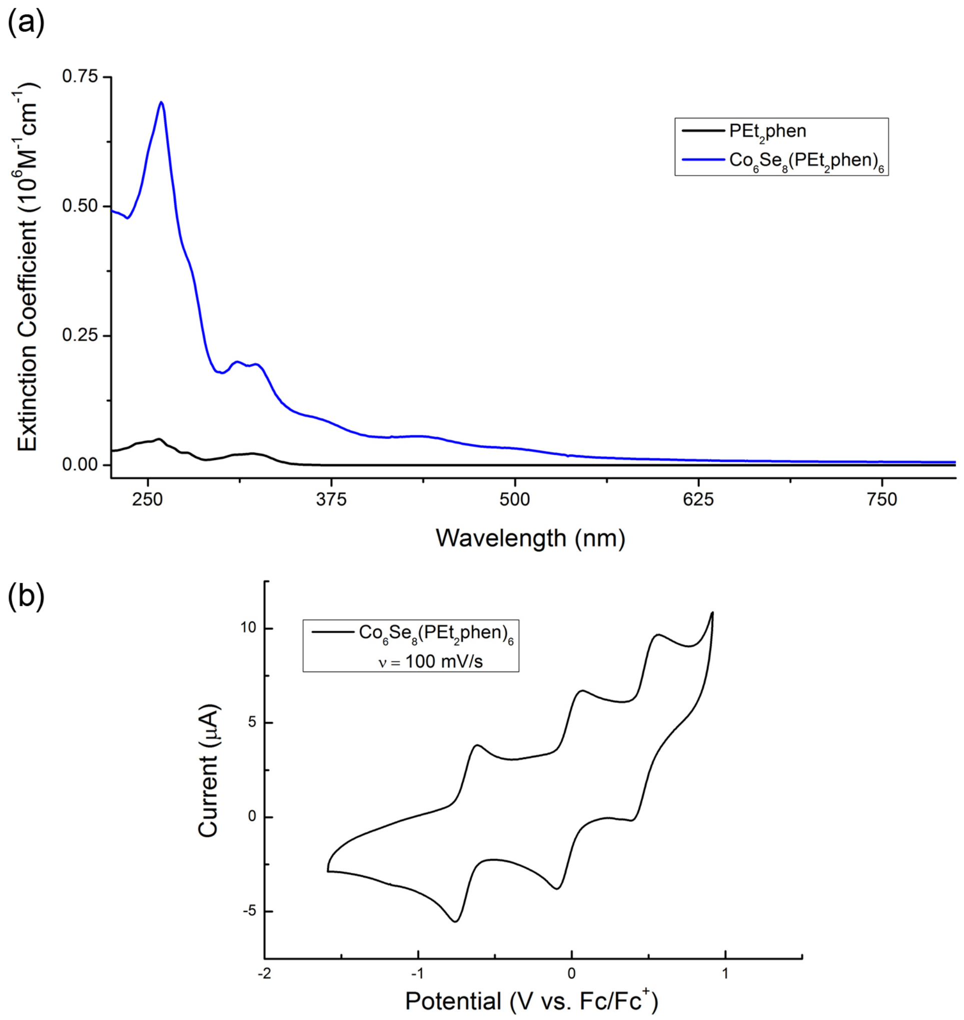

Figure 2.2: (a) Electronic absorption spectrum of PEt_2phen (13 μM) and $Co_6Se_8(PEt_2phen)_6$ (0.72 μM). (b) Cyclic voltammogram of $Co_6Se_8(PEt_2phen)_6$ in 0.1 M $TBAPF_6$ in tetrahydrofuran with a 100 mV/s scan rate.

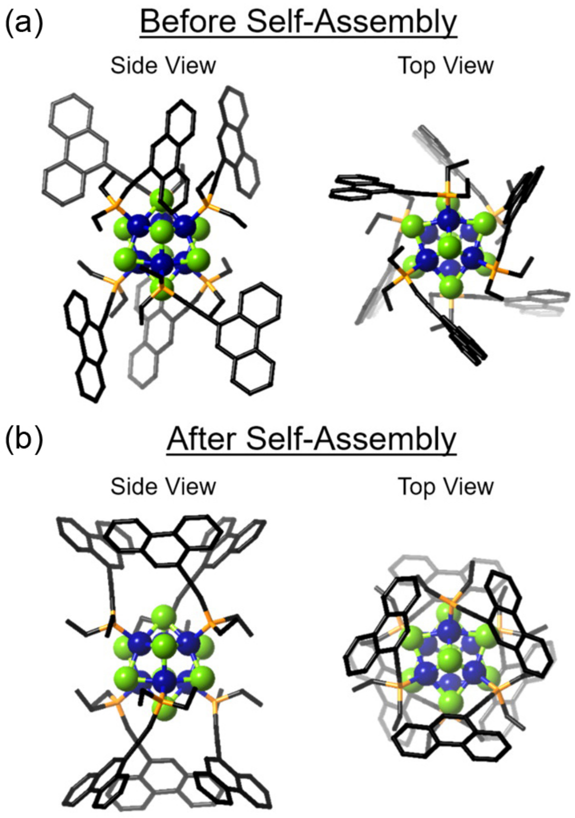

Figure 2.3: Molecular structure of the nanoscale director built from $Co_6Se_8(PEt_2phen)_6$ (a) before and (b) after self-assembly. The PEt_2phen ligands on each cluster reorganize to form two buckybowls that host C_{60}s in the solid-state.

crystals of $[Co_6Se_8(PEt_2phen)_6][C_{60}]_5$ form. Mechanical evaluation in tandem with crystallography shows that this material is not only structurally two-dimensional but also behaves physically like a layered solid.

Flexible molecular recognition elements in the ligand sphere create this self-assembled van der Waals material. Fullerenes are known to bind to molecular receptors such as corannulenes,[55] calix[n]arenes,[56, 57] cyclic paraphenyleneacetylenes,[58] and contorted hexabenzocoronenes[59, 60] that have concave surfaces. We reasoned that the octahedral geometry of the Co_6Se_8 cluster provides a simple yet versatile platform upon which we could build a flexible unit that can recognize C_{60}. While the phenanthrene ring on each phosphine is flat and provides only weak van der Waals interactions with C_{60}, three ethynylphenanthrene groups - one from each of three adjacent phosphines - can rotate in concert to form a "buckybowl" (Figure 2.3). The disposition of the ligands is different in isolated $Co_6Se_8(PEt_2phen)_6$(Figure 2.3a) than in the co-crystal of $[Co_6Se_8(PEt_2phen)_6][C_{60}]_5$ (Figure 2.3b). In the presence of C_{60}, the phenanthrenes decorating the Co_6Se_8 core extend and organize themselves to form two antipodal buckybowls, each capable of interacting with a guest C_{60}. This supramolecular "dumbbell" is the template that forms a basic unit in the extended structure. An unanticipated consequence of the buckybowl formation is the exposure of the equator of the Co_6Se_8 core, leaving a void that is filled by additional fullerenes (Figure 2.4a).

2.3 Self-assembly of the layered van der Waals solid

Figure 2.4a shows the extended molecular structure of the dumbbell with the other three equivalents of C_{60} in $[Co_6Se_8(PEt_2phen)_6][C_{60}]_5$. The structure is composed of two layers (identified as Layers CF and FL) stacked along the hexagonal *c*-axis. Layer CF is trigonal with stoichiometry $[Co_6Se_8(PEt_2phen)_6][C_{60}]_2$ in which the molecular cluster is surrounded by a flattened octahedron of fullerenes that are 3.3 Å above and below the mean plane of the layer (Figure 2.4b). Layer FL is a slightly corrugated trigonal array of fullerenes (Figure 2.4c). For each cluster, there are five C_{60}s that occupy three crystallographically distinguishable positions: two symmetry-related C_{60}s (grey) are sitting in the buckybowls, and these

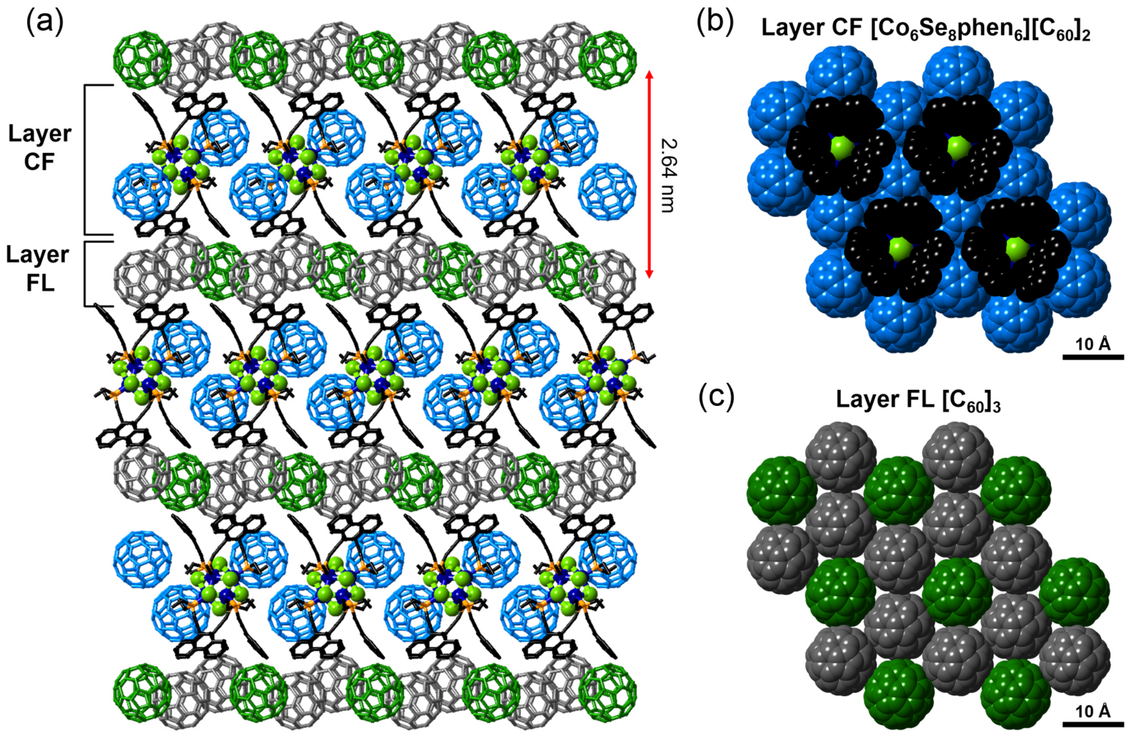

Figure 2.4: (a) Edge-on view of the molecular structure of [$Co_6Se_8(PEt_2phen)_6$][C_{60}]$_5$ looking down the ab plane. Layer CF consists of [$Co_6Se_8(PEt_2phen)_6$][C_{60}]$_2$, and Layer FL is a corrugated monolayer of C_{60}. Cobalt, blue; selenium, light green; phosphorus, orange; carbon, black. The fullerenes in Layer CF are shown in light blue; fullerenes that are sitting in the buckybowls within Layer FL are grey; fullerenes that are not associated with the buckybowls within FL are green. Hydrogen atoms and toluene molecules of solvation were removed to clarify the view. (b) Space-filled view of a single Layer CF looking down the c-axis. (c) Space-filled view of a single Layer FL looking down the c-axis.

are a part of the Layer FL. Two symmetry-related C_{60}s (light blue) are located in Layer CF, close to inorganic clusters; the fifth C_{60} (green), positioned within Layer FL, is not sitting in a buckybowl but is in contact with two interstitial coplanar toluene solvent molecules. Within Layer FL, the C_{60}s are in close contact having centroid-to-centroid distance ranging from 9.65 to 9.94 Å.

Similar to more traditional 2D van der Waals materials, $[Co_6Se_8(PEt_2phen)_6][C_{60}]_5$ crystals can be exfoliated. Figure 2.5b shows the atomic force microscope (AFM) image of a $[Co_6Se_8(PEt_2phen)_6][C_{60}]_5$ single crystal grown from solution. We observe a step-and-terrace structure on the surface of the $[Co_6Se_8(PEt_2phen)_6][C_{60}]_5$ crystals with ∼3 nm steps. We mechanically exfoliated single crystals of $[Co_6Se_8(PEt_2phen)_6][C_{60}]_5$, thereby isolating multilayer samples that we transfer onto Si wafers (Figure 2.5c). Under an optical microscope, exfoliated crystals display various colors (Figure 2.6) that we interpret as interference fringes, suggesting that flakes of different thickness are produced using this technique. We are able to produce samples that are as thin as ∼130 nm and have smooth surfaces (average roughness R_q ∼0.6 nm). This surface roughness is comparable to self-assembled C_{60} monolayers on Au,[61] and C_{60} films deposited and annealed on graphite.[62] In some exfoliated samples, we also observe small, ∼3 nm-high islands on the surfaces (Figure 2.5f). The step height in the layers (Figure 2.5b and 2.5f) is consistent with the height of a superatomic monolayer (Layer CF + Layer FL) calculated from the crystal structure (1/3 of the c-axis length, 2.64 nm). Therefore, when we exfoliate the flakes, they unzip along the 2D sheets of fullerenes.

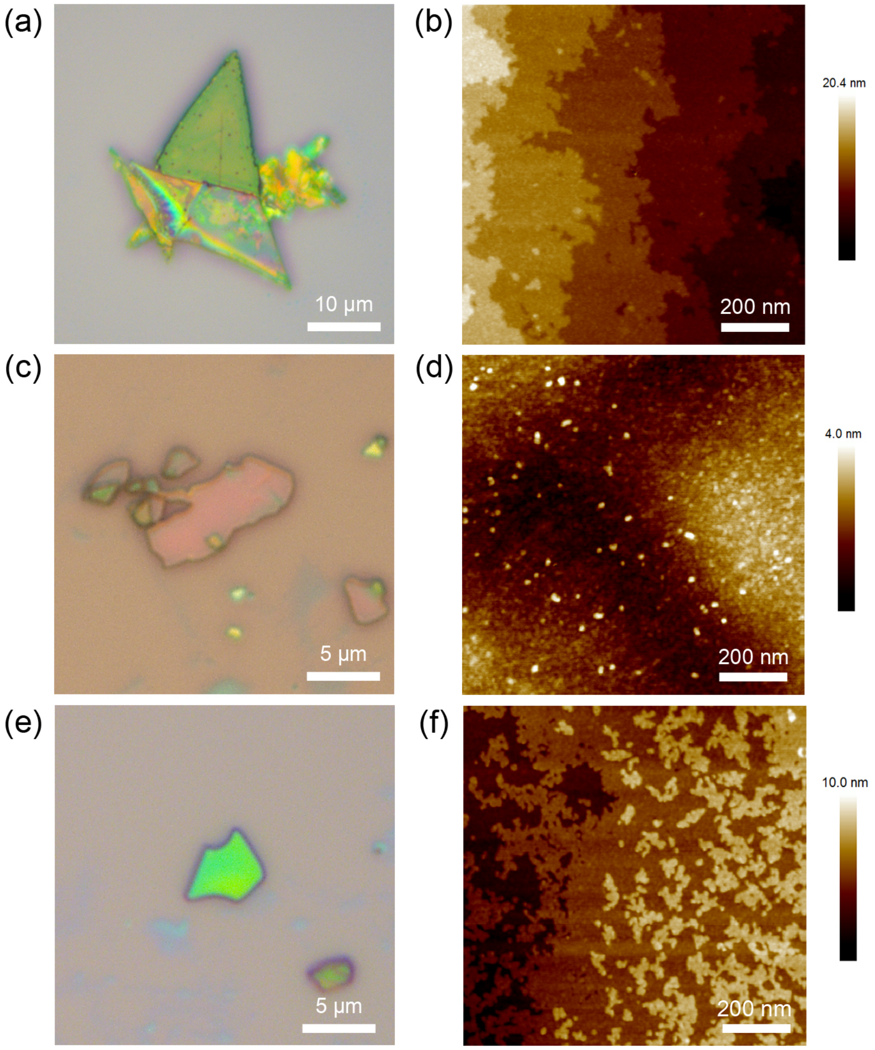

Figure 2.5: Optical microscope images of (a) as-grown single crystal and (c,e) mechanically exfoliated crystals of $[Co_6Se_8(PEt_2phen)_6][C_{60}]_5$, and respective AFM topographic images (b, d, and f). The thickness of the exfoliated crystals are 139 nm and 190 nm as determined by AFM.

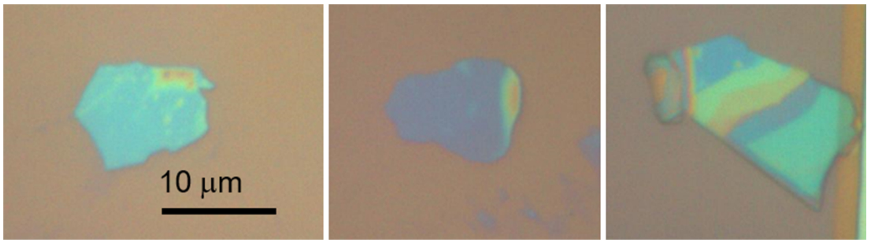

Figure 2.6: Optical images of mechanically exfoliated crystals of $[Co_6Se_8(PEt_2phen)_6][C_{60}]_5$.

2.4 Physical properties of the layered material

Micro-Raman spectroscopy of the layered van der Waals material indicates that no charge is transferred between the constituent clusters in $[Co_6Se_8(PEt_2phen)_6][C_{60}]_5$ (Figure 2.11 in Section 2.8) and that the structure is held together entirely by van der Waals interactions. SQUID magnetometry reveals that the material is diamagnetic and supports the observation that there is no measurable charge transfer. We have collected structural data on a large library of $Co_6Se_8(PR_3)_6$ clusters in known oxidation states (0, +1, and +2; Figure 2.8 in Section 2.7), and we can assess the oxidation state of the cluster by comparing its Co-P and Co-Co$_{trans}$ distances to this database. This analysis also indicates that the cluster bears no charge in the layered solid.

We performed two-probe electrical resistivity measurements on single crystals of $[Co_6Se_8(PEt_2phen)_6][C_{60}]_5$. As shown in Figure 2.7a, the layered solid exhibits in-plane activated electrical transport behavior, and we observe an exponential decrease of the conductance (G) with decreasing temperature. This thermally activated transport displays an Arrhenius behavior with an activation energy E_a of ~400 meV. This energy barrier is higher than the transport barrier of the parent, ionic solid $[Co_6Se_8(PEt_3)_6][C_{60}]_2$ (E_a ~150 meV).[3]

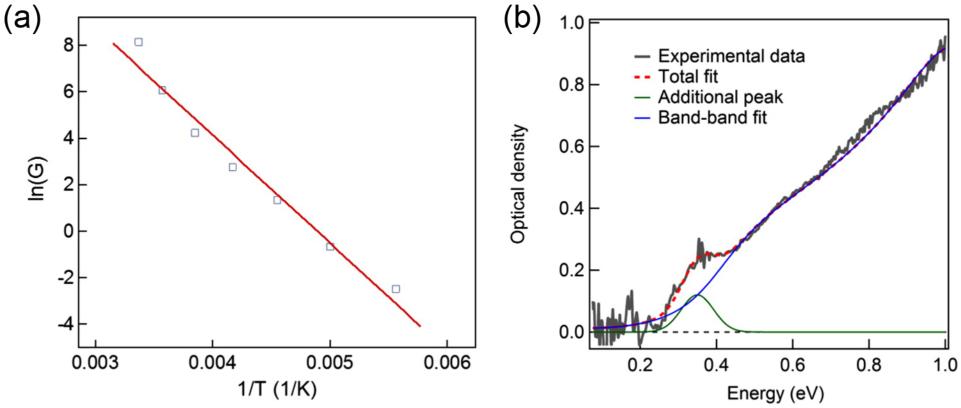

Figure 2.7: (a) Log plot of conductance (G) vs. 1/T for $[Co_6Se_8(PEt_2phen)_6][C_{60}]_5$. The two-probe conductance measurements were done on a single crystal. Using the Arrhenius fit, solid red line, we obtained an activation energy of 400 meV. (b) Mid-IR absorption spectrum of $[Co_6Se_8(PEt_2phen)_6][C_{60}]_5$. The red dashed curve was obtained from a fit using band-to-band transition for semiconductors (blue) with an additional Gaussian peak (green) near the band-edge. The obtained bandgap is 390 ± 40 meV.

Figure 2.7b shows the optical absorption spectrum for $[Co_6Se_8(PEt_2phen)_6][C_{60}]_5$ using Fourier Transform Infrared (FT-IR) spectroscopy. The measurement was performed in microscopic transmission mode on a single flake of the crystal at room temperature. The spectrum is characteristic of that of a direct bandgap semiconductor.[63] The enhanced absorbance near the threshold is similar to that of an excitonic resonance.[64] While we do not know the exact origin of this resonant feature near the threshold/bandgap, we use a Gaussian in addition to the bulk part of the Elliot's theory which describes band-to-band optical transition for direct bandgap semiconductors to fit the experimental data (see Section 2.9) Supporting Information).[64] The fit yields a bulk bandgap of 390 ± 40 meV, in excellent agreement with the activation energy obtained from electrical transport measurement. The origin of the resonant enhancement near the bandgap (peak at ∼350 meV, the green curve in Figure 2.7b) is not known and remains a subject for future mechanistic study.

2.5 Conclusion

In conclusion, we describe here a 2D van der Waals solid self-assembled from a nanoscale building block and C_{60}. The resulting crystalline solid features a corrugated monolayer of fullerenes that are separated by a layer comprising a combination of the structure-directing inorganic cluster and C_{60}. The crystal can be mechanically exfoliated into thinner sheets with smooth surfaces. Because we see a consistent step size of ∼3 nm, we believe that the exfoliation results in "unzipping" of the fullerene monolayer. The absorption spectrum of the bulk crystal shows what is consistent with an excitonic feature at room temperature and bulk optical gap of 390 ± 40 meV that matches well with the thermal activation energy obtained from transport measurement. These properties are decidedly different from those of the bulk fullerene and thus make this system exciting for future study of dimensionally confined neutral C_{60}s. Furthermore, we aim to generalize the use of structure-directing molecular clusters to reorganize canonical materials in new and exciting ways.

2.6 Synthesis and characterization information

2.6.1 Synthetic details

General Information

Chlorodiethylphosphine was purchased from Acros Organics. Dicobalt octacarbonyl and selenium powder were purchased from Strem Chemicals. C_{60} buckminsterfullerene was purchased from Bucky USA. All other reagents and solvents were purchased from Sigma Aldrich. Dry and deoxygenated solvents were prepared by elution through a dual-column solvent system (MBraun SPS). All reactions and sample preparations were carried out under inert atmosphere using standard Schlenk techniques or in a nitrogen-filled glovebox. 9-Ethynylphenanthrene was prepared according to published protocol.[65]

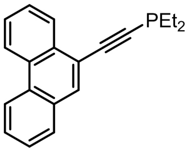

Diethyl(9-ethynlphenanthrene)phosphine ("PEt$_2$phen")

A solution of 9-ethynylphenanthrene[65] (1.0 g, 4.9 mmol) in THF (50 mL) was cooled to -78 °C and *n*-butyllithium (3.7 mL, 5.9 mmol, 1.6 M in hexanes) was added dropwise. The reaction mixture was stirred for 1 h at -78 °C. A solution of chlorodiethylphosphine (920 mg, 7.4 mmol) in THF (10 mL) was added dropwise to the solution and the reaction was warmed gradually to room temperature. After stirring for ~12 h, the solvent was removed *in vacuo* and 20 mL of toluene was added to the crude product. The mixture was filtered through a medium frit over celite. The filtrate was evaporated to dryness *in vacuo* to afford a yellow oil. Yield: 1.1 g (80 %)

^{1}**H NMR** (400 MHz, [d_8-toluene], 298 K): δ = 1.18-1.26 (6H, m), 1.50-1.74 (4H, m), 7.26-7.46 (5H, m), 7.85 (1H, s), 8.27-8.35 (2H, m), 8.63-8.65 (1H, m)

^{31}**P NMR** (162 MHz, [d_8-toluene], 298 K): -39

$Co_6Se_8(PEt_2phen)_6$

To a solution of PEt_2phen (1.07 g, 3.68 mmol) in toluene (50 mL) was added selenium powder (290 mg, 3.68 mmol) and the suspension was stirred for 1 h at room temperature. Dicobalt octacarbonyl (315 mg, 0.92 mmol) dissolved in toluene (15 mL) was added and the mixture was heated to reflux for ~16 h. The hot mixture was filtered through a fine frit. The dark brown solution was cooled to room temperature and concentrated to 10 mL *in vacuo*. 80 mL of diethyl ether was added to precipitate the product. The crude product was isolated by filtration through a fine frit and dissolved in 20 mL of toluene. Hexanes diffusion at room temperature yielded dark brown crystals. The supernatant solution was decanted and the recovered dark brown crystals were washed with hexanes (2 x 20 mL) and dried *in vacuo*. Yield: 745 mg (89 %) based on amount of dicobalt octacarbonyl used.

^{1}**H NMR** (400 MHz, [d_8-toluene], 298 K): δ = 1.23-1.31 (6H, m), 2.21-2.38 (4H, m), 7.12-7.16 (1H, m), 7.23-7.27 (2H, m), 7.31-7.34 (1H, m), 7.46-7.50 (1H, m), 7.89 (1H, s), 8.16-8.21 (2H, t), 9.02 (1H, d)

^{31}**P NMR** (162 MHz, [d_8-toluene], 298 K): 38 (broad)

$[Co_6Se_8(PEt_2phen)_6][C_{60}]_5$

The cluster $Co_6Se_8(PEt_2phen)_6$ (42 mg, 15 μmol) and C_{60} (55 mg, 77 μmol) were dissolved in 30 mL of toluene. The solution filtered through a 0.2 μm syringe filter. Dark brown crystals were obtained after 8 weeks upon slow evaporation of toluene. The solid was collected, rinsed with hexanes and ether, and dried *in vacuo.* Yield: 20 mg (20 %)
Alternatively, dark brown crystals were obtained after 2 weeks upon diffusion of hexanes vapor into a co-solution of $Co_6Se_8(PEt_2phen)_6$ (18 mg, 6 μmol) and C_{60} (21 mg, 29 μmol) in 8 mL of toluene. The solid was collected, rinsed with hexanes and ether, and dried in vacuuo. Yield: 29 mg (77 %)

2.6.2 Instrument details

NMR

All ^{1}H and ^{31}P NMR were recorded on a Bruker DRX400 spectrometer.

Electronic absorption

Solution-phase electronic absorption spectra were taken on a Shimadzu UV-1800 spectrophotometer. All samples were dissolved in THF and loaded in a 1-cm quartz cuvette sealed under nitrogen.

X-ray diffraction

Single crystal X-ray diffraction (SCXRD) data were collected on an Agilent SuperNova diffractometer using mirror-monochromated Cu K_α radiation. The crystals were mounted using a MiTeGen MicroMount cooled to 100 K with an Oxford-Diffraction Cryojet system. Data collection, integration, scaling (ABSPACK) and absorption correction (face-indexed

Gaussian integration[66] or numeric analytical methods[67]) were performed in CrysAlisPro (Agilent Technologies). Structure solution was performed using ShelXS,[68] ShelXT,[69] or SuperFlip.[70] Subsequent refinement was performed by full-matrix least-squares on F^2 in ShelXL.[68] Olex2[71] was used for viewing and preparing CIF files. PLATON[72] was used for SQUEEZE,[73] ADDSYM[74] and TwinRotMat. Many disordered solvent molecules were modeled as rigid fragments from the Idealized Molecular Geometry Library.[75] Details of crystallographic data and parameters for data collection and refinement are in Table 2.1 in Section 2.7.

Powder X-ray diffraction (PXRD) data were collected on a PANalytical X'Pert^3 Powder diffractometer. We used an Anton Paar air-free sample holder equipped with a polycarbonate dome to seal the sample under a nitrogen atmosphere. This dome has a broad amorphous peak from 18 to 25°, and this background was subtracted using HighScore Plus.

Cyclic voltammetry

Electrochemistry for $Co_6Se_8(PEt_2phen)_6$ was carried out in THF with tetra-*n*-butylammonium hexafluorophosphate ($TBAPF_6$) supporting electrolyte (0.1 M) using a CH Instruments Electrochemical Analyzer potentiostat inside a nitrogen-filled glovebox. Measurements were carried out with a glassy carbon working electrode, a platinum counter electrode, and a platinum pseudo-reference electrode. Measurements were calibrated using ferrocene/ferrocenium redox couple.

AFM

AFM images were acquired in ScanAsyst mode by a Bruker Dimension Icon system under ambient conditions.

2.7 X-ray crystallographic characterization

2.7.1 Single crystal X-ray diffraction

$Co_6Se_8(PEt_2phen)_6$

Crystals were grown by vapor diffusion of hexanes into a concentrated toluene solution, which afforded black blocks. Part of a crystal (.14 × .04 × .02 mm) was separated carefully, mounted with STP oil treatment, and cooled to 100 K on the diffractometer. Complete data (98.9 %) were collected to 0.815 Å. 36565 reflections were collected (11067 unique, 10365 observed) with R(int) 3.2 % and R(sigma) 3.1 % after Gaussian absorption correction (Tmax .821, Tmin .498).

The structure solved readily in P-1 using ShelXS with 1/2 cluster in the asymmetric unit. All non-H, non-solvent atoms were located in Fourier maps and refined anisotropically with no restraints. A toluene molecule was located on an inversion center and refined as a rigid fragment from the IMGL. C-H hydrogens were placed in calculated positions and refined with riding coordinates and ADPs.

The final refinement (11067 data, 0 restraints, 686 parameters) converged with R_1 ($F_o > 4\sigma(F_o)$) = 2.7 %, wR_2 = 7.0 %, S = 1.04. The largest Fourier features were 0.75 and -0.69 e^- $Å^{-3}$.

$[Co_6Se_8(PEt_2phen)_6][C_{60}]_5$

Crystals were prepared by slow evaporation of a toluene co-solution of the precursors. Many crystals were aggregates of individual flakes stuck together on their flat (001) faces. A single crystal (.08 × .05 × .01 mm) was selected, mounted with STP oil treatment and cooled to 100 K on the diffractometer. The diffraction pattern was weak but showed sharp Bragg peaks out to the resolution limit. Since the thin crystal was expected to need accurate absorption correction, a highly redundant data set was collected, approximately 2x the full sphere (21.8x redundancy in -3m1). Frames were collected at 12.5 s exposures for detector theta = 35 ° and 62.5 s for theta = 110 °, which resulted in a 4 day data collection. 101472 reflections were collected (4657 unique, 4030 observed) with R(int) 10.0 % and R(sigma) 3.1 % after absorption correction (Tmax .948, Tmin .748).

Merging R statistics and $<E^2-1>$ suggested the space group was R-3 or R-3m. Superflip proposed R-3m, which gave a well-resolved $Co_6Se_8P_6$ core, but the density for the phosphine alkyl groups and the C_{60} molecules was hard to interpret. A refinement in R-3 (merohedrally twinned) gave a more interpretable difference map, but the phosphine was disordered by clockwise/counterclockwise orientation around the c axis. Inspection of this disordered structure showed that it was actually a special position disorder in R-3m. The phosphine geometry was introduced to the R-3m solution as a FRAG fragment in part -1 with DFIX restraints on bonded C-C distances.

The C_{60} molecules were apparent in the difference map, but specific atomic positions were difficult to locate. Each fullerene was introduced as a rigid fragment from the Idealized Molecular Geometry Library with a negative part number and an occupancy determined from its Wyckoff position. Subsequent refinement and examination of difference maps showed that each fullerene was disordered over several independent positions; two were modeled in two independent positions and one was modeled in three independent positions. None of the fullerenes was in a position that fit its site symmetry. Due to the extensive disorder and the rigid nature of the C_{60} molecule, a group isotropic ADP was refined for each fullerene.

A disordered toluene molecule was located in the cluster layer and refined as a rigid fragment in 3 independent positions.

In the final refinement it was possible to release all DFIX restraints on the phosphine ligand. All ADPs were restrained by RIGU; the disordered toluene was additionally restrained by SIMU. All H atoms were placed in calculated positions and refined with riding coordinates and isotropic ADPs. The final refinement (4657 data, 407 parameters, 636 restraints) converged with R_1 ($F_o > 4\sigma(F_o)$) = 4.1 %, wR_2 = 9.7 %, S = 1.03. The largest Fourier features were 0.61 and -0.46 e^- $Å^{-3}$.

2.7.2 X-ray structural analysis of cluster oxidation state

We analyzed a set of 35 published and unpublished crystal structures of $Co_6Se_8(PR_3)_6$ clusters in unambiguous neutral, 1+ and 2+ oxidation states. A manuscript is in preparation, but the key findings are summarized in Figure 2.8. One-electron oxidation causes a lengthening of approximately 0.02-0.04 Å in the cluster's average Co-P bond length. This change is predicted in a DFT study of the related series $Co_6Te_8(PH_3)_6{}^{n+}$ (n = 0-2).[76] A second one-electron oxidation causes further Co-P lengthening and a substantial (0.1 Å) contraction of the average *trans*- Co-Co distance.

Several features are noteworthy: $Co_6Se_8(PAr_3)_6$ clusters are an exceptional case due to the high steric demand of the ligand. PAr_3-capped clusters are denoted by open points. Three reported structures of neutral clusters revealed a geometry agreeing closely with the

Table 2.1: Selected crystallographic data.

Compound	**$Co_6Se_8(PEt_2phen)_6 \cdot C_7H_8$**	**$[Co_6Se_8(PEt_2phen)_6][C_{60}]_5 \cdot 2C_7H_8$**
Formula	$C_{127}H_{122}P_6Co_6Se_8$	$C_{434}H_{130}Co_6P_6Se_8$
MW (g/mol)	2819.32	6415.45
Space group	P-1	R-3m
a (Å)	13.1106(2)	16.7992(2)
b (Å)	15.1825(3)	16.7992(2)
c (Å)	16.7649(3)	79.0867(11)
α (°)	107.4345(16)	90
β (°)	103.1693(15)	90
γ (°)	107.2058(17)	120
V (Å^3)	2852.06(10)	19329.0(6)
Z	1	3
ρ_{calc} (g$\cdot$ cm^{-3})	1.641	1.679
T (K)	100	100
λ (Å)	1.54184	1.54184
$2\theta_{min}$, $2\theta_{max}$	9.814, 143.7	8.258, 143.1
Nref	36565	101472
R(int), R(σ)	0.0316, 0.0312	0.0998, 0.0309
μ (mm^{-1})	10.77	5.196
Size (mm)	0.14 × 0.03 × 0.02	0.08 × 0.06 × 0.01
T_{max}, T_{min}	0.821, 0.498	0.968, 0.748
Data	11067	4657
Restraints	0	636
Parameters	686	407
R_1(obs)	0.0274	0.0412
wR_2(all)	0.0700	0.0967
S	1.037	1.028
Peak, hole (e$^-$ Å^{-3})	0.75, -0.69	0.62, -0.46

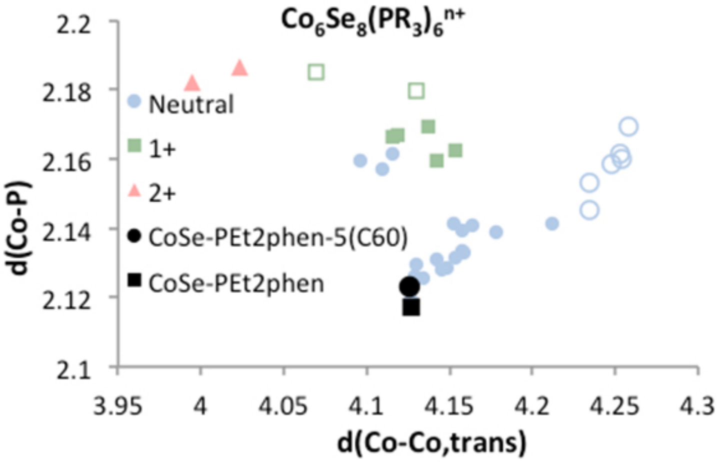

Figure 2.8: Geometries of $Co_6Se_8(PR_3)_6$ clusters in 0, 1+ and 2+ oxidation states. Open points represent PAr_3-capped clusters, which showed a significant effect of steric crowding. See discussion above for the 3 "neutral" data points grouped among the +1 structures.

majority of 1+ clusters. All three of these unusual examples had been treated with PLATON SQUEEZE to model disordered solvent. Therefore we surmise that these 3 structures were probably inadvertently characterized as salts with unknown anions.

$[Co_6Se_8(PEt_2phen)_6][C_{60}]_5$ contains a cluster with geometry almost identical to the isolated building block. Specifically, $Co_6Se_8(PEt_2phen)_6$in its co-crystal with C_{60} has its average Co-P distance lengthened by 0.009(4) Å and its average Co-Co_{trans} distance contracted by 0.0025(19) Å. This demonstrates that the fullerene co-crystal is assembled through van der Waals forces with no charge transfer from cluster to C_{60}.

2.7.3 Power X-ray diffraction

The collected diffraction patterns are in good agreement with the simulated powder patterns generated from the SCXRD data (Figures 2.9 and 2.10) and there are no indications of amorphous content, confirming the purity of the crystalline phase. Small crystals were evenly dispersed, uncrushed, on a zero-background Si plate and covered with a polycarbonate dome, as the crushing of the crystals led to the destruction of the crystalline lattice as indicated by significant broadening and degradation of the diffraction pattern upon sample grinding. We note that the material $[Co_6Se_8(PEt_2phen)_6][C_{60}]_5$ grows as thin plates that tend to pack with a preferred orientation on the substrate. We also note that the simulated patterns were generated from SCXRD run at 100 K, while the PXRD patterns were collected at room temperature, and that some of the solvates are removed from the crystal lattice under ambient conditions. Taken together, these details account for the differences between the experimental PXRD patterns and the simulated ones.

2.8 Raman spectroscopy

For Raman measurements of $[Co_6Se_8(PEt_2phen)_6][C_{60}]_5$, a 532 nm diode-pumped solid-state laser reflects off a 532 nm dichroic beam-splitter in a Nikon Ti/U inverted microscope. A 40x, 0.6 N.A. objective focuses the light to a 1 μm^2 spot size. Scattered light passes through a 75 micron pinhole into a Princeton Instruments 0.3 meter Acton Spectrometer with a 1200 g/mm grating and onto a Princeton Instruments PIXIS 400 CCD array detector. The instrument has a 5 cm^{-1} resolution, which is determined from the 546 nm H_g emission line.

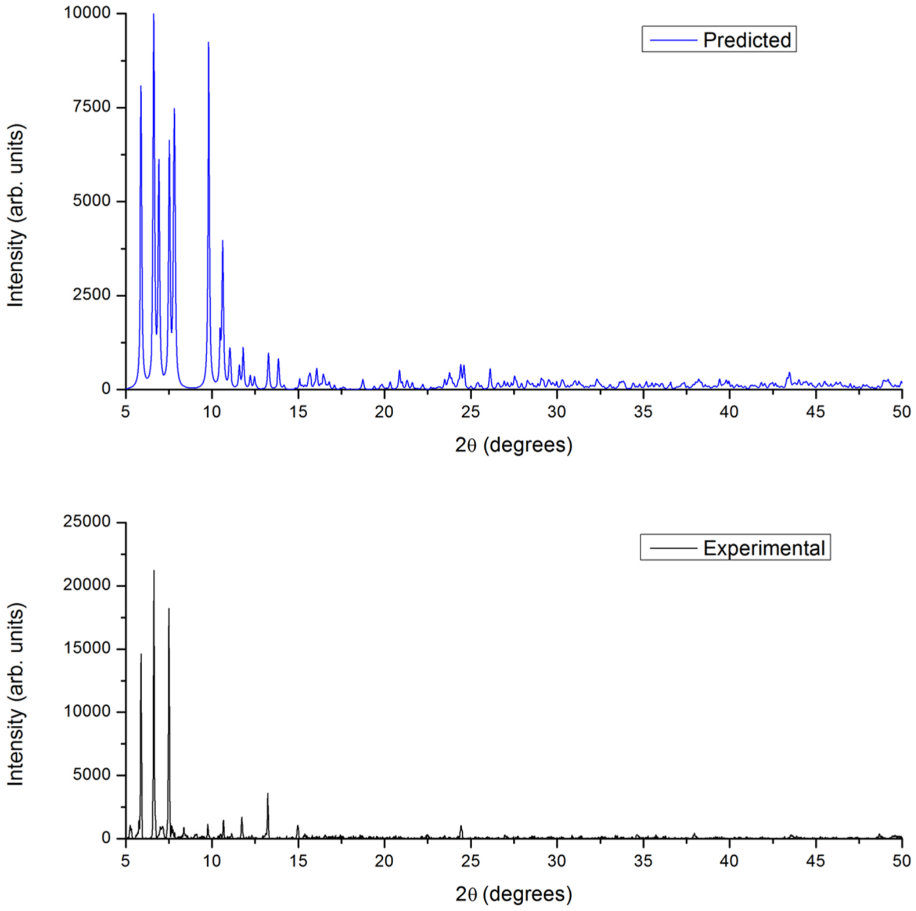

Figure 2.9: PXRD of $Co_6Se_8(PEt_2phen)_6$ simulated from SCXRD data (top) and experimental (bottom).

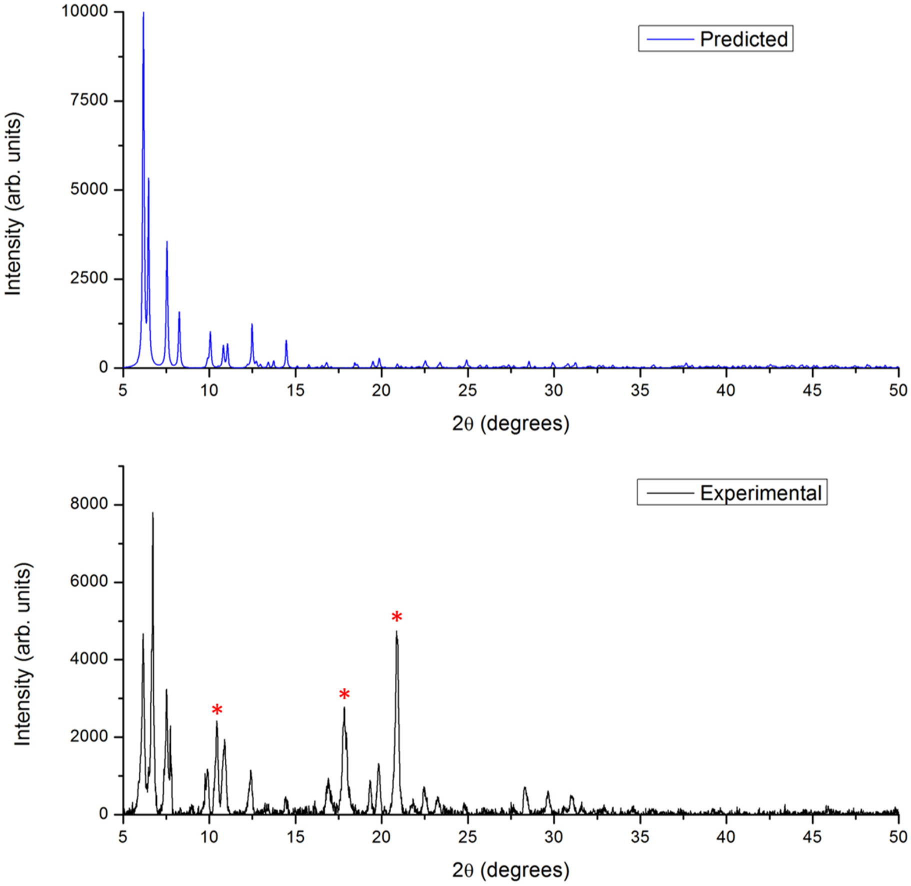

Figure 2.10: PXRD of $[Co_6Se_8(PEt_2phen)_6][C_{60}]_5$ simulated from SCXRD data (top) and experimental (bottom). The red asterisks denote the presence of a small fraction of C60 impurity.

Exposure times were 300 or 600 seconds.

The $A_g(2)$ pentagonal pinch mode, located at 1469 cm^{-1} in solid C_{60}, is a useful probe for characterizing metal chalcogenide cluster-C_{60} materials, because this vibration shifts to lower energy by 6 cm^{-1} per electron transferred to C_{60}.[77] However, photopolymerization can shift the $A_g(2)$ mode to 1463 cm^{-1} and 1459 cm^{-1}, and fullerene triplet state excitation can produce peaks at 1465 cm^{-1} and 1458 cm^{-1},[77] so these effects must also be considered in such a fullerene-rich material. Since these two effects are absent at low power densities, we perform high and low power measurements on the same crystal location to unambiguously assign the origin of the $A_g(2)$ peak shift in our spectra. At each power, consecutive spectra were measured to assess sample stability over time. The higher power density was $\sim$950 W/cm^2. Our low power density was $\sim$40 W/cm^2. For these measurements, several spots on sample crystals were subjected to high power first and low power second while others were exposed to the lower power first. The $A_g(2)$ modes were fit using Voigt functions in which the Gaussian width was set to the instrument resolution.

High power measurements produced peaks at 1469 ± 1 cm^{-1} and 1458.8 ± 0.9 cm^{-1}, while low power measurements showed peaks at 1470.3 ± 0.9 cm^{-1} and 1464.3 ± 1.9 cm^{-1}. The errors of the peak locations were determined from the standard deviations of fit results for spectra measured on different crystals and different days. Representative spectra are shown in Figure 2.11. Peak positions remained the same for high and low power measurements, regardless of whether the spot on the crystal was first subjected to a high or low power. Full fitting parameters can be found in Table 2.2 for the spectra in Figure 2.11, with the uncertainties in the table reflecting fit quality. This observation that the peak positions are reversible with laser power, combined with the expectation that polymerization is an

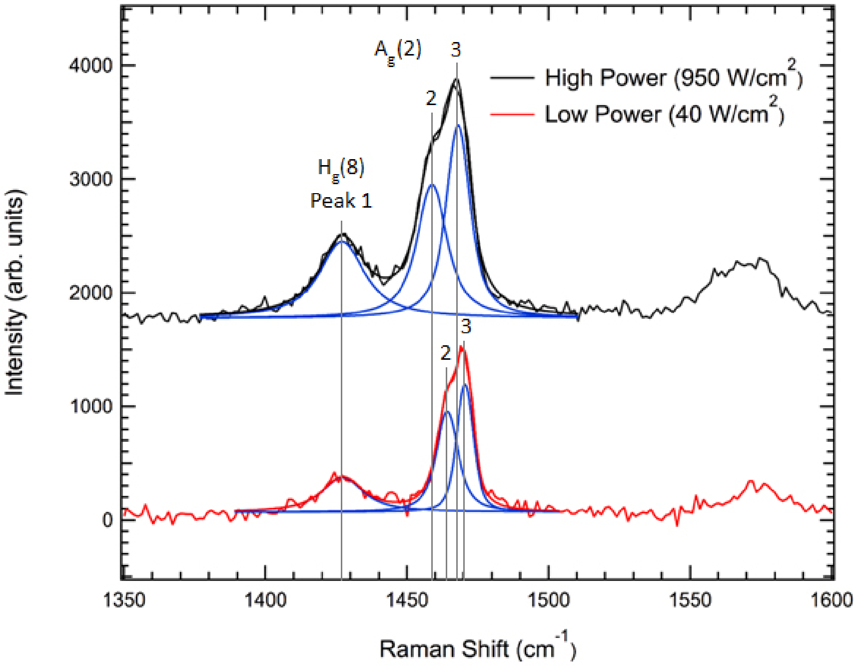

Figure 2.11: Representative spectra for high and low power measurements of the [$Co_6Se_8(PEt_2phen)_6$][C_{60}]$_5$ sample performed on the sample crystal location. The low power measurement was performed first. Peak 1, the H$_g$(8) mode of C_{60}, is included in the fit because it overlaps slightly with the A$_g$(2) pentagonal pinch mode. The black curve and red curves are for the high power density (950 W/cm^2) and low power density (40 W/cm^2) respectively. Fits are the overlaid in the same color, and fits of individual peaks are shown in blue.

irreversible process leads to the conclusion that the high power peak at 1458.8 cm^{-1} is caused by C_{60} excitation into the triplet state. The low power peak at 1464.3 cm^{-1} also indicates the presence of the triplet state, which can persist even for power densities of 40 W/cm^2.[77]

Table 2.2: Selected Raman spectroscopy data from the spectra in Figure 2.11.

	High Power			Low Power		
	Peak 1, $H_g(8)$	Peak 2, $A_g(2)$	Peak 3, $A_g(2)$	Peak 1, $H_g(8)$	Peak 2, $A_g(2)$	Peak 3, $A_g(2)$
Energy (cm^{-1})	1427.0 ± 0.3	1458.8 ± 0.4	1468.0 ± 0.2	1427.2 ± 0.6	1464.2 ± 0.5	1470.5 ± 0.3
Area	20000 ± 1000	22000 ± 3000	25000 ± 2000	8000 ± 1000	11000 ± 2000	10000 ± 2000
Lorentzian FWHM (cm^{-1})	17.6 ± 1.2	10.4 ± 1.0	7.35 ± 0.60	15.8 ± 2.2	6.1 ± 1.0	3.06 ± 0.77

Thus, we assign peaks shifts in these samples to C_{60} triplet state excitation, *not* charge-transfer. We observe no charge-transfer to the fullerenes from the molecular cluster in these materials. Interestingly, at each power there is a peak at 1470 cm^{-1}, which is likely originating from fullerenes more closely associated with the cluster. The fullerene layer is more likely to exhibit peak shifts to lower energy due to triplet state excitation because the layer more closely resembles solid C_{60}.

2.9 Optical absorption measurement

To measure mid-IR absorption spectrum, we used Fourier Transform Infrared (FT-IR) spectroscopy (Thermo Scientific Inc.). Each measurement was carried out on a single crystal flake

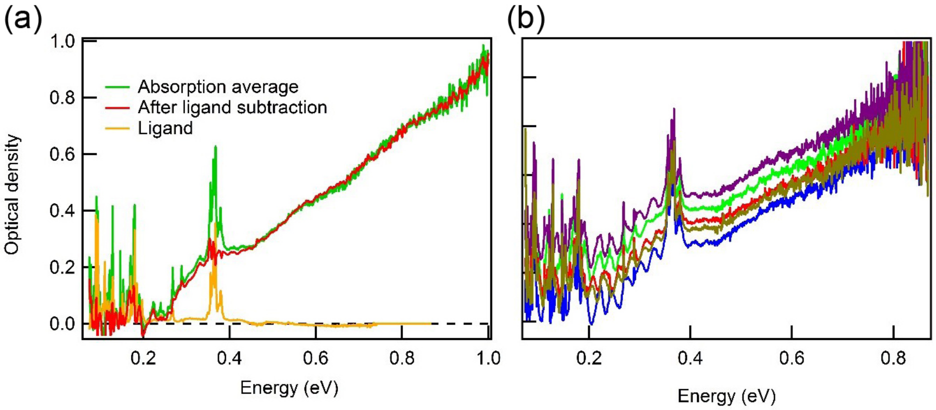

Figure 2.12: (a) Mid-IR optical absorption spectra of $[Co_6Se_8(PEt_2phen)_6][C_{60}]_5$ before (green) and after (red) ligand absorption subtraction. The result was an average from 5 different measurements on a single crystal flake from (b).

using transmission microscopic mode. The crystals were transferred onto a ZnSe substrate placing inside a cell with the KBr windows. During measurement and storage, samples were kept free from oxygen and moisture. The absorption spectrum (Figure 2.7b) was obtained by averaging 5 different measurements and subtracting the vibronic absorptions from the ligands (Figure 2.12).

The absorption coefficient is described by Elliot's theory for Wannier excitons as:[64]

$$\begin{aligned} a(\hbar\omega) =& \frac{\mu_{c\nu}^2}{\hbar\omega}\left[\sum_j \frac{2E_b}{j^3} sech\left(\frac{\hbar\omega - E_j^b}{\Gamma}\right)\right] \\ &+ \int_{E_g}^{\infty} sech\left(\frac{\hbar\omega - E}{\Gamma}\right)\frac{1}{1-e^{-2\pi\sqrt{\frac{E_b}{E-E_g}}}}\frac{1}{1-\frac{8\mu b}{\hbar^3}(E-E_g)}dE \end{aligned} \tag{2.1}$$

The first and second terms describe the Wannier exciton and bulk band-to-band transition, respectively.

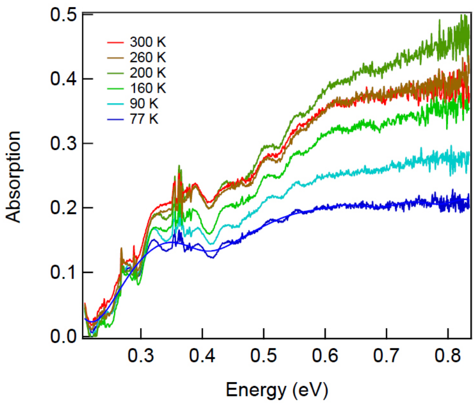

Figure 2.13: Absorption spectra of $[Co_6Se_8(PEt_2phen)_6][C_{60}]_5$ at different temperatures. The results were obtained using FT-IR via microscopic transmission mode. The crystals were transferred onto a ZnSe substrate placing inside a cryostat with two ZnSe windows. The blue-solid curve is a result from filtering out high oscillation frequencies at 77 K. The oscillation is resulted from Fabry-Perot interference pattern caused by two parallel surfaces in a thin crystal.

Where $\mu_{c\nu}^2$ is transition dipole moment, $\hbar\omega$ is photon energy, E_b is binding energy, $E_j^b = E_g - E^b/j^2$ are the energies of transitions to bound states, j is the exciton index, μ is exciton reduced mass.

We used the bulk part of the Elliot's theory with an additional Gaussian peak to fit the data:

$$a(\hbar\omega) = Ae^{-\left(\frac{\hbar\omega - E_1}{W}\right)^2} + \int_{E_g}^{\infty} sech\left(\frac{\hbar\omega - E}{\Gamma}\right) \frac{1}{1 - e^{-2\pi\sqrt{\frac{E_b}{E-E_g}}}} \frac{1}{1 - \frac{8\mu b}{\hbar^3}(E - E_g)} dE \quad (2.2)$$

Where the first term is a Gaussian function with a centered energy E_1 and a width W.

The joint valence-band energy-momentum dispersion is given by:

$$E_c(k) - E_\nu(k) = \frac{\hbar^2 k^2}{2\mu} - bk^4 + E_g \tag{2.3}$$

The result from Figure 2.7b was obtained using parameters: $E_b = 1$ meV, $E_g = 390$ meV, $\Gamma = 44$ meV, and $8\mu b/\hbar^3 = 0.7$

Chapter 3

Dimensional control in covalent frameworks of electroactive superatoms[1],[2]

3.1 Introduction

In this manuscript we explore the outer-sphere reaction chemistry of transition metal chalcogenide molecular clusters, species we have dubbed superatoms.[78–81] We show that we can incorporate functional groups in the ligands, and carry out chemical transformations using this functionality to form extended covalent solid-state compounds that are redox-active.

---

[1] This chapter is based on a manuscript prepared by Anouck M. Champsaur, Jaeeun Yu, Xavier Roy, Daniel W. Paley, Michael L. Steigerwald, Colin Nuckolls, and Christopher M. Bejger. My contribution to this study was focused on morphological characterization by SEM and chemical exfoliation of 2D framework.

[2] The revised manuscript is published on ACS Cent. Sci. **3**, 1050 (2017). Copyright 2017, American Chemical Society.

We have previously used superatoms to form solids from two electronically complimentary building blocks, directed-layer fullerene assemblies from phenanthrene-decorated clusters, and covalent assemblies through directed ligand exchange.[3, 5, 82, 83] For the superatom-assembly chemistry needed here, we tailor the chemical properties of the superatom by manipulating the reactivity of its ligand shell without disrupting the cluster core. We convert the $Co_6Se_8[PEt_2(4\text{-}C_6H_4Br)]_6$ superatom into one that presents six carboxylic acids that assemble into a three-dimensional solid held together by hydrogen bonds. We further modify this assembly by replacing the hydrogen bonds with covalent zinc carboxylate bonds to produce two types of framework materials, a trigonal framework ($\mathbf{F_{3D}}$) and a tetragonal framework ($\mathbf{F_{2D}}$) (Figure 3.3). Single crystal X-ray diffraction (SCXRD) reveals that $\mathbf{F_{3D}}$ is a three-dimensional covalent network of superatoms held together with zinc carboxylate bonds, but $\mathbf{F_{2D}}$ forms two-dimensional sheets that then stack through non-covalent forces into a three dimensional solid. Remarkably, we find that we can chemically exfoliate the two-dimensional sheets of $\mathbf{F_{2D}}$, and cast them onto arbitrary substrates. When we cast them on electrodes surfaces, they retain the redox activity of the superatom building blocks.

3.2 Design of superatom with chemical functionality

To create the superatom building blocks, $Co_2(CO)_8$ and Se are treated with $Et_2P(4\text{-}C_6H_4Br)$ to give $Co_6Se_8[PEt_2(4\text{-}C_6H_4Br)]_6$ (SCXRD in Figure 3.1a) in high yield. Other than the obvious differences in the size, shape, and arrangement of the organic components, the inorganic core of $Co_6Se_8[PEt_2(4\text{-}C_6H_4Br)]_6$ is identical to the parent cluster, $Co_6Se_8(PEt_3)_6$.[10] Through a six-fold lithium/halogen exchange followed by the addition of CO_2 gas and sub-

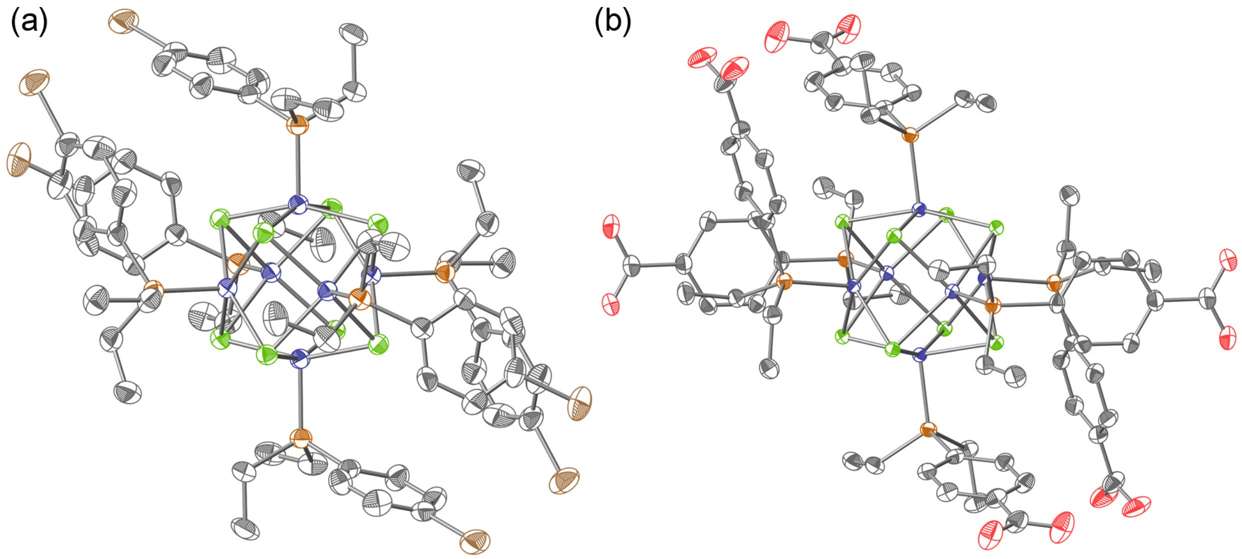

Figure 3.1: Solid state molecular crystal structure of (a) $Co_6Se_8[PEt_2(4\text{-}C_6H_4Br)]_6$ and (b) $Co_6Se_8[PEt_2(4\text{-}C_6H_4COOH)]_6$ (**1**). Carbon, black; oxygen, red; bromine, brown; cobalt, blue; selenium, green; phosphorus, orange. Thermal ellipsoids are set at 50% and hydrogen atoms are omitted to clarify the view.

sequent acidification, we converted each Br in this compound to the corresponding carboxylic acid to yield the nanosized octahedral, superatom building block $Co_6Se_8[PEt_2(4\text{-}C_6H_4COOH)]_6$ (**1**).

We determined the molecular structure of **1** using SCRXD (Figure 3.1b). Rather than simply crystallizing into a molecular solid, **1** assembles into a three-dimensional solid via extensive and ordered hydrogen bonding between carboxylic acids on neighboring clusters (Figure 3.2a). If we represent each cluster as a sphere, we see that this solid forms as a simple-cubic framework in which there is hydrogen-bonding between nearest neighbors (Figure

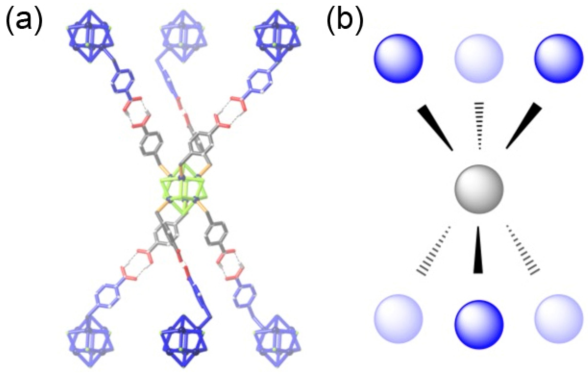

Figure 3.2: (a) **1** forms a three-dimensional hydrogen-bond network, named **1-H**. View of **1-H** down the a-axis, showing a single superatom and its six hydrogen-bonds to neighboring superatoms (in blue). (b) Representation of the view in (a) with each superatom as a sphere to emphasize the framework structure.

3.2b). In order to emphasize the difference between the superatom and the superatom-solid, we refer to the latter as **1-H**. The formation of this solid-state compound is reversible: **1-H** dissolves in tetrahydrofuran to regenerate **1**.

The cohesive network of hydrogen-bonds that produces **1-H** from **1** prompted us to study the hexacarboxylic acid species **1** and determine whether carboxylate-zinc bonds could replace the hydrogen-bonds of **1-H** in a reaction reminiscent of metal-organic frameworks (MOFs) to form new framework solids with porosity and/or lower dimensionality.[84] MOFs are extended, polymeric networks built from multi-coordinated metal sites and multitopic organic linker ligands.[85–88] Typically a MOF results from the reaction of an organic carboxylate ligand with a metal salt such as $Zn(NO_3)_2$. New designs for MOFs have created multi-functional materials by incorporating conductive/magnetic components into the

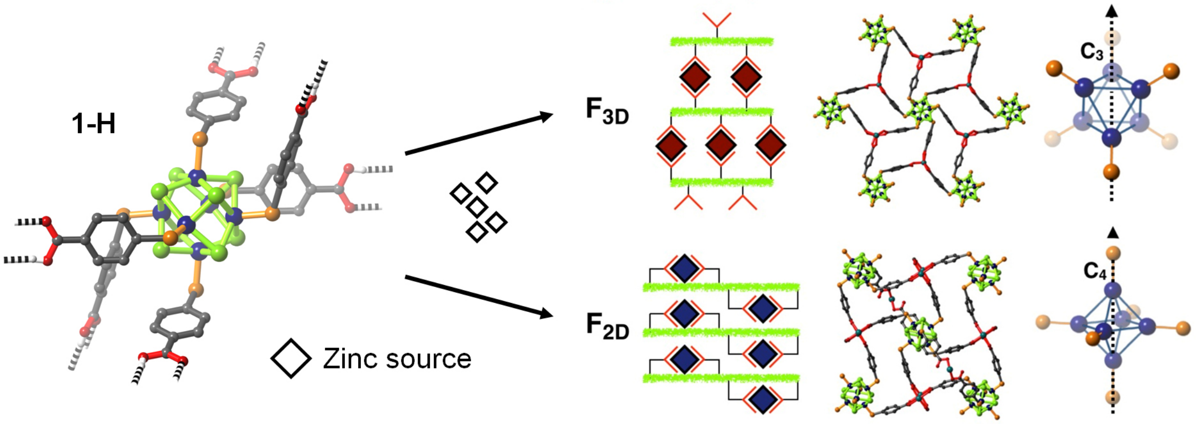

Figure 3.3: In $\mathbf{F_{3D}}$ the superatoms are held together within a two-dimensional plane to create a trigonal arrangement of superatoms, and the planes extend in three dimensions via further zinc carboxylate bonds. The axis of symmetry defining a superatom within an $\mathbf{F_{3D}}$ sheet is a C_3-axis through the center of two planes defined by Co_3 atoms. In $\mathbf{F_{2D}}$ the superatoms are held together within a two-dimensional plane to create a distorted square arrangement. The two-dimensional layers are non-covalently stacked in the third dimension. The axis of symmetry defining the $\mathbf{F_{2D}}$ plane is a C_4-axis through axial atoms of a Co_6 octahedron.

framework,[89–103] and a variety of techniques have been developed to prepare thin porous films.[104, 105] Co_6Se_8 superatoms are useful building blocks for such frameworks because they have tunable ligands, multiply accessible redox states, significant magnetic moments, and charge transport capabilities.[3, 5, 10, 82] Our building block **1** is preformed and atomically defined, and thus programmable.

Using the same building blocks, **1** and Zn^{2+}, we can selectively synthesize two different framework solids, $\mathbf{F_{3D}}$ and $\mathbf{F_{2D}}$, by varying the growth conditions (Figure 3.3). Remarkably, we were able to obtain structures for both frameworks using SCXRD (details of the refinement can be found in Section 3.9.1). In both frameworks, all the carboxylic acid hydrogen bonds of **1-H** are replaced by carboxylate-zinc-carboxylate nodes. SCXRD of both solids reveals that while they have the same Zn:[Co_6Se_8] stoichiometric ratio of 3:1, both the dimensionality of their extended structure and orientation of the cluster within the framework differ significantly. $\mathbf{F_{3D}}$ is a three-dimensional network while $\mathbf{F_{2D}}$ is a two-dimensional structure with strong covalent in-plane bonding and comparatively weak non-covalent inter-layer interactions.

3.3 Three-dimensional covalent network

To synthesize $\mathbf{F_{3D}}$, we reacted **1** and $Zn(NO_3)_2$ in a DMF/MeOH solvent mixture under solvothermal conditions at 65 °C, and obtained black hexagonal crystals after 24 h. Figure 3.4 displays the crystal structure of $\mathbf{F_{3D}}$. The structure is a covalent network in which **1** is coordinated to unusual trinuclear zinc nodes in three dimensions (Figure 3.4a). Looking down the *b*-axis we clearly see the distinct trigonal layers of the framework (Figure 3.4b). Within each layer, the superatoms are bound to six zinc-nodes (Figure 3.4c). These layers are then crosslinked by a single Zn-O bond. The 3-fold symmetry of the trigonal lattice of $\mathbf{F_{3D}}$ arises because the Co_6 octahedron is tilted on its face in the layer, which orients the phosphines such that three point up and three point down (Figure 3.4d). This symmetry mirrors that of **1-H**, replacing hydrogen bonds with an organized trinuclear metal node (labeled Zn1, Zn2, and Zn3 in Figure 3.4e). Unusual trinuclear zinc nodes have been reported previously.[106, 107]

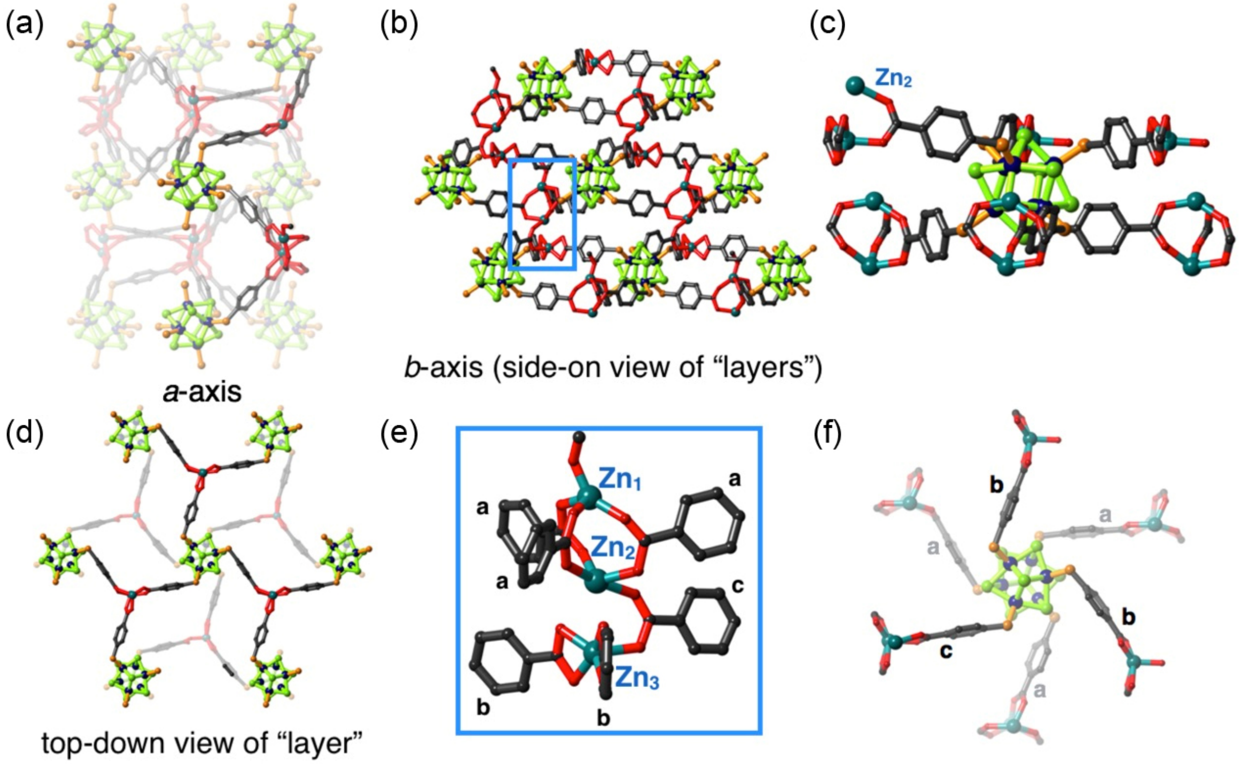

Figure 3.4: Structure of $\mathbf{F_{3D}}$ from SCXRD: a three-dimensional covalent network synthesized from the solvothermal reaction of **1** and $Zn(NO_3)_2$ in a MeOH/DMF solvent mixture. Ethyl groups are omitted for clarity. (a) View of the network along the *a*-axis. (b) View along the *b*-axis of the crosslinked pseudotrigonal arrays of superatoms. The blue box highlights the trinuclear zinc node, which is magnified in (e). (c) Side-on view of **1** within a pseudotrigonal layer and (d) top-down view of a single "layer" within $\mathbf{F_{3D}}$. (e) View of the metal node geometry and different coordination environments around Zn1, Zn2, and Zn3. The blue box around this trinuclear zinc node is the same as in the inset in (b). (f) Top-down view of a single cluster within an $\mathbf{F_{3D}}$ layer surrounded by three different Zn-carboxylate binding modes. Three types of carboxylates are shown: **a**, **b**, and **c**.

Each zinc atom in $\mathbf{F_{3D}}$ exhibits a different coordination environment. Zn1 and Zn2 display distorted tetrahedral geometry and together form a three-bladed trigonal paddlewheel with three bridging μ_2-carboxylates. A solvent molecule (likely MeOH) coordinates Zn1 axially, and Zn2 is axially coordinated by a μ_2-carboxylate, whose second oxygen coordinates Zn3. Zn3 exhibits a distorted square pyramidal geometry. Each superatom **1** within the framework contains three types of carboxylates, labeled **a**, **b**, and **c** in Figures 3.4e and 3.4f. For **a**, three μ_2-carboxylates form the Zn1-Zn2 paddlewheel; for **b**, two carboxylates coordinate Zn3 in an η_2 fashion; for **c**, a μ_2-carboxylate coordinates both Zn3 and Zn2. The latter ligand c also serves to crosslink the layers through its carboxylate-Zn2 bond. This bond has a length of 2.22 Å, which is a long Zn-O contact[3]. It suggests the inter-layer carboxylate-Zn2 bond is a weaker, dative bond compared to covalent intra-layer carboxylate-Zn bonds.

3.4 Layered two-dimensional material

Because of the weak inter-layer zinc bonds in $\mathbf{F_{3D}}$ and to explore the generality of this approach where we replace the proton nodes of **1-H** with zinc carboxylates, we reacted **1** and $Zn(NO_3)_2$ at 65 °C in a DMF/EtOH solvent mixture and obtained black cubic crystals after 24 h. We note that a small fraction of $\mathbf{F_{3D}}$ forms under these conditions but can be eliminated with the addition of "extra" protons in the form of HCl in the reaction. Under these conditions, we form exclusively the new solid-state compound, $\mathbf{F_{2D}}$ (Figure 3.5). $\mathbf{F_{2D}}$ also contains complete replacement of proton-nodes with metal nodes, although the types

---

[3] The Cambridge Structural Database was searched using *ConQuest*[108] to identify 3855 examples of Zn_2 units bridged by carboxylates. The average Zn-O distance is 2.02 ± .09 Å.

of metal nodes and dimensionality differs from $\mathbf{F_{3D}}$. Distinct layers of superatoms are held together only by non-covalent forces.

$\mathbf{F_{2D}}$ is a layered two-dimensional material in which each layer is a square arrangement of Co_6Se_8 superatoms with four phosphine ligands residing in the 2D plane and bonding to four-bladed Zn-carboxylate paddlewheels (Figure 3.5a). In the direction normal to the sheet, the axial carboxylate ligands coordinate an additional Zn^{2+} ion that is positioned above or below the square sheet (Figure 3.5b). Figures 3.5c and 3.5d display the binding interaction of each ligand of **1** within the framework. The zinc subunit within the square plane of this framework is a dinuclear four-bladed Zn-carboxylate paddlewheel (Figure 3.5e). The combination of two Zn^{2+} ions and four bridging μ_2-carboxylate groups yields this Zn_2 cluster with a Zn-Zn distance of 2.867(7) Å that is consistent with other such "four-bladed" paddlewheels in zinc-based metal-organic frameworks.[109] Pairs of apical phosphines on adjacent clusters that are not involved in dinuclear Zn paddlewheels within a single layer are covalently linked via a single Zn atom (in addition to their covalent linkage via the intra-layer Zn_2 node) to form a mononuclear zinc complex. This complex features Zn-O distances of 2.20(3) and 2.36(3) Å and a carboxylate-Zn-carboxylate angle of approximately 119 °. This geometry is typical of pseudotetrahedral $Zn(O_2R)_2L_2$ complexes[4] but in this case we note that the two L-type ligands (presumably ethanol or water) are disordered and could not be located. The layers are self-contained and stack through non-covalent inter-layer interactions

---

[4] The Cambridge Structural Database was searched using *ConQuest*[108] to identify 140 examples of $Zn(O_2R)_2L_2$ complexes where the carboxylates are η^2 and the L ligands bind through O or N. Among these examples, the average angle between the two O_2CR ligands (measured C-Zn-C) is 115 ± 12 °. The average Zn-O distance (each bond measured individually) is 2.21 ± 0.18 Å and the average after taking the mean of all four bonds in a single molecule is 2.21 ± .05 Å. Therefore, the RCO_2-Zn-O_2CR angle of 119 ° and Zn-O distances of 2.14 and 2.37 Å are consistent with previously reported structures.

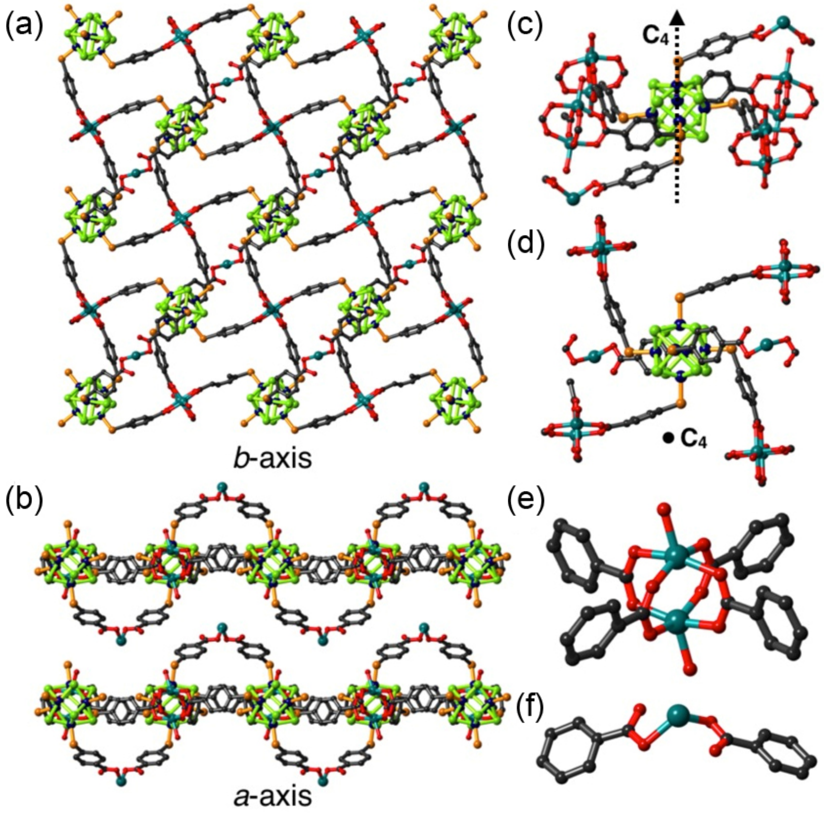

Figure 3.5: Structure of $\mathbf{F_{2D}}$ from SCXRD: square sheets in the crystalline state. $\mathbf{F_{2D}}$ is two-dimensional covalent network synthesized from the solvothermal reaction of **1** and $Zn(NO_3)_2$ in a EtOH/DMF solvent mixture. Ethyl groups are omitted for clarity. (a) Top-down view of a single layer within $\mathbf{F_{2D}}$ along the *b*-axis. (b) Side-on view of $\mathbf{F_{2D}}$ layers along the *c*-axis. Non-covalent forces hold the layers together in the third dimension. (c) Single superatom in an $\mathbf{F_{2D}}$ layer and the binding interaction of each carboxylate of **1**. Within the two-dimensional framework plane, each of the four equatorial carboxylate ligands coordinates two Zn^{2+} ions, forming the four-bladed paddlewheel upon coordination of equatorial carboxylate ligands of three adjacent superatoms. The axial carboxylate ligands coordinate an additional Zn^{2+} ion that lies just above or below the square sheet. (d) Top-down view of **1** within the framework plane. (e) Four-bladed Zn^{2+} paddlewheel. (f) Mononuclear zinc complex.

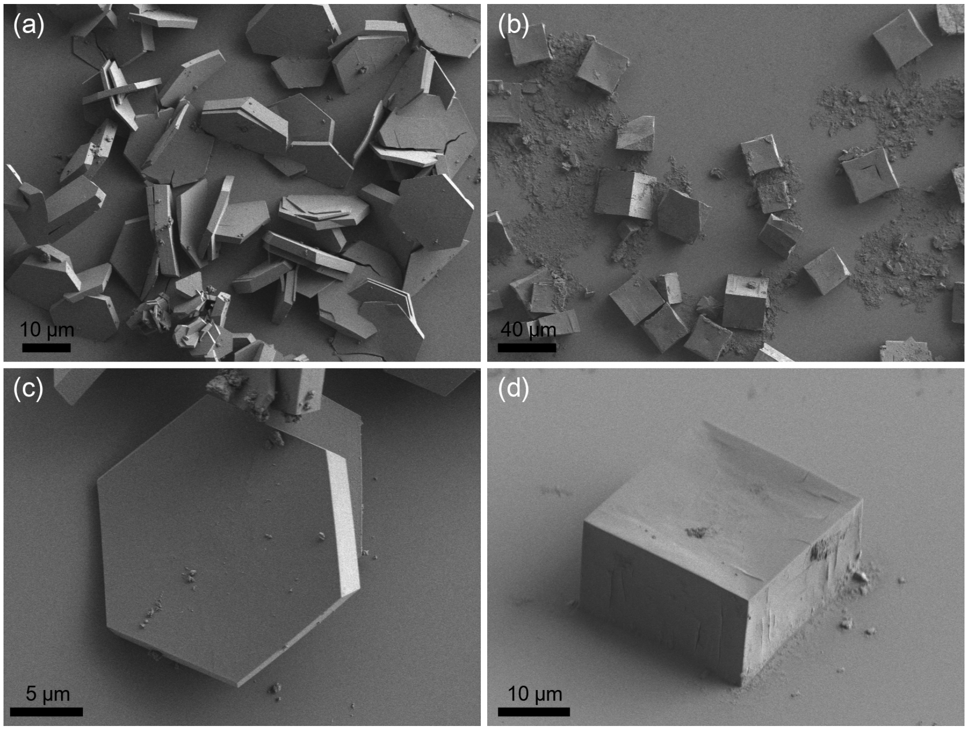

Figure 3.6: SEM images of (a,c) $\mathbf{F_{3D}}$ hexagonal crystals and (b,d) $\mathbf{F_{2D}}$ cubic crystals as synthesized.

in an eclipsed arrangement.

3.5 Structural and chemical analyses of frameworks

The crystal packing arrangements of $\mathbf{F_{3D}}$ and $\mathbf{F_{2D}}$ are propagated in their macroscopic crystal morphologies. Structural and chemical analyses were performed by employing scanning electron microscopy (SEM) and energy-dispersive X-ray spectroscopy (EDX). Figure 3.6 shows SEM micrographs of the crystals that form after 24 h growth. The hexagonal

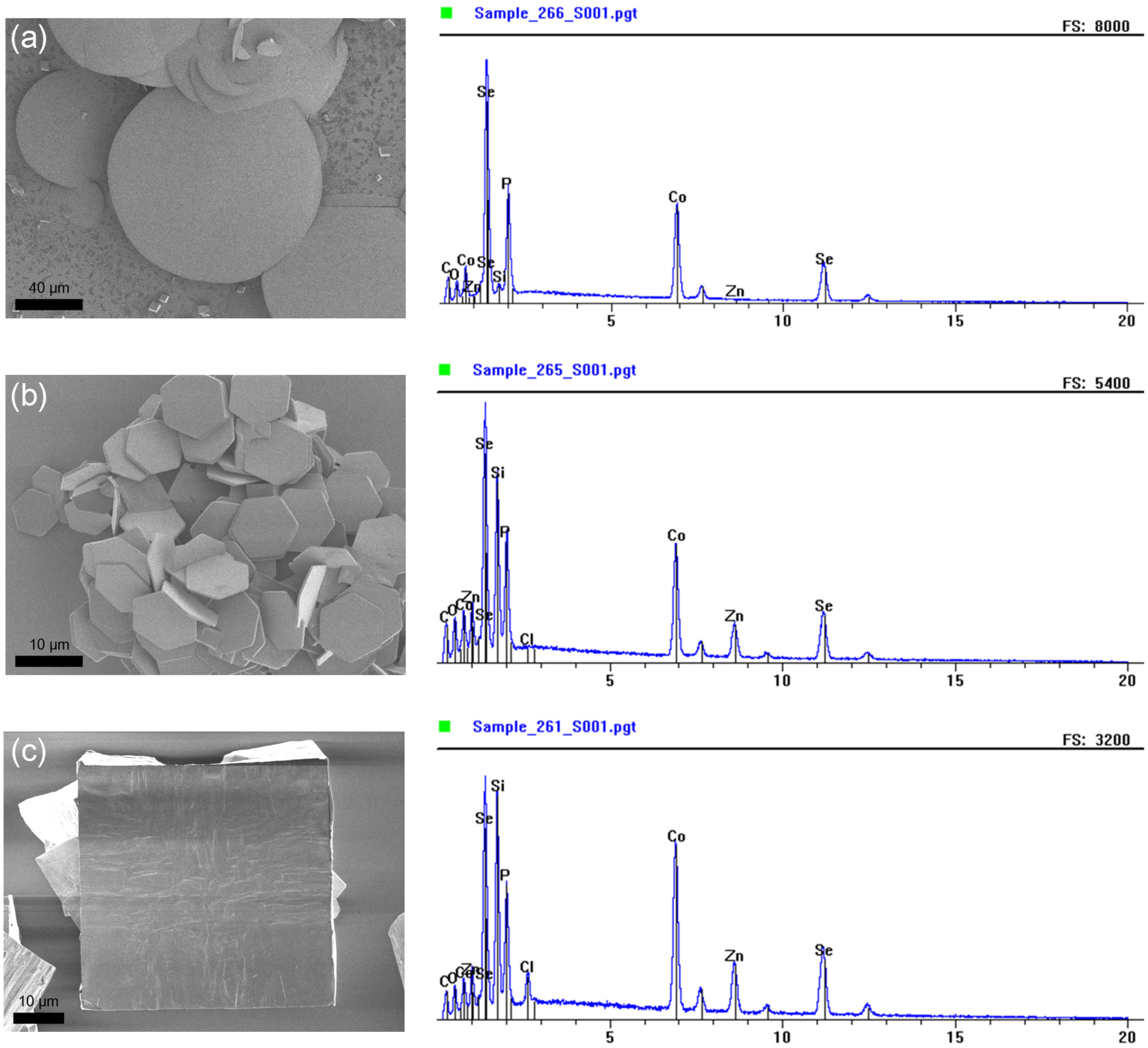

Figure 3.7: SEM images and corresponding EDX spectra of (a) $Co_6Se_8[PEt_2(4\text{-}C_6H_4COOH)]_6$ (**1**), (b) 3D framework $\mathbf{F_{3D}}$, and (c) 2D framework $\mathbf{F_{2D}}$. For all EDX spectra, the Si signal arises from the substrate. EDX spectra indicate the presence of Co and Se for all compounds. As expected, the Zn peak is missing from starting material **1**, but a Zn peak is present in both frameworks $\mathbf{F_{3D}}$ and $\mathbf{F_{2D}}$ due to the presence of coordinated zinc complexes.

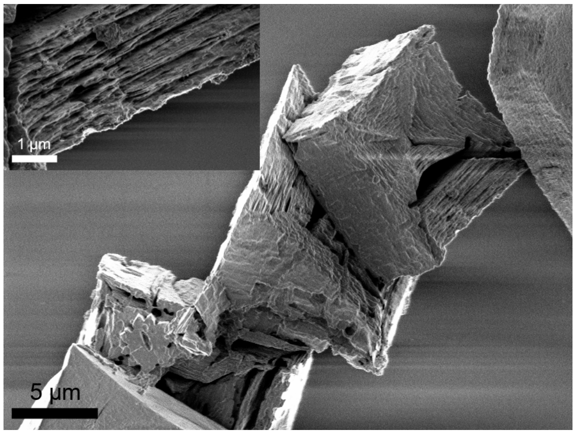

Figure 3.8: SEM images of cubic crystals of $\mathbf{F_{2D}}$ immersed in a benzoic acid solution in DMF. Striations in the crystals are apparent.

plates ($\mathbf{F_{3D}}$; Figure 3.6c) and black cubes ($\mathbf{F_{2D}}$; Figure 3.6d) reflect the trigonal and square lattices of their crystalline arrangements. In $\mathbf{F_{3D}}$, the cluster is tilted on its side such that the symmetry is defined by a C_3-axis through the offset triangular stacks of Co_3, whereas in $\mathbf{F_{2D}}$ a C_4-axis through the axial cobalt atoms of the Co_6 octahedron generates a square lattice. EDX spectra of both samples (Figure 3.7) display zinc, cobalt, and selenium as compared to the EDX spectrum of **1** that lacks Zn peaks. Powder XRD of each sample shows homogeneous crystalline phases (Figure 3.14 in Section 3.9.2).

3.6 Chemical exfoliation of F_{2D} crystals

We were curious to see whether the two-dimensional $\mathbf{F_{2D}}$ crystals would behave like traditional "atomic" layered compounds. In particular, can we exfoliate these materials without having the layers themselves disintegrate? We reasoned that a weakly acidic solution would

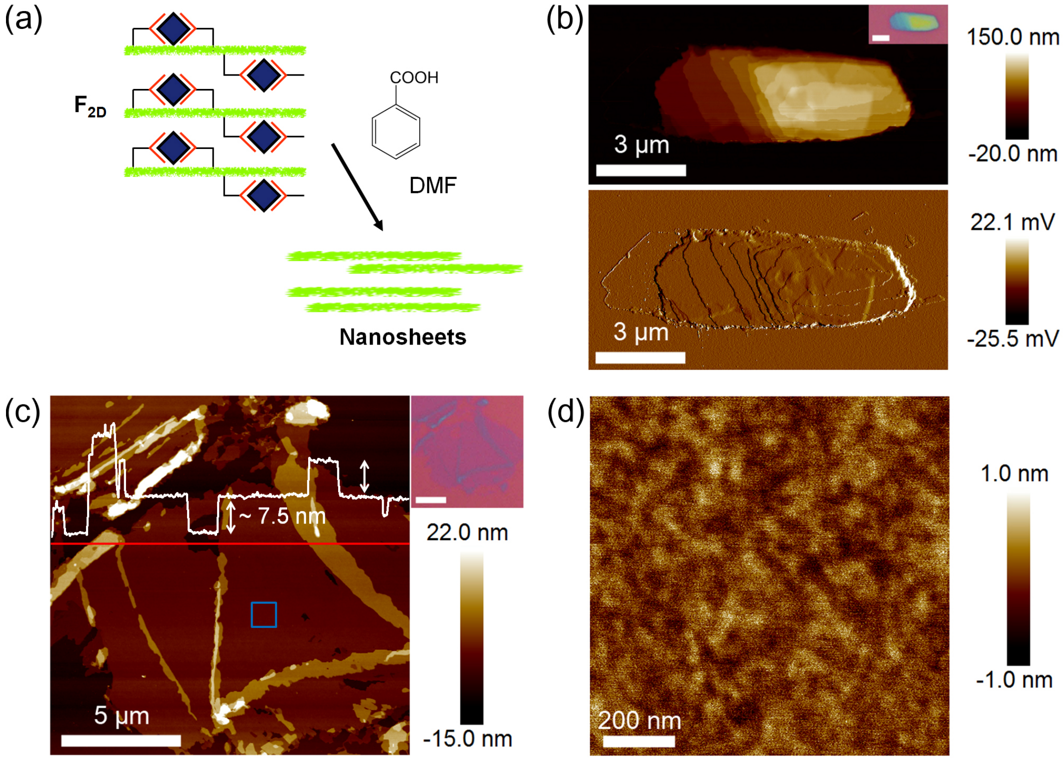

Figure 3.9: (a) Chemical exfoliation of **F$_{2D}$**. (b) AFM height sensor and peak force error images of multilayered **F$_{2D}$** films after immersion in benzoic acid solution in DMF. The scale bar in an inset is 3 μm. (c) AFM topographic image of exfoliated sheets. Sheets remain that are about 7.5 nm in thickness, with distinct step sizes apparent. The scale bar in an inset is 5 μm. (d) AFM image of the surface of exfoliated **F$_{2D}$**. The surface is clean and flat, with a roughness of 0.3 nm. The area imaged by AFM is indicated by the blue square in (c).

chemically exfoliate the layers of $\mathbf{F_{3D}}$ and that they would be stable to these conditions having been formed in acidic conditions. We first immersed the cubic crystals of $\mathbf{F_{2D}}$ in a 1 mM solution of benzoic acid in DMF. SEM micrographs of immersed cubes show visible layered striations within the crystals (Figure 3.8). Next, we immersed the $\mathbf{F_{2D}}$ crystals in 40 mM benzoic acid overnight and followed the transformation with powder X-ray diffraction (Figure 3.15 in Section 3.9.2). The reflections that are due to $\mathbf{F_{2D}}$ disappear, with only low intensity peaks corresponding to trace impurities of $\mathbf{F_{3D}}$ still visible. During this process, we observe a color change in the solution from clear to light brown upon suspension in the benzoic acid solution. We dropcasted this solution on a silicon substrate (SiO_2 on Si) substrates and characterized the films with optical microscopy and atomic force microscopy (AFM). Figures 3.9b and 3.10 clearly show layered two-dimensional sheets. Thin sheets with a thickness of 7.5 nm are present throughout the samples (Figure 3.9c and 3.11a), with step sizes between the layers corresponding to this thickness. From the SCXRD structure of $\mathbf{F_{2D}}$, the expected thickness of a single sheet is 1.5 nm, corresponding to the Zn-Zn distance between stacked mononuclear Zn atoms in adjacent layers. Thus, 7.5 nm corresponds to five distinct superatom framework layers. In other images we also observe smaller step sizes of 3.8 nm and 5.3 nm (Figure 3.11), corresponding to SCXRD of three layers and four layers, respectively. These chemically exfoliated sheets of $\mathbf{F_{2D}}$ once deposited onto a substrate are clean and flat (Figure 3.9d, a roughness of 0.3 nm).

We can use these thin layers of $\mathbf{F_{2D}}$ from solution to coat the surface of electrodes to probe their redox-activity. For comparison, **1** displays three reversible oxidations relative to Fc/Fc^+ (Figure 3.12a) and the bulk crystals deposited on the electrode show two broad, quasi reversible oxidations (Figure 3.12b). When we dropcast the exfoliated sheets onto

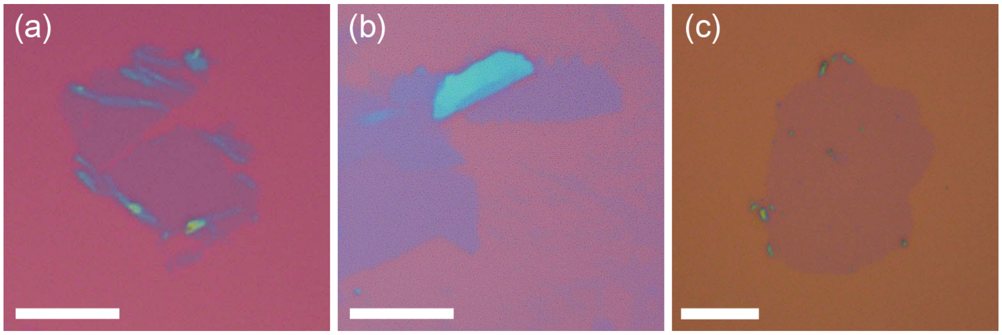

Figure 3.10: Optical images of chemically exfoliated $\mathbf{F_{2D}}$ sheets on Si/SiO$_2$ substrates. Scale bars are 10 μm. Exfoliated sheets are typically around 7.5 nm in thickness.

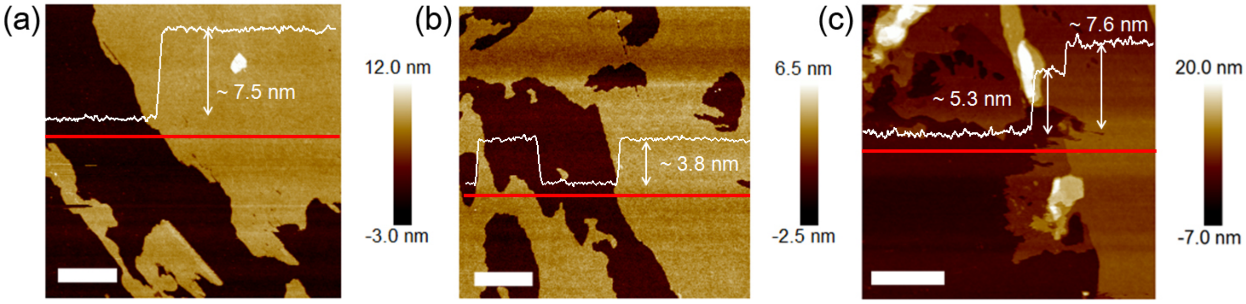

Figure 3.11: AFM topographic images and height profiles of chemically exfoliated $\mathbf{F_{2D}}$ sheets. Scale bars are 1 μm.

a glassy carbon electrode. The cyclic voltammogram of the exfoliated $\mathbf{F_{2D}}$ sheets (Figure 3.12c) reveals that the redox properties of the superatom building block **1** persists within the sheets as they display three reversible oxidations. Another interesting feature of the cyclic voltammetry (CV) of the electrodes that are covered with the 2D superatom frameworks of $\mathbf{F_{2D}}$ is that are permeable to the electrolyte. The onset of the peaks and peak separations of the exfoliated $\mathbf{F_{2D}}$ sheets are similar to these values for **1**, we assign similar charged states for **1** within $\mathbf{F_{2D}}$. The important finding is that $\mathbf{F_{2D}}$ sheets are solution processable, porous, and redox-active.

3.7 Conclusion

We have developed the reaction chemistry to create the hexatopic $Co_6Se_8[PEt_2(4\text{-}C_6H_4COOH)]_6$ superatom **1**. This superatom assembles into a three-dimensional framework that is held together by hydrogen bonds between superatoms. From this building block we create covalent, crystalline frameworks $\mathbf{F_{3D}}$ and $\mathbf{F_{2D}}$ from the solvothermal reaction of **1** with $Zn(NO_3)_2$. A seemingly small change in the solvent system from DMF/methanol to DMF/ethanol yields remarkable changes in crystal morphology and structure, from a three-dimensional to a two-dimensional framework. Both frameworks are held together via zinc-carboxylate bonds. Two-dimensional $\mathbf{F_{2D}}$ can be chemically exfoliated to yield ultrathin yet soluble layers. These layers can be deposited from solution onto substrates. The sheets are redox-active, preserving the redox activity of their component superatoms. These types of porous, ultrathin, and electroactive sheets will find utility in a number of other applications such as modified electrodes for catalysis, batteries, and nanoscale electronic

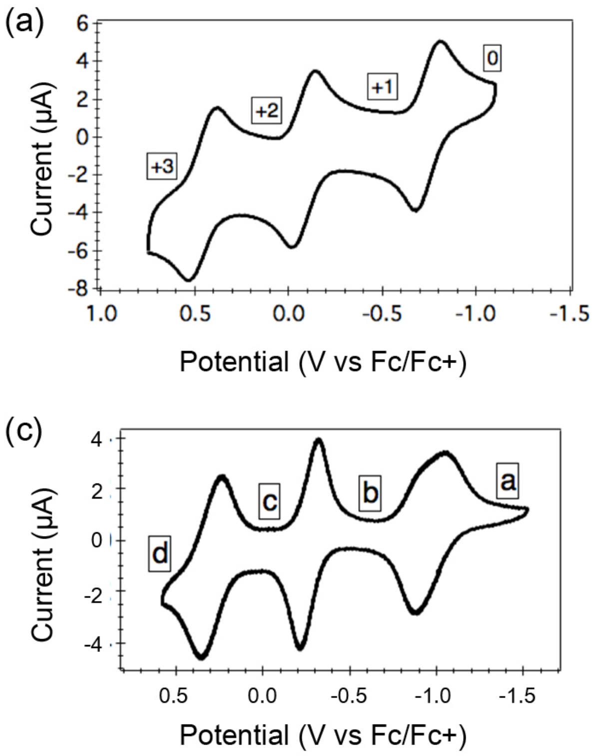

Figure 3.12: (a) Cyclic voltammogram of **1** in 0.1 M TBAPF$_6$ in tetrahydrofuran with a 150 mV/s scan rate. The superatom is neutral as synthesized and displays three reversible oxidations. (b,c) Solid-state cyclic voltammogram of (b) $\mathbf{F_{2D}}$ crystals and (c) exfoliated $\mathbf{F_{2D}}$ sheets. A suspension of $\mathbf{F_{2D}}$ crystals in ether was dropcasted onto the glassy carbon electrode and allowed to dry. The crystals or sheets stuck to the electrode surface. The electrode was immersed in a 0.1 M TBAPF$_6$ solution in tetrahydrofuran and the cyclic voltammogram was acquired as usual, with a 50 mV/s scan rate. The voltammogram is labeled a-d and these events roughly align with oxidation states of **1** although they are slightly offset.

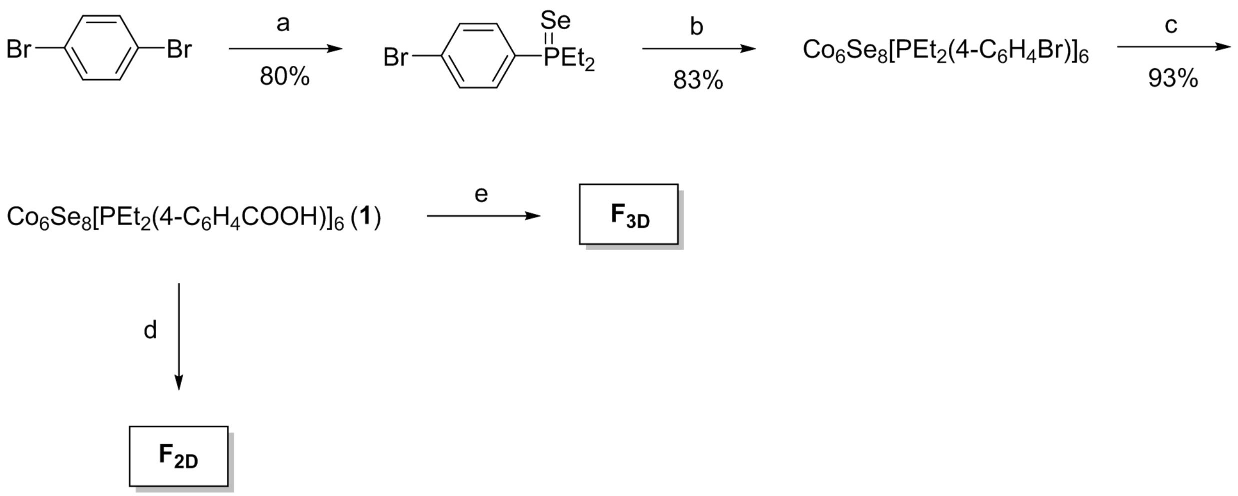

Figure 3.13: Synthetic scheme for $Co_6Se_8[PEt_2(4\text{-}C_6H_4COOH)]_6$ (**1**) and crystalline frameworks.

sieves.

3.8 Synthesis and characterization information

3.8.1 Synthetic details

All reactions were performed in a nitrogen atmosphere using standard Schlenk techniques. Selenium powder and dicobalt octacarbonyl (stabilized with 1-5% hexane) were obtained from STREM Chemicals. All other reagents were purchased from Sigma-Aldrich. Chemicals were used without further purification. Anhydrous and anaerobic solvents were obtained from a Glass Contour solvent system consisting of a Schlenk manifold with purification columns packed with activated alumina and supported copper catalyst. DMF, ethanol, and methanol (used for framework synthesis) were purchased as anhydrous bottles, degassed, and stored over 4 Åmolecular sieves in the glovebox.

(4-Bromophenyl)diethylphosphineselenide

n-BuLi (1.6 M in n-hexane, 20.0 mL, 32.05 mmol, 1.0 eq.) was added dropwise at -78 °C under N_2 to a stirred solution of 1,4-dibromobenzene (7.56 g, 32.05 mmol, 1.0 eq.) in anhydrous THF (90 mL). The mixture was stirred at -78 °C for 1 h and then chlorodiethylphosphine (4.00 g, 32.12 mmol, 1.0 eq.) was added dropwise. The resulting mixture was gradually warmed to room temperature overnight. The solvent was removed *in vacuo* and anhydrous toluene was added to the reaction flask. The mixture was stirred for 1 h and Schlenk filtered via cannula transfer into a flask charged with selenium powder (3.00 g, 37.99 mmol, 1.2 eq.). This solution was stirred under N_2 at 60 °C for 1 h and filtered hot in air. The solution was dried *in vacuo* and the resulting yellow oil was subject to silica gel column chromatography (hexanes/dichloromethane = 3:2) to yield (4-bromophenyl)diethylphosphineselenide as a clear off-white oil (8.347g, 80 %).

^{1}**H NMR** (300 MHz, chloroform-d): δ 7.75 (dd, J = 11.7, 8.4 Hz, 2H), 7.62(dd, J = 8.5, 2.2 Hz, 2H), 2.21 (m, 4H), 1.11 (dt, J = 20.2, 7.5 Hz, 6H)

^{31}**P NMR** (202 MHz, chloroform-d): δ 43.53.

FTIR (cm^{-1}): 2970, 2933, 1692, 1572, 1392, 1068, 1007, 815, 776.8

HRMS (FAB+): calculated for $C_{10}H_{15}BrPSe$ 322.9259, observed 322.9269

$Co_6Se_8[PEt_2(4\text{-}C_6H_4Br)]_6$

(4-Bromophenyl)diethylphosphineselenide (2.039 g, 6.29 mmol, 4.2 eq.) was placed in a

Schlenk flask under N_2 and dissolved in anhydrous toluene (20 mL). Dicobalt octacarbonyl (0.512 g, 1.50 mmol, 1 eq.), dissolved in 10 mL toluene, was added to the solution and the reaction was heated to 120 °C for 24 h with a reflux condenser. The solvent was removed *in vacuo* and the solids were brought inside the glovebox. The oily product was dissolved in 15 mL toluene and filtered. The remaining dark brown solid was washed with pentane and dried, yielding $Co_6Se_8[PEt_2(4\text{-}C_6H_4Br)]_6$ (1.014 g, 83 % based on $Co_2(CO)_8$). This cluster is red when dissolved. When the reaction is not complete, another species is present, $Co_4Se_2[(CO)_3]_6(PEt_2PhBr)_4$ (determined crystallographically) which is dark green in solution. Molecular structure displayed in Figure 3.1a.

^{1}**H NMR** (500 MHz, benzene-d_6): δ 7.75 (d, 2H), 7.62(t, 2H), 2.01 (m, 4H), 0.91 (dt, 6H)

^{31}**P NMR** (161.9 MHz MHz, benzene-d_6): δ 57.95 (broad)

$Co_6Se_8[PEt_2(4\text{-}C_6H_4COOH)]_6$ (1)

$Co_6Se_8[PEt_2(4\text{-}C_6H_4Br)]_6$(0.412 g, 0.17 mmol, 1 eq.) was placed in a Schlenk flask under N_2 and dissolved in anhydrous THF (40 mL). The solution was cooled to -78 °C and n-BuLi (2.5 M in n-hexane, 0.40 mL, 1.0 mmol, 6 eq.) was added dropwise over 5 minutes. The reaction was stirred for 15 minutes. Carbon dioxide was bubbled through the solution for 5 minutes. The reaction was kept at -78 °C for 30 minutes. The cold bath was removed and the reaction was warmed to room temperature over 1-2 h. The solvent was removed *in vacuo*. In the glovebox, the remaining reddish brown solids were triturated with diethyl ether, then THF. The solids were then suspended in 15 mL THF and acidified with 2 M HCl in diethyl ether (2 mL). The deep red solution was filtered and the solvent was removed *in vacuo*. The remaining solid was triturated with diethyl ether and acetonitrile, then dried to yield **1** as a reddish brown solid (0.351 mg, 93 %). Molecular structure displayed in Figure 3.1b.

^{1}**H NMR** (500 MHz, THF-d_8): δ 10.71 (s, 1H), 8.38-8.08 (m, 2H), 8.00 (dd, 2H), 2.26 (m, 4H), 1.11 (dt, 6H)

^{31}**P NMR** (202 MHz, THF-d_8): δ 43.99

FTIR (cm^{-1}): 3000-2700 (br-OH), 2974, 1692, 1423, 1294,1095, 1013, 922, 858

$\mathbf{F_{3D}}$

Compound **1** (20 mg, 8.90 mmol, 1 eq.) was dissolved in 5 mL DMF. Zinc nitrate hexahydrate (13 mg, 43.70 mmol, 4.9 eq.) was dissolved in 5 mL MeOH. The two solutions were mixed, filtered and placed in a 20 mL scintillation vial. The vial was sonicated for 5 minutes, placed in an oven, and heated to 65 °C for 24 hours. After cooling to room temperature, the supernatant was removed and the hexagonal crystals were washed with fresh DMF. Ethyl ether was added to the vial, and the vial was sonicated briefly to remove crystals from the vial walls. The ether was discarded and the crystals were dried under vacuum and then collected. Yield: 13 mg.

$\mathbf{F_{2D}}$

Compound **1** (20 mg, 8.90 mmol, 1 eq.) was dissolved in 5 mL DMF. Zinc nitrate hexahydrate (13 mg, 43.70 mmol, 4.9 eq.) was dissolved in 5 mL EtOH. A 5 mM stock solution of HCl in EtOH was prepared from a 2 M HCl solution in diethyl ether. 0.4 mL of the 5 mM HCl solution was added to the zinc solution. (We note that a small fraction of $\mathbf{F_{3D}}$ forms under these conditions without HCl, but can be eliminated with the addition of "extra" protons in the form of HCl in the reaction). The two solutions were mixed, filtered and placed in a 20 mL scintillation vial. The vial was sonicated for 5 minutes, placed in an oven, and heated to 65 °C for 24 hours. After cooling to room temperature the supernatant was removed and the cubic crystals were washed with fresh DMF. Ethyl ether was added to the vial, and the vial was sonicated briefly to remove crystals from the vial walls. The ether was discarded and crystals were dried under vacuum then collected. Yield: 8 mg.

3.8.2 Instrument details

NMR

^{1}H NMR spectra were recorded on a Bruker DRX400 (400 MHz) or a Bruker DMX500 (500 MHz) spectrometer. ^{31}P NMR spectra were recorded on a Bruker DMX500 (500 MHz) spectrometer and referenced to phosphoric acid (H_3PO_4). ^{1}H NMR chemical shifts were referenced to residual protons in the NMR solvent.

X-ray diffraction

Crystallographic data for all compounds was collected on an Agilent SuperNova diffractometer using mirror-monochromated Cu K_α radiation. Crystals were mounted on Mitegen polymer loops with the aid of Paratone oil and cooled on the diffractometer using a Cryostream 700 cooler. Data collection, integration, scaling (ABSPACK) and absorption correction (face-indexed Gaussian integration[66] or numeric analytical methods[67]) were performed in CrysAlisPro. Structure solution was performed using ShelXT[69] or SuperFlip.[70] Subsequent refinement was performed by full-matrix leastsquares on F^2 in

ShelXL.[69] Olex2[71] was used for viewing and to prepare CIF files. PLATON[72] was used extensively for SQUEEZE,[73] ADDSYM,[74] and TwinRotMat. ORTEP graphics were prepared in CrystalMaker. Thermal ellipsoids are rendered at the 50 % probability level. Powder X-ray diffraction data were collected using a PANalytical X'Pert^3 Powder diffractometer.

Cyclic voltammetry

Cyclic voltammetry (CV) was performed on a CHI600C potentiostat using a 3-mm diameter glassy carbon working electrode, platinum counter electrode, and platinum pseudo-reference electrode. Measurements were calibrated using the ferrocene/ferrocenium redox couple. A 0.1 M solution of tetrabutylammonium hexafluorophosphate in either DCM or THF was used as the supporting electrolyte. All measurements were done under a dinitrogen atmosphere and at room temperature.

AFM

Atomic force microscopy (AFM) images were acquired in ScanAsyst mode by a Bruker Dimension Icon system under ambient conditions.

SEM

Scanning electron microscopy (SEM) images were taken by a Zeiss SIGMA VP at 0.8 kV. The elemental analysis of framework materials was performed on a HITACHI S-4700 SEM equipped with energy-dispersive X-ray spectrometer (EDX) analyses at 25 kV.

3.9 X-ray crystallographic characterization

3.9.1 Single crystal X-ray diffraction

Crystal data for all compounds is provided in Table 3.1. The refinements of **1-H** and $Co_6Se_8[PEt_2(4\text{-}C_6H_4Br)]_6$ were routine. The structure determinations of $\mathbf{F_{2D}}$ and $\mathbf{F_{3D}}$ were quite challenging due to twinning, pseudosymmetry, and disorder; the refinements are described in detail below.

Crystal structure of $\mathbf{F_{2D}}$

Crystals of $\mathbf{F_{2D}}$ lost their solvent easily when standing in Paratone, so the crystal was continuously cooled by dry ice on the microscope slide and by a Thermos of liquid nitrogen when transferring to the cold stream. The diffraction also appeared to deteriorate at 100 K, and the best data set was collected at 230 K. A full sphere of data were collected to 0.87 Å resolution, although the data set was ultimately truncated at 1.0 Å.

The diffraction pattern clearly showed a threefold non-merohedral twin. The pattern was indexed on a tetragonal unit cell with a = 20.9 Å; c = 14.6 Å. With this indexing, the threefold twin axis was hkl = 201 or uvw = 101. The degree of overlap was modest and therefore merging statistics and systematic absences were easily assessed. This initially suggested a structure in P4/nmm or twinned P4/n.

Structure solution was attempted on the isolated reflections of one component. Solutions were attempted using Superflip and ShelXT. ShelXT failed to provide a usable solution when assuming any of 4/mmm, 4/m, mmm, 2/m, 2/m11, and 112/m symmetry. Superflip

Table 3.1: Crystallographic data for all compounds.

Compound	$\mathbf{F_{2D}}$	$\mathbf{F_{3D}}$	**1-H**	$\mathbf{Co_6Se_8[PEt_2(4\text{-}C_6H_4Br)]_6}$
Formula	$C_{66}H_{84}Co_6O_{14}P_6Se_8Zn_3$	$C_{67}H_{87}Co_6O_{13}P_6Se_8Zn_3$	$C_{66}H_{90}Co_6O_{12}P_6Se_8$	$C_{60}H_{84}Br_6Co_6P_6Se_8$
MW (g/mol)	2468.52	2467.55	2246.45	2455.81
Space group	P2/n	I2/a	P-3	Pbca
$\boldsymbol{a}$ **(Å)**	20.9263(19)	22.6974(10)	11.9463(2)	19.8484(8)
$\boldsymbol{b}$ **(Å)**	14.5590(16)	17.9931(7)	11.9463(2)	19.5785 (9)
$\boldsymbol{c}$ **(Å)**	20.9375(19)	28.9694(14)	16.8522(3)	20.0741(8)
$\boldsymbol{\alpha}$ **(°)**	90	90	90	90
$\boldsymbol{\beta}$ **(°)**	89.983(7)	106.838(5)	90	90
$\boldsymbol{\gamma}$ **(°)**	90	90	120	90
V (Å^3)	6378.9(11)	11323.8(9)	2082.83(8)	7800.8(6)
Z	2	4	1	4
$\boldsymbol{\rho_{calc}}$ **(g· cm^{-3})**	1.285	1.447	1.791	2.091
T (K)	230	140	100	140
$\boldsymbol{\lambda}$ **(Å)**	1.54184	1.54184	1.54184	1.54184
$\boldsymbol{2\theta_{min}}$**,** $\boldsymbol{2\theta_{max}}$	8, 101	8, 91	8, 143	8, 147
Nref	83846	21826	8833	44828
R(int), R($\boldsymbol{\sigma}$**)**	.105, .1353	.0935, .0736	.0325, .0333	.1221, .0809
$\boldsymbol{\mu}$ **(mm^{-1})**	10.183	11.466	14.659	19.071
Size (mm)	.07 × .05 × .05	.06 × .05 × .02	.06 × .05 × .03	0.06 × 0.05 × 0.03
$\mathbf{T_{max}}$**,** $\mathbf{T_{min}}$	.685, .587	.825, .609	.739, .539	.705, .462
Data	17119	4899	2703	7767
Restraints	382	1449	1	0
Parameters	277	387	154	394
$\mathbf{R_1}$**(obs)**	0.0578	0.0859	0.0264	0.0759
$\mathbf{wR_2}$**(all)**	0.1252	0.2682	0.0637	0.2117
S	0.932	1.047	1.063	1.069
Peak, **hole (e$^-$ Å^{-3})**	0.74, -0.64	0.63, -0.47	0.44, -0.42	2.44, -2.13

occasionally (1-2 attempts out of 10) provided solutions in either P4/n or P11n that showed some recognizable features, essentially a layered structure with a Co_6Se_8-sized jumble and a pair of atoms at a typical Zn-Zn four-bladed paddlewheel distance with the paddlewheel axis aligned with the crystallographic fourfold axis.

We proceeded with the solution in P4/n, placing a rigid $Co_6Se_8P_6$ fragment on a -4 site as suggested by the Superflip solution. In this model, the cluster is disordered over four symmetry-related positions and therefore was placed in PART -1.

At this point, we recalled that the merging statistics had indicated 4/mmm was the point group. A model in P4/n therefore should be a perfect merohedral twin. We introduced a twofold rotation around 110 as a twin law. An obstacle here was the fact that ShelXL handles non-merohedral (HKLF 5) or merohedral (TWIN) twinning but not both simultaneously. We prepared a Python script (see below) that takes an input HKLF 4 or 5 file, transforms each reflection by one or more twin laws, and returns an HKLF 5 file that may implement either several independent merohedral twin operators or simultaneous merohedral and non-merohedral twinning.

For a model in P4/n containing a $Co_6Se_8P_6$ cluster on a -4 site and two Zn atoms on a fourfold axis, different twinning models had the following effect: "detwinned" HKLF 4 from CrysAlisPro: R_1 = 50%. HKLF 4 with twofold merohedral twinning: R_1 = 39 %. HKLF 5: R_1 = 35 %. HKLF 5 plus twofold merohedral twinning: R_1 = 29 %.

We looked for a fully ordered model by removing the fourfold axis around which the cluster is disordered in P4/n. This gives a model in polar P11n, interestingly the space group that Superflip suggested in some attempted solutions. The fourfold axis remains as a twin law, but only has to be applied once because refining 2[001] as a twin law in point group ..m is equivalent to refining the Flack parameter. The model in polar P11n, with 11 independent twin volume fractions, refines to R_1 = 16 %.

Finally we noted that Co_6Se_8 clusters typically crystallize on inversion centers and that a four-bladed Zn_2 paddlewheel can also fit on an inversion center. Therefore we transformed the model into P2/n by moving the origin to place the cluster and Zn_2 dimer on inversion centers and deleting inversion-related atoms. The centrosymmetric model also refined to $R_1 = 16$ % and therefore is preferred.

Inspection of difference maps did not give any indication of light atom positions, but it was possible to deduce the positions of 2 out of the 3 independent phosphine $C_6H_4CO_2$ fragments by orienting them toward adjacent Zn_2 nodes. This improved the refinement stability enough to remove the rigid-body constraint on the heavy-atom cluster core and anisotropically refine Co, Se, and P atoms. At this point, a final heavy atom was located between the cluster layers and tentatively identified as Zn. Fourier maps clearly showed the final $C_6H_4CO_2$ group pointing toward this atom.

We proceeded to locate all phosphine C_2H_5 groups by a combination of difference maps and trial and error. Anisotropic ADPs for the heavy atoms and individual isotropic ADPs for C and O were reasonably well behaved. Hydrogen atoms were placed in calculated positions and refined with riding coordinates and ADPs. The disordered solvent was modeled as a diffuse contribution to the overall scattering by the use of SQUEEZE. 5 iterations of the SQUEEZE procedure were required before the final electron count converged.

In the final refinement, all 12 twin orientations were occupied with volume fractions between 5.92(9) % and 13.39(10) %. We note that the determination of a 12-fold twinned structure is extremely unusual. We found only one previous example[110] of a successfully determined structure from a 12-fold twin.

Crystal structure of $\mathbf{F_{3D}}$

The data (cell metric and merging statistics) were consistent with a rhombohedral structure, and the structure was initially solved in R-3c. In R-3c, two Zn atoms lie on a threefold axis and are coordinated symmetrically by three μ^2-carboxylates in a three-bladed paddlewheel arrangement. This moiety collides with its own symmetry equivalent and has a significant positive Fourier feature between the two Zn atoms. This suggested a model in which a trinuclear Zn_3 moiety is disordered by symmetry over a twofold axis in R-3c. However, on closer inspection, the third Zn atom was located a small distance from the threefold axis. This requires that a model in R-3c must be additionally disordered by symmetry around the threefold axis. Therefore, the symmetry was lowered to monoclinic I2/a, a subgroup of R-3c.

In I2/a, the trinuclear Zn_3 moiety is still disordered by symmetry around a twofold axis perpendicular to the Zn-Zn-Zn axis. In addition, in view of the good merging statistics for trigonal symmetry, the threefold axis of the rhombohedral lattice was preserved as a threefold pseudomerohedral twin law.

The geometry of the $Co_6Se_8P_6$ core of the cluster required some restraints to behave in the refinement. All chemically equivalent 1,2- and 1,3- distances were made equivalent with "floating" DFIX restraints. Anisotropic ADPs were refined but required RIGU and SIMU restraints.

The three μ^2-carboxylates of the three-bladed paddlewheel were retained in the monoclinic model; their positions were now independent and were restrained with DFIX or SADI instructions for intramolecular geometry and with soft DFIX restraints for all Zn-O distances. The three carboxylates associated with the third Zn atom were located with difficulty. The displacement of atom Zn3 away from the pseudo-threefold axis creates two shorter P...Zn distances of about 8.2 Åand one longer P…Zn distance of about 8.8 Å. By trial and error we found that $C_6H_4CO_2$ fragments bound η^2 (chelating) to Zn3 fit the shorter P…Zn distances and another C6H4CO2 bound μ^2 (bridging) to Zn2 and Zn3 fit the longer P…Zn distance. At this stage, all six carboxylates bound to the Zn_3 node had been located, but restraints on all Zn-O distances were required and several anti-bumping restraints were employed to prevent unrealistically small O-Zn-O angles. Additionally, the light-atom skeletons of the $C_6H_4CO_2$ ligands were stabilized with rigid-body constraints for the phenyl rings and FLAT and DFIX/SADI restraints.

Phosphine ethyl groups were located in difference maps and subsequently refined with all 1,2- and 1,3- distances restrained. Several terminal methyl positions were unstable and ultimately required a combination of anti-bumping restraints and a weak DAMP instruction for the least-squares refinement.

All C and O atoms were refined with a single group isotropic ADP in view of the weak data, twinning, and pseudosymmetry. Hydrogen atoms were placed in calculated positions and refined with riding coordinates and ADPs.

Zn3 displays a large and unusually shaped displacement ellipsoid that is likely a sign of unresolved disorder. We were not able to construct an explicit disorder model and therefore have left the unusual ellipsoid as is.

Several voids in the structure were filled with diffuse electron density that could not be modeled explicitly. This was treated by SQUEEZE to model the disordered solvent as a diffuse contribution to the overall scattering without specific atomic positions.

3.9.2 Powder X-ray diffraction

The samples were dispersed on a sample holder without grinding and therefore the intensities are strongly affected by preferred orientation. The peak positions are in good agreement with the simulated powder patterns generated from the SCXRD data and confirm the identity and phase purity of the samples (Figure 3.14). We note that the simulated patterns were generated from SCXRD run at 100 K, while the PXRD patterns were collected at room temperature, and that some of the solvates are removed from the crystal lattice under ambient conditions.

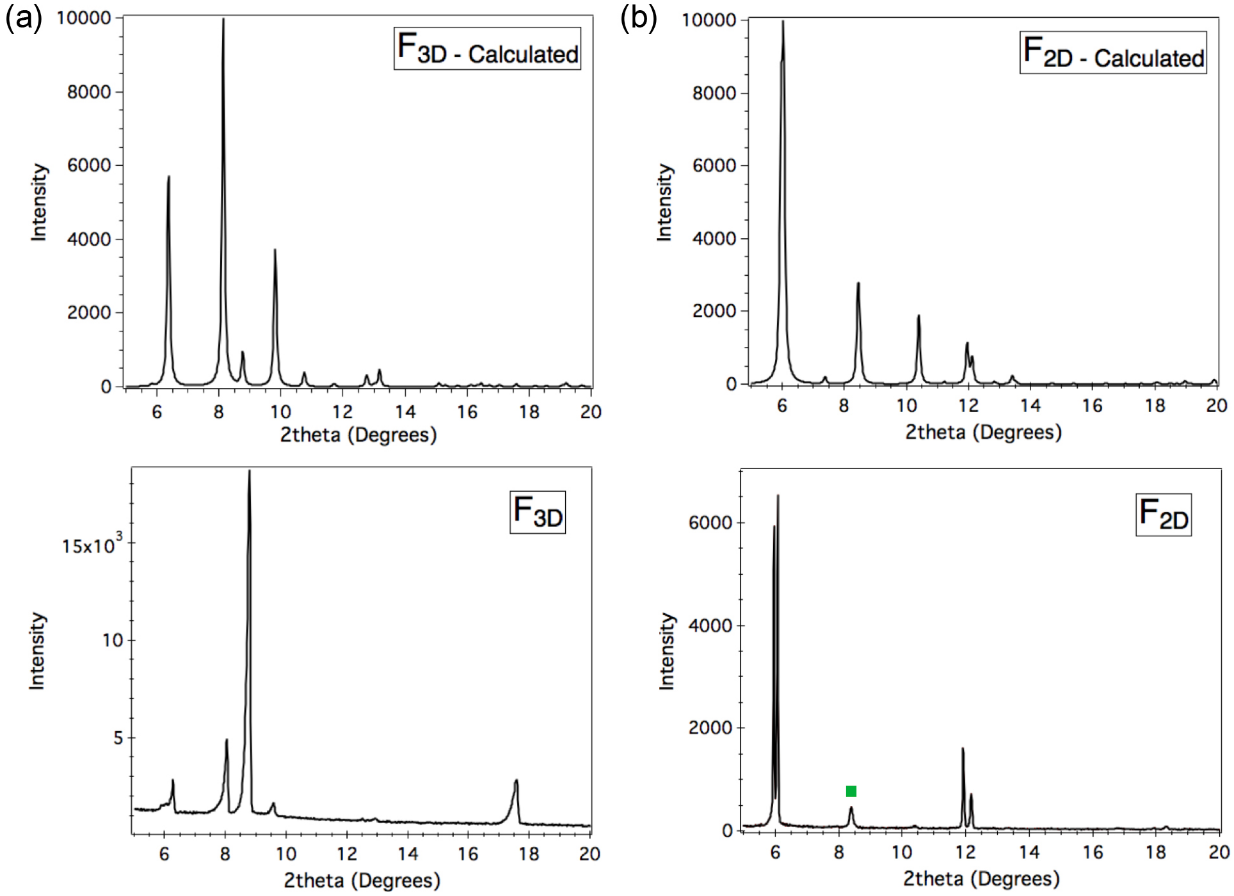

Figure 3.14: PXRD of (a) $\mathbf{F_{3D}}$ hexagonal plates and (b) $\mathbf{F_{2D}}$ cubes calculated from single crystal data (top) and experimental (bottom).

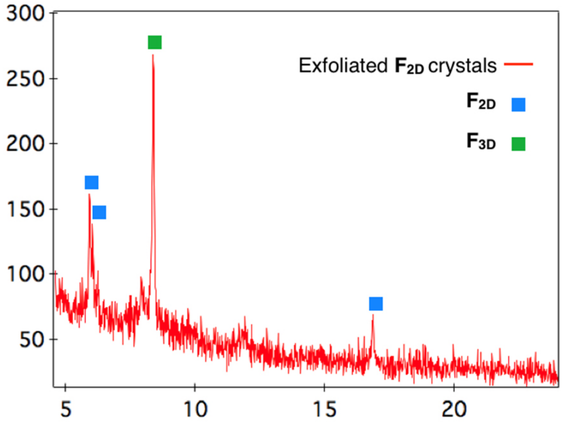

Figure 3.15: Powder XRD spectrum showing the exfoliation of $\mathbf{F_{2D}}$ cubes upon immersion in 40 mM benzoic solution in DMF. The initial spectrum of intact $\mathbf{F_{2D}}$ crystals is shown in Figure 3.14b. The blue squares highlight the peaks corresponding to $\mathbf{F_{2D}}$, whereas the green square highlights traces of $\mathbf{F_{3D}}$ present in the as-synthesized sample (PXRD spectrum of $\mathbf{F_{3D}}$ is shown in Figure 3.14a). A few drops of 40 mM benzoic solution in DMF were added to the crystals directly onto the powder plate. The colorless solution turned a light brown-red color and the cubes become less visible by eye. After 10 minutes, the liquid was removed by syringe and the resulting diffraction was obtained (red trace). Peaks corresponding to $\mathbf{F_{2D}}$ have become less intense relative to $\mathbf{F_{3D}}$ peaks. Since $\mathbf{F_{3D}}$ is a 3D network, we do not expect to be able to exfoliate this material and the crystals should not fall apart under these conditions, as is observed.

Chapter 4

Fabrication of hundreds of field-effect transistors on a single carbon nanotube for basic studies and molecular devices[1]

4.1 Introduction

Due to their unique structure, extraordinary electrical and mechanical properties, and unusual chemical properties, carbon nanotubes (CNTs)[111] are of great interest for many applications. In particular, carbon nanotube field-effect transistors (CNT FETs) have been extensively investigated[112–117] since they were first fabricated in 1998.[118, 119] Because

---

[1] Part of this chapter is reproduced from the work published in J. Vac. Sci. Technol. B **31**, 06FI01 (2013). Copyright 2013, American Vacuum Society. Xian Zhang and I performed device fabrication and electrical measurements with assistance from Daniel Chenet and Bumjung Kim. Conductance studies for DNA oligomers were done in collaboration with Jacqueline Barton group.

of their excellent properties such as high conductance, high mobility, and chemical inertness, continuous progress has been carried out on applications of CNT FETs, which includes integrated circuits,[120, 121] nanoelectromechanical systems,[122] and biosensors.[123–128] In one specifically demanding application, individual CNT FETs are lithographically "cut" and rejoined with single molecules in the gap, to yield circuits that can be used to study the basic electrical transport properties of single molecules, and can form the basis of multiple types of sensors.[129, 130] Because of the extreme precision required, such devices have a yield of only a few percent, which severely limits the speed of progress in implementing CNT-molecule devices. Thus, it is desirable to optimize the CNT FETs platform with high yield and precise characterization for this application.

The current reported methodologies in making and characterizing CNT FETs can be categorized into three fundamental types. The first is the FETs on random networks of CNTs,[131, 132] which is flexible in fabrication process and can achieve scaled-up design, but the random distribution of CNTs brings poor uniformity for the FETs properties and makes it difficult to characterize conductance properties of single molecules. The second method is the massive fabrication of CNT FETs with CNTs grown from catalyst islands located on each device.[133] The disadvantages of this method are the diversity of CNT structures and uncertainty of the number of CNTs connecting each source-drain channel, posing a challenge to collect uniform and meaningful information from single molecules. The third method is producing FETs out of one single long CNT,[134, 135] which shows potential for single molecules sensing platform. However, the uniform characterization of many devices fabricated by such platform has not been reported, to date.

In this work, for the first time, we characterize hundreds of FETs around one single long single-walled carbon nanotubes (SWCNT) on the 1 × 1 cm^2 silicon substrate. After outlining the experimental details of the technique, we discuss the performance of transfer curves of all devices fabricated out of one CNT. The maximum number of conducting devices we fabricated out of 33 chips was 775. The measurement result from one substrate shows uniform and stable characteristics that significantly exceed previous reports. This technique allows the goals described above to be addressed to test reproducibility of high-yield devices such as molecular conduction.

4.2 Design and fabrication of hundreds of CNT FETs

The substrate was designed to pattern electrode arrays on top of a single CNT grown by chemical vapor deposition (CVD) on an oxidized silicon wafer by flow-aligned growth. Figure 4.1a shows a schematic design of the electrode arrays. The process described below is used to fabricate this array of electrodes. Pairs of adjacent electrodes form source and drain contacts and the conducting wafer forms a global back gate, with 300 nm SiO_2 as the gate dielectric. Figure 4.1b shows the atomic force microscopy (AFM) scan of a single CNT used for fabrication, with a diameter of 1.65 nm.

The photolithography mask used to pattern the electrodes with this design is shown in Figure 4.1c. This design targets one single long carbon nanotube in the center of the chip with electrode pads fanning out across a ∼5 mm square area for individual probing of each electrode pair. Each CNT section is 4 μm in length. This compact structure design contains around 900 devices on each chip, with 27 rows and 36 electrode pads on each row. For every four rows, there are two smaller squares replacing electrode pads, serving as the alignment

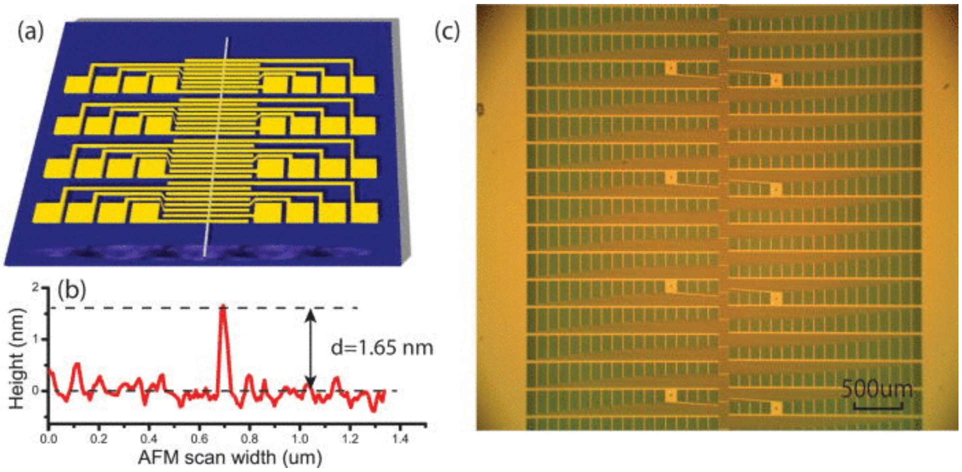

Figure 4.1: (a) Drawing for CNT FETs platform design with arrays of electrodes around one single carbon nanotube in the center. (b) AFM height profile of a single CNT. (c) Actual photolithography mask used to pattern the electrodes with 27 rows and 36 columns.

marks for electron beam lithography in the following treatments.

The CNT FETs fabrication process generally contains six steps as shown in Figure 4.2. These devices can also serve as a sensing platform and are later used to test conductance of DNA.

First, highly doped 4 in. thermally oxidized silicon wafer was diced into 1 × 1 cm^2 substrates (Figure 4.2a). Flow-aligned SWCNTs growing from one edge of the substrate were prepared by conventional chemical vapor deposition method directly on the silicon substrate. The Müller catalyst (Fe-Mo mixed nanocluster)[136, 137] was swabbed on one edge of the substrate. The CVD growth condition was at 890 °C for 40 min with 10 sccm H_2 and 40 sccm Ar gas mixture flowing through ethanol and across the substrate. A high degree of CNTs orientation along the direction of gas flow could be obtained (Figure 4.2b).

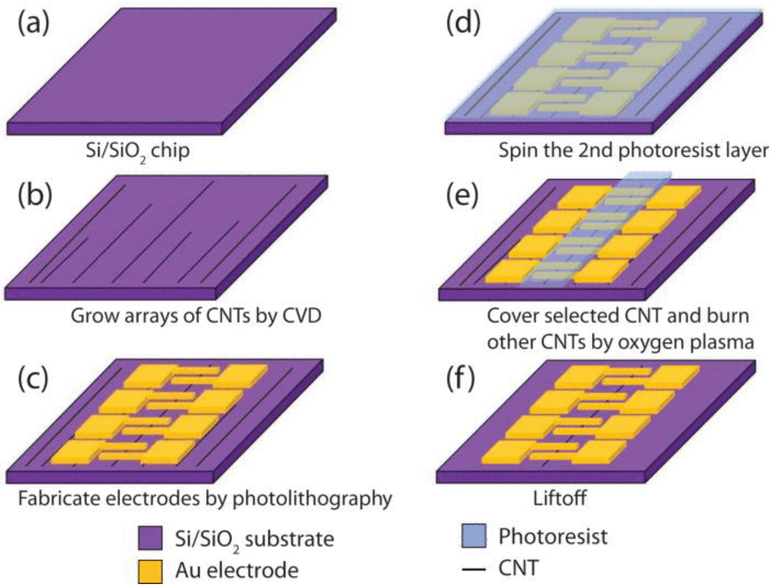

Figure 4.2: Schematic illustration of the fabrication of the arrays of FETs around one single long CNT.

Then one single long CNT (usually reaching 1 cm across the entire substrate) was identified and positioned by scanning electron microscope (SEM). The CNT location was done by recording "five points" (two points on the carbon nanotube, two points on the substrate edge, and one point on a scratch made on the substrate edge center as a position reference) of the selected CNT in order to calculate the position and angular direction relative to the substrate. Assuming a completely straight carbon nanotube, the two points on the carbon nanotube and two points on the substrate edge were used to calculate an angle between the carbon nanotube and the substrate edge. Then, the two points on the carbon nanotube and one point on the scratch were used to calculate the distance from the scratch to the carbon nanotube. This recording and calculation of carbon nanotube position are

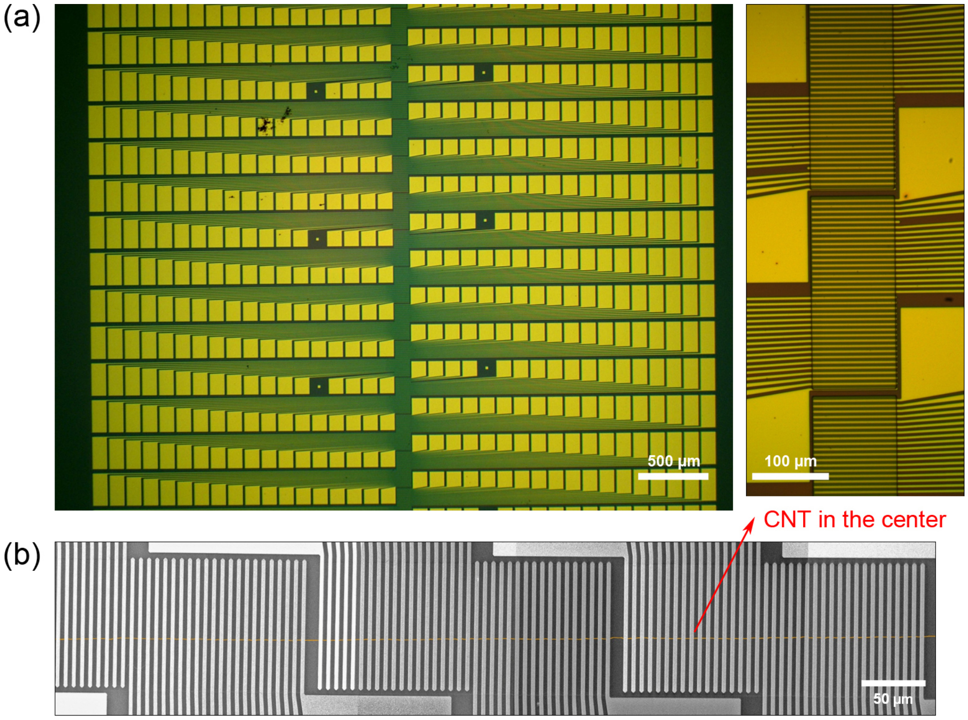

Figure 4.3: (a) Optical image of the carbon nanotube device arrays on one chip, and the zoom-in optical image of blocks of photoresists protecting the center carbon nanotube area in the burning extra tubes process. (b) The SEM image of electrodes patterned on one carbon nanotube after fabrication.

due to impossibility of identifying the carbon nanotubes by optical microscope when doing photolithography for electrodes patterning.

The first photolithography step was performed to deposit electrodes on the selected long CNT (Figure 4.2c). LOR3A (1 μm) and S1813 (300 nm) were first coated on the SiO_2/Si substrate. The lift-off resist layer provides an undercut profile, facilitating a clean lift-off process after electrode deposition. The electrode pattern was fabricated using a customized photomask (Figure 4.1c) and UV light exposure using Süss MA6 mask aligner. The photomask was placed on the substrate where all the center overlapped electrodes covered only the aimed CNT. After development in MF-CD-26 developer for 70 s, the electrodes were formed on the chip by depositing Cr(1 nm)/Pd(10 nm)/Au(50 nm) by electron beam evaporation. Cr served as an adhesive layer, Pd as a good CNT contacting layer,[138, 139] and Au as a protective layer to prevent oxidation at the Pd. The lift-off was done using Remover PG with bath at 70 °C for 4 h in order to have a complete removal of unwanted leftover resists and metals.

The CVD growth process produces many carbon nanotubes around the CNT of interest. In order to remove them, a second photolithography step (Figures 4.2d and 4.2e) was performed. This step is essential as it prevents interference from extra CNT connections. The substrate was coated with polymethyl methacrylate (PMMA) (50 nm) and S1813 (300 nm), exposed under UV light, and developed in MF-CD-26 developer with the same recipe as the first photolithography step. PMMA was used as a protective layer to avoid contamination from S1813 to the CNT devices. Then, the S1813 photoresist was patterned into 27 blocks covering the center overlapped electrodes area (Figure 4.3a), so in the following step the only CNT remaining in the protected area was also divided up to 27 subsections. This CNT dividing method is to prevent possible gate leakage from spreading to all the electrodes and devices. For such a large electrode array, it is highly possible that one electrode pad might not be well insulated by the SiO_2 layer on the Si substrate. The exposed CNTs (and the CNT sections between the photoresist blocks) were removed by "burning" in an oxygen plasma (RIE Technics Series 800), with 250 mTorr gas pressure and 50 W power for 80 s. Remover PG with bath at 70 °C for 4 h was used to remove the photoresists. Figure 4.3b shows joint

SEM images of a single carbon nanotube with arrays of electrodes fabricated upon it. The resulted CNT channel is around 3 μm in length. At this point the completed devices were tested (Section 4.6.8).

4.3 Electrical characteristics of CNT FETs

This fabrication method produces a chip with up to 775 transistor devices, whose density is limited by the "real estate" for contact pads (Figure 4.3). With a design of around 900 devices, the fabrication result achieves a yield of 87 %, which is defined as the percentage of working devices number (775) out of the maximum number of devices we measure (890). The long CNT (as long as 1 cm) we can grow goes through the whole electrode region, providing this large number of devices. An average yield of 47 % was calculated out of 33 samples. The limitation for achieving the full 900 devices is due to the manual operation of mask aligner to locate the mask on a target CNT. Nonetheless, our platform allows us to have an average number of working devices is over 400 on one chip from an average fabrication yield of 47 %. This large number of devices ensures high device output and allows us to study the stability and uniformity of devices' properties.

Figures 4.4 and 4.5 show the conductance behavior of metallic and semiconducting CNT devices, respectively, both of which are fabricated using the same method presented here. Figure 4.4a shows the typically recorded transfer characteristics of 82 randomly selected metallic CNT devices on one metallic chip, with a channel length of 3 μm. The inset of Figure 4.4a presents an example of hysteresis behavior. The conductance curves show ambipolar behavior with a dip around 0 V gate voltage, which is typical behavior of metallic

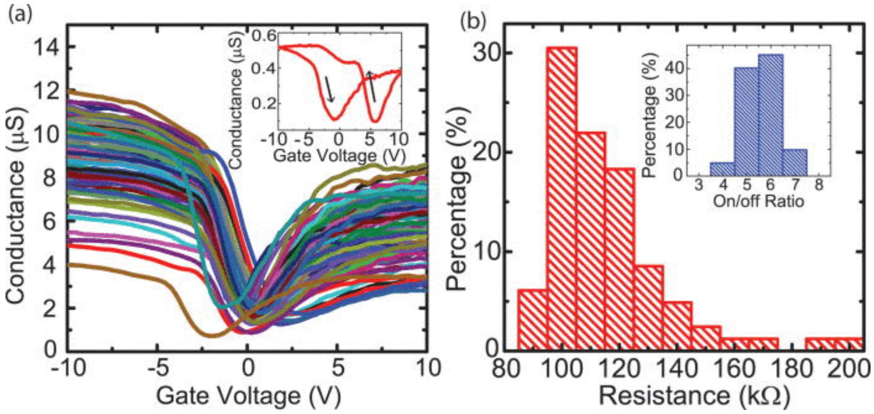

Figure 4.4: (a) Transfer characteristics of 82 selected metallic CNT devices exhibiting a small band gap. Inset: an example of the hysteresis behavior. (b) Distribution of metallic CNTs' resistance with a 3 μm channel length, and distribution of the devices' on/off ratio.

single-walled nanotubes with a small band gap.[140] Most of the transfer curves lie in the same range of conductance and share similar trend. We analyze and plot the distribution of resistance and on/off ratio in Figure 4.4b. It shows over 92 % of the devices have resistance below 150 kΩ, and all the devices have on/off ratio between 4 and 7, which means this chip has a high yield of low-resistance devices and good uniformity.

Figure 4.5a presents transfer characteristics of 82 typical semiconducting CNT FETs randomly selected from one semiconducting chip, with an inset of an example of hysteresis behavior. They share the same channel length of 3 μm. Figure 4.5b plots the distribution of on-state resistance and on/off ratio, which shows over 97 % of the devices have resistance below 1200 kΩ, and all the on/off ratio are above 1000. The plots of threshold voltages of these devices (Figure 4.5c) reveal the uniformity of the on and off conductance behavior, with most of the values lie within −3 and −6 V. Figure 4.5d is the distribution of field-effect

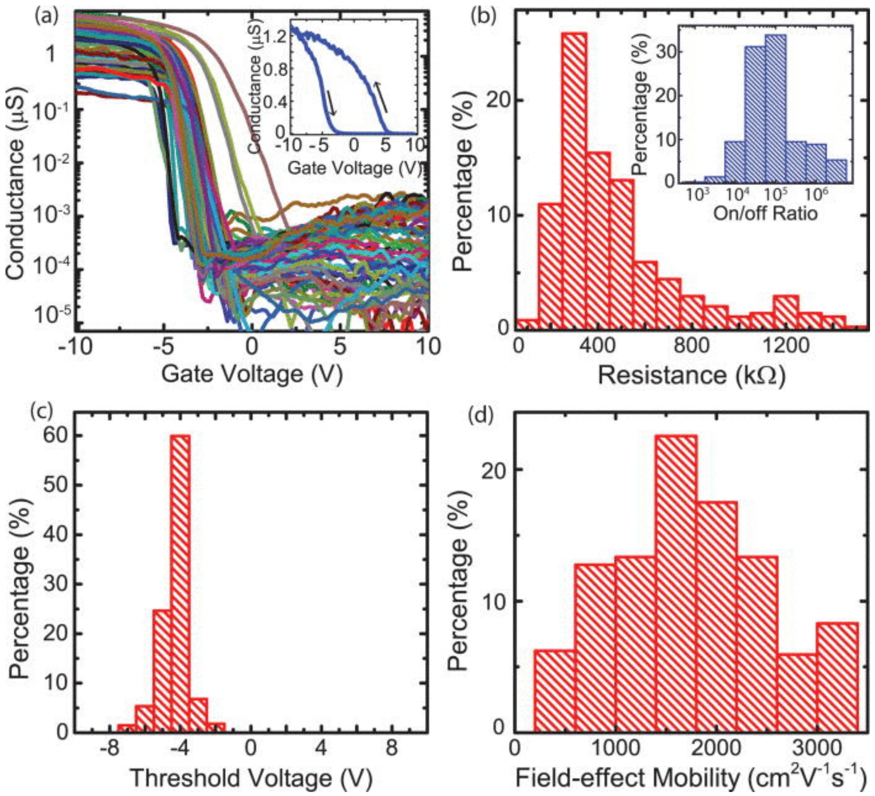

Figure 4.5: (a) Transfer characteristics of 82 selected semiconducting CNT devices. Inset: an example of the hysteresis behavior. (b) Distribution of the semiconducting CNTs' on-state resistance with a 3 μm channel length, and distribution of the devices' on/off ratio. (c) Distribution of threshold voltage. (d) Distribution of the calculated field-effect mobility.

mobility, with an average value around 1600 cm^2/Vs. The value of field-effect mobility μ_{FE} of each device is calculated according to the following formula:[141]

$$\mu_{FE} = \frac{L^2}{C_G}\frac{dG_S}{dV_{OV}} \tag{4.1}$$

The gate capacitance (C_G) is defined as

$$C_G = L\left[{C_Q}^{-1} + \frac{ln(2t_{ox}/r)}{2\pi\varepsilon_0\varepsilon_r}\right]^{-1}, \tag{4.2}$$

where L is 3 μm, G_S is the device conductance, and V_{OV} is the gate overdrive voltage defined as gate voltage in excess of the threshold voltage. C_Q is the quantum capacitance (0.4 nF/m), $t_{ox} = 300$ nm is the SiO_2 dielectric thickness, r = 0.83 nm is the radius of CNTs, ε_0 is vacuum permittivity, and ε_r is calculated as $\varepsilon_r = (\varepsilon_{air} + \varepsilon_{SiO_2})/2 = (1 + 3.9)/2 = 2.45$.

4.4 Conductance studies for DNA-bridged CNT FETs

The unique electronic properties of DNA have captured the interest of researchers for over half a century. DNA-mediated charge transport (DNA CT) has been investigated from multiple angles, with diverse experimental platforms, to reveal that this chemistry proceeds exclusively through the π-stacked core of aromatic nucleobases within the linear DNA molecule.[142] For systems with robust electronic coupling to the π-stack, DNA CT can proceed over long molecular distances.[143] However, only undamaged DNA with a continuous path of well-stacked bases forms this efficient electrical conduit; even slight perturbations in base pair stacking, such as mismatches[144, 145] or protein binding[146, 147], dramatically attenuate DNA CT. Further underscoring the role of the π-stack in facilitating DNA CT, DNA-mediated conductivities that are measured in an aqueous, undamaging environment, match the expected conductivity perpendicular through a stack of graphite planes of the same length.[130] These electronic characteristics, combined with the ease with which DNA may be precisely synthesized and functionalized, have led to the consideration of DNA as a versatile molecular wire candidate for nanoelectronic and biosensing applications. Additionally, growing evidence suggests that this capacity for efficient and sensitive long-range charge transport may be a key mechanism for protein signaling and coordination in living organisms.[148, 149]

Essential to the consideration of DNA CT in these contexts is an understanding of how the efficiency of DNA CT is affected by the CT distance. Although many other aspects of this chemistry are now well demonstrated and understood, the direct measurement and comparison of DNA CT over regimes of increasing distance has been elusive. Solution-based photoexcitation studies first suggested that DNA CT may proceed efficiently over long distances.[150, 151] Though the studies showed minimal impact from the CT distance, the resolution limits of the platforms used to make these measurements prevented the direct calculation of β for DNA, a parameter that describes the distance dependence of the CT rate. More significantly, as these approaches measure excited-state DNA CT, results cannot be confidently used to infer the same shallow distance dependence in systems where ground-state DNA CT occurs, such as nanoelectronic devices and living organisms.

CNT-based devices, in which a single molecule spans an oxidatively cut gap in the CNT, provide a versatile, ground-state platform with well defined electrical contacts that have previously been used to measure the electrical properties of a variety of small molecule bridges.[129, 130, 147, 152–155] High electrical sensitivity of CNT enables low-voltage device operation and more importantly, these measurements can be carried out in aqueous solution as well as in ambient condition, providing a natural and undamaging environment for biomolecules.

Previously, this platform was shown to be highly effective for single molecule measurements of DNA CT through DNA duplexes that covalently bridge the CNT gap.[130, 147] In these studies, the path of CT through the device was confirmed to be DNA-mediated because of the dramatic loss of current flow upon introduction of single base mismatches in the bridging duplex.[130] Additionally, the single DNA duplex that is wired into the device was shown to be an active substrate for DNA-binding proteins including restriction endonucleases[130] and methyltransferases,[147] indicating that it is maintained in a biologically recognizable and accessible conformation.

Here, we utilize this ground-state, single molecule, CNT-DNA platform to measure the electrical resistance of DNA-mediated current flow over increasing DNA bridge lengths (up to 27 nm). As single molecule measurements generally provide more direct information about the fundamental electronic properties of a molecule than do ensemble measurements,[153] CNT-DNA devices represent a more sensitive platform than the ensemble platforms used previously. Additionally, by employing the state-of-the-art device fabrication technique, a number of data for statistics were obtained with reliable stability and uniformity.

4.4.1 Nanogaps in carbon nanotubes

For DNA length dependence study, we hope to collect as many working devices as possible and we used CVD-grown CNT devices (Section 4.2). Figure 4.6 is the schematics for one CNT device before cutting, after cutting, and after DNA molecule reconnection inside the CNT gap. For this application, the metallic CNT devices are preferred, for their continuous

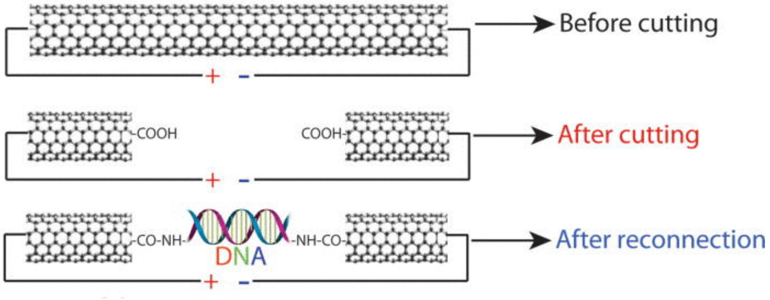

Figure 4.6: Diagram showing one CNT device before cutting, after cutting, and after DNA reconnection.

"on" conducting behavior over the whole gate voltage range.

To form a CNT nanogap, a narrow PMMA window was first opened using ultra-high resolution (∼10 nm) e-beam lithography. The exposed portion of nanotubes was then cut with an oxidative plasma etch, leaving carboxylic acids on the two termini of the cut nanotubes. Importantly, a length of the PMMA window was varied by the target DNA molecule. AFM images shown in figure 4.7 are good examples of CNT nanogaps that are precisely cut to fit the given DNA molecules.

Electrical measurements need to be taken after cutting to confirm whether CNT devices are still alive or are completely cut. It is important to note that we do measure voltages of each electrode pad when performing cut measurement (Figure 4.8). Unlike initial and final measurements, candidates should show no conductance over the channel. Voltage measurements would prevent us from misreading results that arise from bad contacts between probes and electrodes. Inset graph in figure 4.8b shows the representative plot of source and drain voltages as a function of the gate voltage. The measured source voltage is 50 mV (± 2 μV) which is a bias voltage we applied, and the drain voltage is 71 μV (± 3 μV).

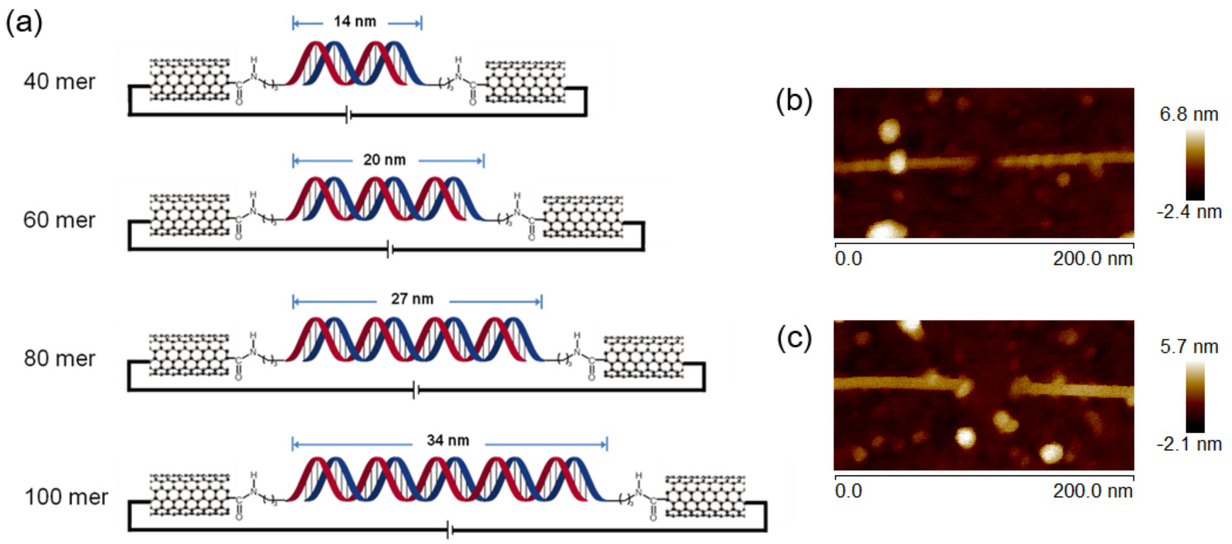

Figure 4.7: (a) Diagram illustraing DNA-bridged CNT FETs with different DNA lengths. (b,c) AFM images of CNT nanogaps after oxidative cutting. Measured nanogaps are (b) ∼14 nm and (c) ∼27 nm which are good for reconnection with 40-mer and 80-mer strands, respectively.

We also note that individual devices are isolated by opening 200-nm CNT gap in adjacent devices, and these large-gap devices are skipped when electrically measured. By doing this, we can avoid a widening of the gap cut while measuring the conductance of a neighboring device. At this second step, therefore, the total number of devices is reduced to 472 from 890.

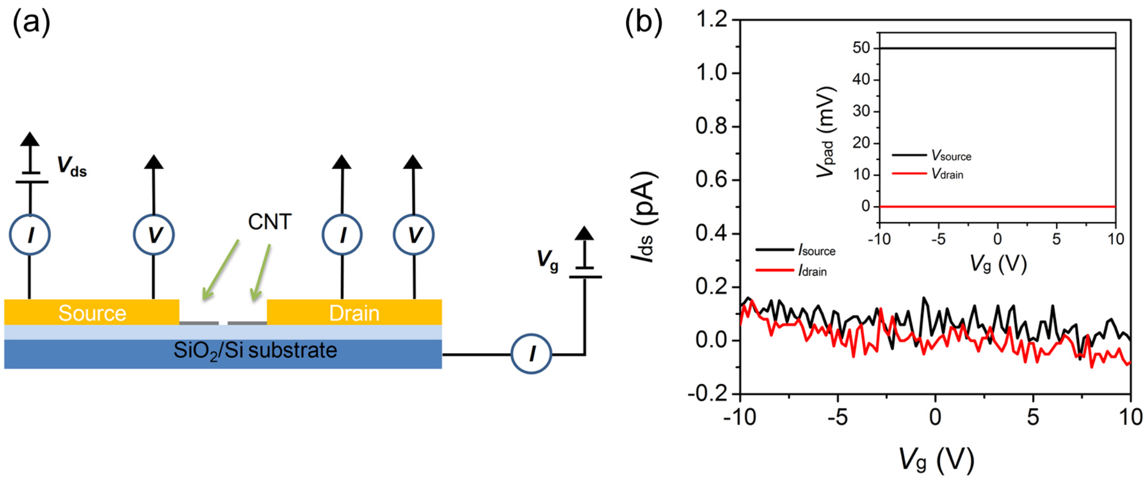

Figure 4.8: (a) Schematic of electrical measurement of CNT FETs after nanogap opening. (b) $I_{ds} - V_g$ characteristic of a typical CNT device after CNT cutting. Inset shows the voltage measurement of source and drain pads during gate sweep.

4.4.2 Length dependent conductance of DNA oligomers

For DNA length dependence measurements, CNT-DNA devices were reacted with bridging DNA segments of varying length including 40-mer (14 nm), 60-mer (20 nm), 80-mer (27 nm), and 100-mer (34 nm), all with C3 amine linkers (Figure 4.7a). Carboxyl groups created by oxygen plasma on the two ends of the CNT gap were used to connect the DNA molecule through amide linkages. First, we created DNA junction between nanotube electrodes with a 40-mer DNA (Figure 4.9). The plot of the transfer characteristics of three-step conductance measurements is shown in Figure 4.9a. The fabricated device initially exhibits high current ($> 10^{-6}$ A), then it shows current at the noise level ($\sim$10 pA) after oxidative plasma etching. The final electrical current comes from a molecular bridge and the minimum resistance

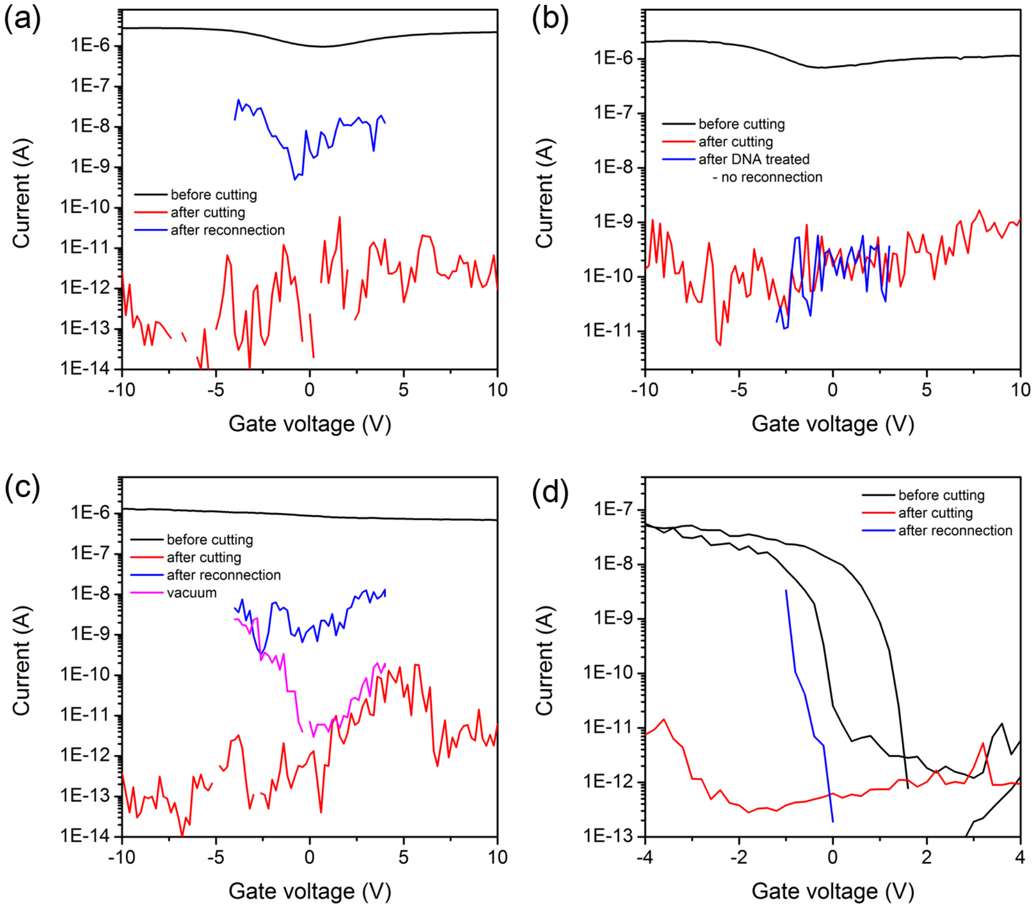

Figure 4.9: Representative device characteristics of CNT FETs (a) reconnected with a 40-mer DNA and (b) without a molecule bridge. (c) The device characteristic change for a DNA-bridged CNT FET after vacuum treated. (d) $I_{ds} - V_g$ characteristic of a semiconducting CNT device bridged with a 40-mer.

is calculated to 1.1 MΩ. Figure 4.9b demonstrates typical device characteristics of FET that fails to form a molecular junction even after the target DNAs are treated. The final conducting signal remains as the same level of the second measurement. Approximately, we obtained one reconnected device among ∼500 of fabricated devices, resulting in ∼0.2 % of the overall yield. This low yield is a combination of low cutting yield due to the narrow nanogap window (∼14 nm) and small possibilities of reconnection that requires both amine ends of strands reacting with carboxylic acid groups of nanotube electrodes.

DNA molecule that is connected in solid-state CNT FETs is fragile under vacuum treatment. Figure 4.9c demonstrates the loss of conductance of a reconnected device. We speculate that double strands of DNA get dehybridized after stored in vacuum; thus charge cannot be transported through π-stacked bases. Figure 4.9d is an example of reconnection result with semiconducting CNTs. Interestingly, the semiconducting characteristics are recovered with a lower conductance after a DNA junction is formed.[2]

Electrical measurement of CNT devices reconnected with an 80-mer is shown in Figure 4.10a. The graph contains curves of as-prepared, nanogap-opened and DNA-reconnected devices. The blue curve in Figure 4.10a displays retrieval of current from nanogap-opened step (red curve), indicating that DNA successfully linked the nanogap. The final reconnection current in Figure 4.10b is almost two orders of magnitude higher than that in Figure 4.10a. We characterized the nanogap size of another device written in the exact same condition with the device shown in Figure 4.10b and found that the nanogap size is too small ($<$ 10 nm) to accommodate an 80-mer in the gap. Presumably, the one end of DNA is chemically

---

[2] The gate sweep voltage of the initial electrical measurement was 4 to -4 V for semiconducting CNT FETs due to the hysteresis. The gate sweep voltage of the reconnection measurement was 0 to -1 V for this result.

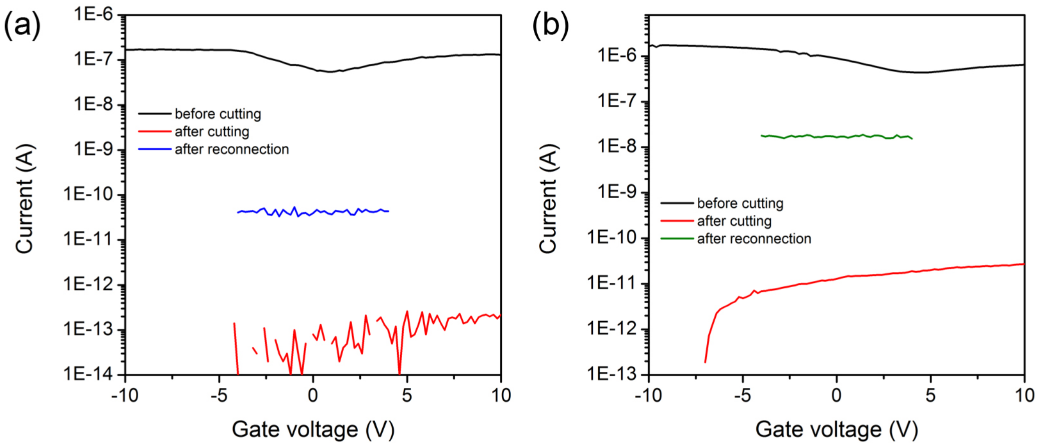

Figure 4.10: (a) Device characteristics of CNT FETs reconnected with a 80-mer. (b) Device characteristics of the device that presumably has one end covalently bonded and the other end physically adsorbed.

bonded to the nanotube, while the other end of DNA is physically adsorbed on the nanotube. This is attributed to the drying direction which is along the single CNT in the center of the pattern.[156] To avoid this physical adsorption, the chip is dried in a perpendicular of the direction of the nanotube.

Figure 4.11a shows the resistance of devices connected with various lengths of DNA. These values were converted from the highest conductance measured over a range of gate voltages with the source-drain voltage of 50 mV. The plot shows a serial exponential increase in resistance as the length of DNA increases. From this plot, the distance dependence parameter β was extrapolated by fitting the plot with the exponential shown in the equation:

$$R = R_0 e^{\beta L} \tag{4.3}$$

where R is the device resistance, R_0 is contact resistance, and L is the DNA bridge length.

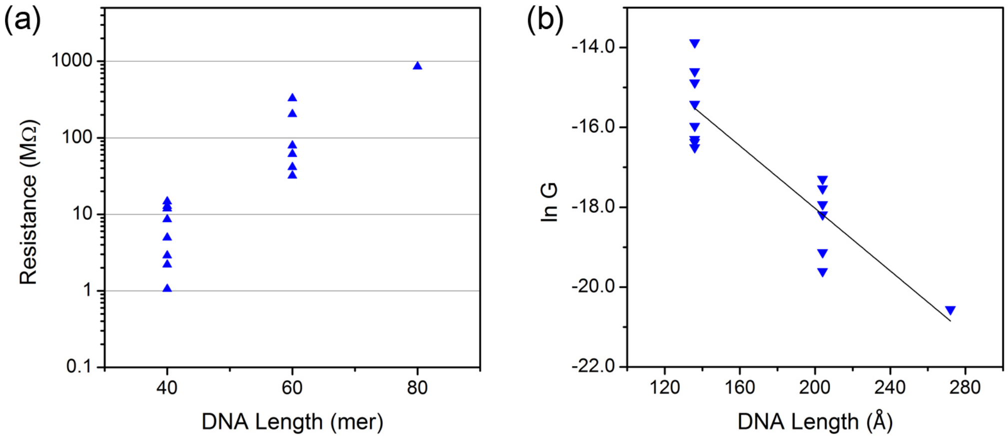

Figure 4.11: (a) Resistance of DNA spanning a carbon nanotube gap as a function of DNA length and (b) corresponding semi-log plot of conductance of DNA-bridged CNT FETs. Data shown are for DNA attached to the CNT device by a C3 linker.

The trend-line of best fit for these data gives a β value of 0.04 ± 0.01 Å^{-1} (shown in Figure 4.11b).[3] An estimated β value of 0.04 Å^{-1} from these measurements is on the order of estimates from previous excited-state measurements[150, 151] and ground-state electrochemical measurements.[143] Furthermore, this value lies within the range of β of more conventional molecular wires (0.001-0.2 Å^{-1}) and among the longest molecular wires reported to date.[143, 157–161] Specifically, the value is comparable with the value of oligo(p-phenylene ethynylene)s (OPE) (0.030 Å^{-1}).[161] Small β value denotes little variation in resistance with length, which is an important factor for a good molecular wire. We attribute this to undisturbed, dry-state atmosphere of measurement condition and direct assembly of DNA into an electrical device.

---

[3] We note that the calculated β value without one result from 80-mer is still 0.04 ± 0.01 Å^{-1}.

In addition, the extracted contact resistance R_0 from the plot in Figure 4.11b is 27 kΩ. It is in the same magnitude of the initial resistances of metallic CNTs. Surprisingly, this value is comparable to the contact resistance of a direct, covalent Au-C bonded single-molecule junctions.[162] Although there is a trend toward increased resistance with increased DNA length, broad distribution of resistance values for each DNA molecule makes it difficult to estimate the contact resistance, resulting in a high standard deviation. To understand more thoroughly, we need more reconnection results from an 80-mer DNA and new data from a 100-mer DNA. For a 100-mer, it is possible that the experiments would be restricted by the resolution of measuring electrical signals because the final current may lie at the noise level.

4.5 Conclusion

We have demonstrated a novel fabrication process of hundreds of CNT FETs on one single long carbon nanotube for basic studies and molecular sensing. This approach is unique for two applications: (1) testing reproducibility, as it ensures many devices fabricated out of the same CNT for statistics; (2) high-yield devices for status at molecular conduction. The fabrication process is based on flow-aligned CVD growth of long SWCNTs and photolithography patterning of electrodes. This high-throughput CNT FETs platform with uniformity is essential for DNA sensing. This mass-fabrication process demonstrated here can be potentially useful to connect DNA with different lengths into the CNT gaps and test the conductance to obtain a conductance trend versus molecular lengths. We also believe this fabrication technology with high throughput and uniformity can help to sense and examine the conductance of a wide range of other nanoscaled molecules.[163]

Using the single molecule CNT-DNA platform, the impact of CT distance on the efficiency of DNA CT was investigated by preparing devices with DNA bridges of varying length and measuring current flow through these devices. We were able to analyze CNT-DNA-CNT devices quantitatively as well as qualitatively using our CNT device fabrication method. For data collected at three different bridge lengths (40-mer, 60-mer, and 80-mer) a β -value of 0.04 ± 0.01 Å^{-1} was derived. This shallow distance dependence measurement agrees strongly with the conservative estimate of β for DNA CT from ensemble electrochemical measurements ($\beta = 0.05$ Å^{-1}).[143] Unlike these previous ensemble measurements where β could not be measured directly, these data suggest that CNT-DNA devices may be used to directly measure how DNA CT varies with increasing CT distance. Reconnection of DNA in the CNT nanogap was clarified by the change in $I_{ds} - V_g$ curves. The characterizations of the impact of distance on DNA CT confirm the wire-like electronic nature of DNA and may be used to inform the application and study of DNA CT in diverse ground-state systems.

4.6 Experimental section

4.6.1 CVD CNT growth

We first prepare diced SiO_2/Si chips by cleaving them from a 4 in.wafer and clean them in piranha solution (3:1 H_2SO_4:H_2O_2). Substrates are rinsed with deionized (DI) water and blown dry with N_2. The Müller catalyst solution (in ethanol) is spread at one edge of the quartz substrate with a cotton swab and the sample is placed in a 1-inch quartz tube for oxidation for 80 min at 500 °C. After purging with Ar, a mixture of 120 sccm Ar and 30

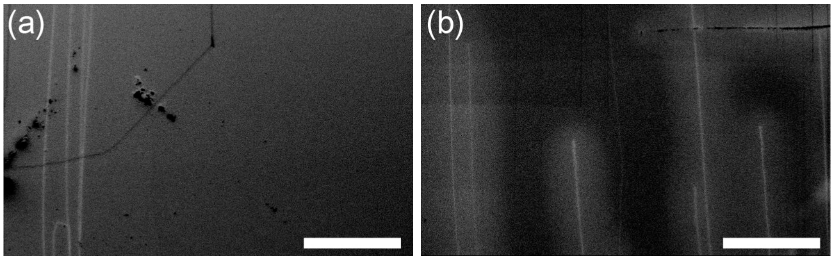

Figure 4.12: SEM image of long CNTs grown on SiO_2/Si substrates. The scale bars are 1 mm.

sccm H_2 reduces the nanoparticles at 750 °C for 80 min. Once the temperature is raised to 890 °C, we pass 40 sccm of Ar and 10 sccm of H_2 through an ethanol bubbler in an ice bath to supply the carbon source for the CNT growth for 40 min. Figure 4.12 shows a typical scanning electron micrograph (SEM) from such a growth. Many of the CNTs are longer than 5 mm and some are reaching 1 cm across the entire substrate.

4.6.2 Fabrication of CNT FETs

Devices on CVD-grown CNTs were fabricated as described in Section 4.2. The CNT FETs fabrication process can be also performed by e-beam lithography using NanoBeam nB5 system. Although one pre-step is required to make global alignment marks on a chip for e-beam lithography method, there are two advantages of this process: 1) it is easier to find the exact location of CNTs by SEM, which allows us to reach higher than 90 % of the fabrication yield. The yield is now limited by the length of a nanotube. 2) The process gives the cleaner surface that only contains PMMA residues compared to the surface covered by residues from four different photoresists. This would also reduce the possible reaction between DNA molecules and polymer residues that may affect the reconnection yield.

4.6.3 Nanogap opening

To create nanogaps in the nanotube, the following additional fabrication step was performed. A 50 nm layer of PMMA was coated on the substrate, and ultra-high resolution (∼10 nm) electron beam lithography was used to open a window in PMMA on each CNT device. The periodic small squares appearing once every four rows (Figure 4.3a) serve as alignment marks for this process. A section of PMMA only a few nanometers in length was exposed with a dose of 1900 $\mu C/cm^2$ at 1 nA current with 80 kV electron beam in a NanoBeam nB5 system. The PMMA was developed by rinsing in methyl isobutyl ketone (MIBK)/isopropanol(IPA) solution (volumetric ratio 1:3) for 45 s followed by rinsing in IPA solution for 15 s. Oxygen plasma with 250 mTorr gas pressure and 50 W power for 3 s was performed through the opened PMMA window to open nanogaps in the CNT. The oxidative plama etch leave carboxylic acids on the two termini of the cut nanotubes,[129] which are later chemically reacted with amine functionalized DNA oligomers. Moreover, we noted that the size of the gap cut in the nanotube was adjusted to fit the length of a given DNA bridge.

4.6.4 DNA sequences

All standard and modified phosphoramidites were purchased from Glen Research. For distance dependence studies, the 40-mer, 60-mer, 80-mer, and 100-mer were designed such that one strand in each duplex carried a C3 linker at each end and the complementary strand was unmodified. The sequences for each length were: (40-mer) 5'-H_2N-$(CH_2)_3$-GGA GCG

CTC CAG CTG TGA CAT ATA AAA GTA GTG AGT CAA T-$(CH_2)_3$-N_2H-3'; (60-mer) 5'-H_2N-$(CH_2)_3$-ATA GGA CAT TGG AGC GCT CCA GCT GTG ACA TAT AAA AGT AGT GAG TCA ATC GTG TAC TGT-$(CH_2)_3$-N_2H-3'; (80-mer) 5'-H_2N-$(CH_2)_3$-TA TCG ACG TCA TAG GAC ATT GGA GCG CTC CAG CTG TGA CAT ATA AAA GTA GTG AGT CAA TCG TGT ACT GTA GTC CAT GTA–$(CH_2)_3$-N_2H-3'; (100-mer) 5'-H_2N-$(CH_2)_3$-AGT ACT GCA GTA TCG ACG TCA TAG GAC ATT GGA GCG CTC CAG CTG TGA CAT ATA AAA GTA GTG AGT CAA TCG TGT ACT GTA GTC CAT GTA TAC TGC ACT A–$(CH_2)_3$-N_2-3'. Note, the 40-mer, 60-mer, and 80-mer sequences are identical to the 100-mer sequence but with 30, 20, and 10 bases, respectively, removed on each end.

4.6.5 Synthesis and purification of DNA

Oligonucleotides were synthesized on an Applied Biosystems 3400 DNA synthesizer using standard reagents. The amine-modified strands were synthesized with 3'-PT-amino-modifier C3 CPG beads to modify the 3' end and a 5'-amino-modifier C3-TFA phosphoramidite to modify the 5' end. The unmodified complement was synthesized using standard reagents and procedures. Both amine-modified and unmodified DNA were cleaved from the solid support and deprotected by treating with concentrated ammonium hydroxide for 8 hours at 60 °C. All DNA was purified by high-performance liquid chromatography (HPLC) on a polymeric PLRP-S column (Agilent) with a 50 mM ammonium acetate buffer/acetonitrile gradient. For the 40-mer, 60-mer, 80-mer, and 100-mer strands, the column was heated to 60 °C to discourage the formation of secondary structures. At least two rounds of HPLC were performed on each DNA type to achieve highly pure samples. After purification, samples were characterized by matrix-assisted laser desorption/ionization time of flight mass spectrometry. DNA stocks were then desalted, resuspended in phosphate buffer (5 mM phosphate, 50 mM NaCl, pH 7), and quantified by UV/Vis absorption at 260 nm according to their extinction coefficients (IDT Oligo Analyzer). To eliminate the possibility of free, single-stranded, amine-modified DNA in the duplex solution, an excess of the unmodified single strand (55 μM) was combined with the amine-modified complement and thermally annealed.

4.6.6 Reconnection of DNA

To prepare the devices for reconnection with DNA, the nanotubes were treated with a 2-(N-morpholino) ethansulfonic acid (MES) buffer solution (0.1 M, pH 4.7) with EDC (5 mM) and Sulfo-NHS (10 mM) for 4-6 hours to activate the carboxylic acid termini inside the CNT gap. The devices were then gently rinsed with MES buffer and dried under air. Following this, the devices were treated with prepared DNA in phosphate buffer solution (0.1 M PBS, 10 μM DNA, pH 7.2) overnight to reconnect the devices with DNA.

4.6.7 Restriction enzyme

As a final confirmation for DNA reconnection in the gap, we can use a restriction enzyme *Alu*I. *Alu*I is known to selectively disconnect duplex DNA with sequence of 5'AGCT and it is a good indicator to verify that the current is flowing only through DNA molecule. One interesting fact is that this reaction is only active in presence of Mg^{2+} ion.

Prior to the restriction enzyme treatment, all of the devices were first treated with Bovine serum albumin (BSA). This is a protein that does not bind DNA and is used frequently in biological experiments to reduce nonspecific binding issues. For BSA treatment, 10 nM solution of BSA was prepared in PBS buffer solution and the chip was incubated in the solution for 1 h at room temperature.

Two stepwise reactions can be tested; the first reaction used *Alu*I without Mg^{2+} and the second reaction used Mg^{2+} containing *Alu*I solution. We expect to observe negligible conductance change with *Alu*I solution without Mg^{2+}. On the other hand, the DNA-bridged CNT device would fully lose its conductance in presence of Mg^{2+} and *Alu*I. The final concentration of Mg^{2+} and *Alu*I are 20 mM and 1,000 units/mL, respectively, in a reaction buffer consisting of 40 mM NaCl, 10 mM Tris-HCl, and 5 mM EDTA at pH 7.9. the chip was incubated in each solution for 2 h at room temperature.

4.6.8 Electrical measurements of CNT FETs devices

The electrical measurements were performed under ambient conditions, with the silicon substrate serving as a global back gate. A semi-automatic probe station (Cascade Microtech Summit 12000B-S) was used to probe on each of the two adjacent electrode pad pairs as source and drain. A semiconductor device analyzer (Agilent 4155C) was used to collect and process electrical data. Three steps of electrical measurement were performed, to measure the devices' conductance before CNT cutting, after CNT cutting, and after DNA reconnection. The conductance change was recorded and plotted in order to examine the effect of fabrication and DNA sensing. In all electrical measurements, bias voltage for all three steps of measurement was 0.05 V. The gate sweep voltage was -10 to 10 V for the first and second measurement steps, and -4 to 4 V for the third measurement step to avoid burning DNA molecules. For the second measurement after cutting, source and drain voltages were also recorded to ensure the good contact between probes and electrode pads.

Bibliography

[1] M. L. Steigerwald, T. Siegrist, and S. M. Stuczynski, Inorg. Chem. **30**, 4940 (1991).

[2] M. L. Steigerwald, Polyhedron **13**, 1245 (1994).

[3] X. Roy, C.-H. Lee, A. C. Crowther, C. L. Schenck, T. Besara, R. A. Lalancette, T. Siegrist, P. W. Stephens, L. E. Brus, P. Kim, M. L. Steigerwald, and C. Nuckolls, Science **341**, 157 (2013).

[4] C.-H. Lee, L. Liu, C. Bejger, A. Turkiewicz, T. Goko, C. J. Arguello, B. A. Frandsen, S. C. Cheung, T. Medina, T. J. S. Munsie, R. D'Ortenzio, G. M. Luke, T. Besara, R. A. Lalancette, T. Siegrist, P. W. Stephens, A. C. Crowther, L. E. Brus, Y. Matsuo, E. Nakamura, Y. J. Uemura, P. Kim, C. Nuckolls, M. L. Steigerwald, and X. Roy, J. Am. Chem. Soc. **136**, 16926 (2014).

[5] A. Turkiewicz, D. W. Paley, T. Besara, G. Elbaz, A. Pinkard, T. Siegrist, and X. Roy, J. Am. Chem. Soc. **136**, 15873 (2014).

[6] D. Wei, Y. Liu, Y. Wang, H. Zhang, L. Huang, and G. Yu, Nano Lett. **9**, 1752 (2009).

[7] W. Chen, S. Chen, C. Q. Dong, Y. G. Xing, and A. T. S. Wee, J. Am. Chem. Soc. **129**, 10418 (2007).

[8] K. P. Loh, Q. Bao, P. K. Ang, and J. Yang, J. Mater. Chem. **20**, 2277 (2010).

[9] B. M. Boardman, J. R. Widawsky, Y. S. Park, C. L. Schenck, L. Venkataraman, M. L. Steigerwald, and C. Nuckolls, J. Am. Chem. Soc. **133**, 8455 (2011).

[10] X. Roy, C. L. Schenck, S. Ahn, R. A. Lalancette, L. Venkataraman, C. Nuckolls, and M. L. Steigerwald, Angew. Chem. Int. Ed. **51**, 12473 (2012).

[11] M. J. Rosseinsky, J. Mater. Chem. **5**, 1497 (1995).

[12] H. Liu, Y. Liu, and D. Zhu, J. Mater. Chem. **21**, 3335 (2011).

[13] W. Xu, T.-s. Lim, H.-k. Seo, S.-y. Min, H. Cho, M.-h. Park, Y.-h. Kim, and T.-w. Lee, Small **10**, 1999 (2014).

[14] I. Jo, Y. Kim, J. Moon, S. Park, J. S. Moon, W. B. Park, J. S. Lee, and B. H. Hong, Phys. Chem. Chem. Phys. **17**, 29492 (2015).

[15] H. M. W. Khalil, M. F. Khan, J. Eom, and H. Noh, ACS Appl. Mater. Interfaces **7**, 23589 (2015).

[16] L. Yang, K. Majumdar, H. Liu, Y. Du, H. Wu, and M. Hatzistergos, Nano Lett. **14**, 6275 (2014).

[17] H. Fang, M. Tosun, G. Seol, T. C. Chang, K. Takei, J. Guo, and A. Javey, Nano Lett. **13**, 1991 (2013).

[18] D. Kiriya, M. Tosun, P. Zhao, J. S. Kang, and A. Javey, J. Am. Chem. Soc. **136**, 7853 (2014).

[19] K. Chen, D. Kiriya, M. Hettick, M. Tosun, T.-J. Ha, S. R. Madhvapathy, S. Desai, A. Sachid, and A. Javey, APL Mater. **2**, 092504 (2014).

[20] S.-H. Jo, D.-H. Kang, J. Shim, J. Jeon, M. H. Jeon, G. Yoo, J. Kim, J. Lee, G. Y. Yeom, S. Lee, H.-Y. Yu, C. Choi, and J.-H. Park, Adv. Mater. **28**, 4824 (2016).

[21] H. Schmidt, F. Giustiniano, and G. Eda, Chem. Soc. Rev. **44**, 7715 (2015).

[22] S. Lei, X. Wang, B. Li, J. Kang, Y. He, A. George, L. Ge, Y. Gong, P. Dong, Z. Jin, G. Brunetto, W. Chen, Z.-T. Lin, R. Baines, D. S. Galvão, J. Lou, E. Barrera, K. Banerjee, R. Vajtai, and P. Ajayan, Nat. Nanotechnol. **11**, 465 (2016).

[23] A. Pospischil, M. M. Furchi, and T. Mueller, Nat. Nanotechnol. **9**, 257 (2014).

[24] B. W. H. Baugher, H. O. H. Churchill, Y. Yang, and P. Jarillo-Herrero, Nat. Nanotechnol. **9**, 262 (2014).

[25] Q. H. Wang, K. Kalantar-Zadeh, A. Kis, J. N. Coleman, and M. S. Strano, Nat. Nanotechnol. **7**, 699 (2012).

[26] K. F. Mak, C. Lee, J. Hone, J. Shan, and T. F. Heinz, Phys. Rev. Lett. **105**, 136805 (2010).

[27] C. Lee, H. Yan, L. E. Brus, T. F. Heinz, J. Hone, and S. Ryu, ACS Nano **4**, 2695 (2010).

[28] W. Zhao, Z. Ghorannevis, L. Chu, M. Toh, C. Kloc, P.-H. Tan, and G. Eda, ACS Nano **7**, 791 (2013).

[29] A. M. van der Zande, P. Y. Huang, D. A. Chenet, T. C. Berkelbach, Y. You, G.-H. Lee, T. F. Heinz, D. R. Reichman, D. A. Muller, and J. C. Hone, Nat. Mater. **12**, 554 (2013).

[30] H. Fang, S. Chuang, T. C. Chang, K. Takei, T. Takahashi, and A. Javey, Nano Lett. **12**, 3788 (2012).

[31] H. Jiang, J. Phys. Chem. C **116**, 7664 (2012).

[32] J. I.-J. Wang, Y. Yang, Y.-A. Chen, K. Watanabe, T. Taniguchi, H. O. H. Churchill, and P. Jarillo-Herrero, Nano Lett. **15**, 1898 (2015).

[33] C. R. Dean, A. F. Young, I. Meric, C. Lee, L. Wang, S. Sorgenfrei, K. Watanabe, T. Taniguchi, P. Kim, K. L. Shepard, and J. Hone, Nat. Nanotechnol. **5**, 722 (2010).

[34] L. Wang, I. Meric, P. Y. Huang, Q. Gao, Y. Gao, H. Tran, T. Taniguchi, K. Watanabe, L. M. Campos, D. A. Muller, J. Guo, P. Kim, J. Hone, K. L. Shepard, and C. R. Dean, Science **342**, 614 (2013).

[35] H. Fang, C. Battaglia, C. Carraro, S. Nemsak, B. Ozdol, J. S. Kang, H. A. Bechtel, S. B. Desai, F. Kronast, A. A. Unal, G. Conti, C. Conlon, G. K. Palsson, M. C. Martin, A. M. Minor, C. S. Fadley, E. Yablonovitch, R. Maboudian, and A. Javey, Proc. Natl. Acad. Sci. U. S. A. **111**, 6198 (2014).

[36] M. S. Choi, D. Qu, D. Lee, X. Liu, K. Watanabe, T. Taniguchi, and W. J. Yoo, ACS Nano **8**, 9332 (2014).

[37] H. Jung, T. Lim, Y. Choi, M. Yi, J. Won, and S. Pyo, Appl. Phys. Lett. **92**, 163504 (2008).

[38] A. K. Geim, and K. S. Novoselov, Nat. Mater. **6**, 183 (2007).

[39] S. Z. Butler, S. M. Hollen, L. Cao, Y. Cui, J. A. Gupta, H. R. Gutiérrez, T. F. Heinz, S. S. Hong, J. Huang, A. F. Ismach, E. Johnston-Halperin, M. Kuno, V. V. Plashnitsa, R. D. Robinson, R. S. Ruoff, S. Salahuddin, J. Shan, L. Shi, M. G. Spencer, M. Terrones, W. Windl, and J. E. Goldberger, ACS Nano **7**, 2898 (2013).

[40] M. Xu, T. Liang, M. Shi, and H. Chen, Chem. Rev. **113**, 3766 (2013).

[41] J. N. Coleman, M. Lotya, A. O'Neill, S. D. Bergin, P. J. King, U. Khan, K. Young, A. Gaucher, S. De, R. J. Smith, I. V. Shvets, S. K. Arora, G. Stanton, H.-Y. Kim, K. Lee, G. T. Kim, G. S. Duesberg, T. Hallam, J. J. Boland, J. J. Wang, J. F. Donegan, J. C. Grunlan, G. Moriarty, A. Shmeliov, R. J. Nicholls, J. M. Perkins, E. M. Grieveson, K. Theuwissen, D. W. McComb, P. D. Nellist, and V. Nicolosi, Science **331**, 568 (2011).

[42] J. Shinar, Z. V. Vardeny, and Z. H. Kafafi, *Optical and Electronic Properties of Fullerenes and Fullerene-Based Materials* (Marcel Dekker Inc., New York, 2000).

[43] F. Diederich, and M. Gómez-López, Chem. Soc. Rev. **28**, 263 (1999).

[44] H. W. Kroto, A. W. Allaf, and S. P. Balm, Chem. Rev. **91**, 1213 (1991).

[45] K. S. Novoselov, D. Jiang, F. Schedin, T. J. Booth, V. V. Khotkevich, S. V. Morozov, and A. K. Geim, Proc. Natl. Acad. Sci. U. S. A. **102**, 10451 (2005).

[46] J. N. Coleman, Adv. Funct. Mater. **19**, 3680 (2009).

[47] D. V. Konarev, S. S. Khasanov, A. Otsuka, M. Maesato, G. Saito, and R. N. Lyubovskaya, Angew. Chem. Int. Ed. **49**, 4829 (2010).

[48] D. V. Konarev, S. S. Khasanov, A. Otsuka, M. Ishikawa, H. Yamochi, G. Saito, and R. N. Lyubovskaya, Inorg. Chem. **53**, 6850 (2014).

[49] C. D. Reddy, Z. G. Yu, and Y.-W. Zhang, Sci. Rep. **5**, 12221 (2015).

[50] L. Sánchez, R. Otero, J. M. Gallego, R. Miranda, and N. Martín, Chem. Rev. **109**, 2081 (2009).

[51] J. G. Hou, J. Yang, H. Wang, Q. Li, C. Zeng, L. Yuan, B. Wang, D. M. Chen, and Q. Zhu, Nature **409**, 304 (2001).

[52] D. Bonifazi, O. Enger, and F. Diederich, Chem. Soc. Rev. **36**, 390 (2007).

[53] D. J. Hornbaker, S.-J. Kahng, S. Misra, B. W. Smith, A. T. Johnson, E. J. Mele, D. E. Luzzi, and A. Yazdani, Science **295**, 828 (2002).

[54] M. Feng, J. Zhao, T. Huang, X. Zhu, and H. Petek, Acc. Chem. Res. **44**, 360 (2011).

[55] W. Xiao, D. Passerone, P. Ruffieux, K. Aït-Mansour, O. Gröning, E. Tosatti, J. S. Siegel, and R. Fasel, J. Am. Chem. Soc. **130**, 4767 (2008).

[56] G.-B. Pan, J.-M. Liu, H.-M. Zhang, L.-J. Wan, Q.-Y. Zheng, and C.-L. Bai, Angew. Chem. Int. Ed. **42**, 2747 (2003).

[57] E. M. Pérez, and N. Martín, Chem. Soc. Rev. **37**, 1512 (2008).

[58] T. Kawase, K. Tanaka, Y. Seirai, N. Shiono, and M. Oda, Angew. Chem. Int. Ed. **42**, 5597 (2003).

[59] N. J. Tremblay, A. A. Gorodetsky, M. P. Cox, T. Schiros, B. Kim, R. Steiner, Z. Bullard, A. Sattler, W.-Y. So, Y. Itoh, M. F. Toney, H. Ogasawara, A. P. Ramirez, I. Kymissis, M. L. Steigerwald, and C. Nuckolls, ChemPhysChem **11**, 799 (2010).

[60] M. Ball, Y. Zhong, Y. Wu, C. Schenck, F. Ng, M. Steigerwald, S. Xiao, and C. Nuckolls, Acc. Chem. Res. **48**, 267 (2015).

[61] S. Lee, Y.-S. Shon, T. R. Lee, and S. S. Perry, Thin Solid Films **358**, 152 (2000).

[62] Y. J. Jeong, D.-J. Yun, J. Jang, S. Park, T. K. An, L. H. Kim, S. H. Kim, and C. E. Park, Phys. Chem. Chem. Phys. **17**, 6635 (2015).

[63] E. Rosencher, and B. Vinter, *Optoelectronics* (Cambridge University Press, Cambridge, 2002).

[64] M. Saba, M. Cadelano, D. Marongiu, F. Chen, V. Sarritzu, N. Sestu, C. Figus, M. Aresti, R. Piras, A. Geddo Lehmann, C. Cannas, A. Musinu, F. Quochi, A. Mura, and G. Bongiovanni, Nat. Commun. **5**, 5049 (2014).

[65] S. Grunder, D. Muñoz Torres, C. Marquardt, A. Błaszczyk, R. Krupke, and M. Mayor, Eur. J. Org. Chem., 478 (2011).

[66] E. Blanc, D. Schwarzenbach, and H. D. Flack, J. Appl. Crystallogr. **24**, 1035 (1991).

[67] R. C. Clark, and J. S. Reid, Acta Crystallogr. Sect. A **A51**, 887 (1995).

[68] G. M. Sheldrick, Acta Crystallogr. Sect. A **A64**, 112 (2008).

[69] G. M. Sheldrick, Acta Crystallogr. Sect. C **C71**, 3 (2015).

[70] L. Palatinus, and G. Chapuis, J. Appl. Crystallogr. **40**, 786 (2007).

[71] O. V. Dolomanov, L. J. Bourhis, R. J. Gildea, J. A. K. Howard, and H. Puschmann, J. Appl. Crystallogr. **42**, 339 (2009).

[72] A. L. Spek, Acta Crystallogr. Sect. D **D65**, 148 (2009).

[73] P. van der Sluis, and A. L. Spek, Acta Crystallogr. Sect. A **A46**, 194 (1990).

[74] Y. Le Page, J. Appl. Crystallogr. **21**, 983 (1988).

[75] I. A. Guzei, J. Appl. Crystallogr. **47**, 806 (2014).

[76] T. T. M. Palstra, M. L. Steigerwald, A. P. Ramirez, Y.-U. Kwon, S. M. Stuczynski, L. F. Schneemeyer, J. V. Waszczak, and J. Zaanen, Phys. Rev. Lett. **71**, 1768 (1993).

[77] H. Kuzmany, M. Matus, B. Burger, and J. Winter, Adv. Mater. **6**, 731 (1994).

[78] M. Walter, J. Akola, O. Lopez-Acevedo, P. D. Jadzinsky, G. Calero, C. J. Ackerson, R. L. Whetten, H. Gronbeck, and H. Häkkinen, Proc. Natl. Acad. Sci. U. S. A. **105**, 9157 (2008).

[79] S. N. Khanna, and P. Jena, Phys. Rev. B **51**, 13705 (1995).

[80] Z. Luo, and A. W. Castleman, Acc. Chem. Res. **47**, 2931 (2014).

[81] E. G. Tulsky, N. R. M. Crawford, S. A. Baudron, P. Batail, and J. R. Long, J. Am. Chem. Soc. **125**, 15543 (2003).

[82] B. Choi, J. Yu, D. W. Paley, M. T. Trinh, M. V. Paley, J. M. Karch, A. C. Crowther, C.-H. Lee, R. A. Lalancette, X. Zhu, P. Kim, M. L. Steigerwald, C. Nuckolls, and X. Roy, Nano Lett. **16**, 1445 (2016).

[83] A. M. Champsaur, A. Velian, D. W. Paley, B. Choi, X. Roy, M. L. Steigerwald, and C. Nuckolls, Nano Lett. **16**, 5273 (2016).

[84] B. Yoon, W. D. Luedtke, R. N. Barnett, J. Gao, A. Desireddy, B. E. Conn, T. Bigioni, and U. Landman, Nat. Mater. **13**, 807 (2014).

[85] H. Li, M. Eddaoudi, M. O'Keeffe, and O. M. Yaghi, Nature **402**, 276 (1999).

[86] J. Jia, F. Sun, Q. Fang, X. Liang, K. Cai, Z. Bian, H. Zhao, L. Gao, and G. Zhu, Chem. Commun. **47**, 9167 (2011).

[87] J. R. Long, and O. M. Yaghi, Chem. Soc. Rev. **38**, 1213 (2009).

[88] H. Furukawa, K. E. Cordova, M. O'Keeffe, and O. M. Yaghi, Science **341**, 1230444 (2013).

[89] M. P. Shores, L. G. Beauvais, and J. R. Long, J. Am. Chem. Soc. **121**, 775 (1999).

[90] S. M. Humphrey, P. K. Allan, S. E. Oungoulian, M. S. Ironside, and E. R. Wise, Dalton Trans., 2298 (2009).

[91] N. Ding, G. S. Armatas, and M. G. Kanatzidis, J. Am. Chem. Soc. **132**, 6728 (2010).

[92] M. C. Das, S. Xiang, Z. Zhang, and B. Chen, Angew. Chem. Int. Ed. **50**, 10510 (2011).

[93] G.-L. Zhuang, W.-X. Chen, H.-X. Zhao, X.-J. Kong, L.-S. Long, R.-B. Huang, and L.-S. Zheng, Inorg. Chem. **50**, 3843 (2011).

[94] S.-T. Zheng, X. Zhao, S. Lau, A. Fuhr, P. Feng, and X. Bu, J. Am. Chem. Soc. **135**, 10270 (2013).

[95] D. Sheberla, L. Sun, M. A. Blood-Forsythe, S. Er, C. R. Wade, C. K. Brozek, A. Aspuru-Guzik, and M. Dincă, J. Am. Chem. Soc. **136**, 8859 (2014).

[96] L. Sun, C. H. Hendon, M. A. Minier, A. Walsh, and M. Dincă, J. Am. Chem. Soc. **137**, 6164 (2015).

[97] J.-S. Qin, D.-Y. Du, W. Guan, X.-J. Bo, Y.-F. Li, L.-P. Guo, Z.-M. Su, Y.-Y. Wang, Y.-Q. Lan, and H.-C. Zhou, J. Am. Chem. Soc. **137**, 7169 (2015).

[98] L. E. Darago, M. L. Aubrey, C. J. Yu, M. I. Gonzalez, and J. R. Long, J. Am. Chem. Soc. **137**, 15703 (2015).

[99] S. Li, Y.-S. Chen, and K. L. Mulfort, CrystEngComm **17**, 1005 (2015).

[100] H. L. Nguyen, F. Gándara, H. Furukawa, T. L. H. Doan, K. E. Cordova, and O. M. Yaghi, J. Am. Chem. Soc. **138**, 4330 (2016).

[101] I.-R. Jeon, and T. D. Harris, Chem. Commun. **52**, 1006 (2016).

[102] D. M. D'Alessandro, Chem. Commun. **52**, 8957 (2016).

[103] L. Sun, M. G. Campbell, and M. Dincă, Angew. Chem. Int. Ed. **55**, 3566 (2016).

[104] O. Shekhah, J. Liu, R. A. Fischer, and C. Wöll, Chem. Soc. Rev. **40**, 1081 (2011).

[105] P. Falcaro, R. Ricco, C. M. Doherty, K. Liang, A. J. Hill, and M. J. Styles, Chem. Soc. Rev. **43**, 5513 (2014).

[106] L. Hou, J.-P. Zhang, and X.-M. Chen, Cryst. Growth Des. **9**, 2415 (2009).

[107] A. D. Martin, T. L. Easun, S. P. Argent, W. Lewis, A. J. Blake, and M. Schröder, CrystEngComm **19**, 603 (2017).

[108] I. J. Bruno, J. C. Cole, P. R. Edgington, M. Kessler, C. F. Macrae, P. McCabe, J. Pearson, and R. Taylor, Acta Crystallogr. Sect. B **58**, 389 (2002).

[109] S. Vagin, A. Ott, H.-C. Weiss, A. Karbach, D. Volkmer, and B. Rieger, Eur. J. Inorg. Chem., 2601 (2008).

[110] M. Onoda, X.-A. Chen, K. Kato, A. Sato, and H. Wada, Acta Crystallogr. Sect. B **B55**, 721 (1999).

[111] S. Iijima, Nature **354**, 56 (1991).

[112] H. T. Soh, C. F. Quate, A. F. Morpurgo, C. M. Marcus, J. Kong, and H. Dai, Appl. Phys. Lett. **75**, 627 (1999).

[113] P. L. McEuen, M. Bockrath, D. H. Cobden, Y.-G. Yoon, and S. G. Louie, Phys. Rev. Lett. **83**, 5098 (1999).

[114] C. Zhou, J. Kong, and H. Dai, Appl. Phys. Lett. **76**, 1597 (2000).

[115] A. Bachtold, P. Hadley, T. Nakanishi, and C. Dekker, Science **294**, 1317 (2001).

[116] A. Javey, M. Shim, and H. Dai, Appl. Phys. Lett. **80**, 1064 (2002).

[117] A. Jorio, G. Dresselhaus, and M. S. Dresselhaus, *Carbon Nanotubes: Advanced Topics in the Synthesis, Structure, Properties and Applications* (Springer, New York, 2008).

[118] R. Martel, T. Schmidt, H. R. Shea, T. Hertel, and P. Avouris, Appl. Phys. Lett. **73**, 2447 (1998).

[119] S. J. Tans, A. R. M. Verschueren, and C. Dekker, Nature **393**, 49 (1998).

[120] Z. Chen, J. Appenzeller, Y.-M. Lin, J. Sippel-Oakley, A. G. Rinzler, J. Tang, S. J. Wind, P. M. Solomon, and P. Avouris, Science **311**, 1735 (2006).

[121] Y.-C. Tseng, P. Xuan, A. Javey, R. Malloy, Q. Wang, J. Bokor, and H. Dai, Nano Lett. **4**, 123 (2004).

[122] B. Lassagne, Y. Tarakanov, J. Kinaret, D. Garcia-Sanchez, and A. Bachtold, Science **325**, 1107 (2009).

[123] G. Gruner, Anal. Bioanal. Chem. **384**, 322 (2006).

[124] Z. C. Sánchez-Acevedo, J. Riu, and F. X. Rius, Biosens. Bioelectron. **24**, 2842 (2009).

[125] M. T. Martínez, Y.-C. Tseng, N. Ormategui, I. Loinaz, R. Eritja, and J. Bokor, Nano Lett. **9**, 530 (2009).

[126] P. Li, N. Lei, D. A. Sheadel, J. Xu, and W. Xue, Sens. Actuators B **166-167**, 870 (2012).

[127] J. Zhao, A. Hashmi, J. Xu, and W. Xue, Appl. Phys. Lett. **100**, 243109 (2012).

[128] W. Yang, P. Thordarson, J. J. Gooding, S. P. Ringer, and F. Braet, Nanotechnology **18**, 412001 (2007).

[129] X. Guo, J. P. Small, J. E. Klare, Y. Wang, M. S. Purewal, I. W. Tam, B. H. Hong, R. Caldwell, L. Huang, S. O'Brien, J. Yan, R. Breslow, S. J. Wind, J. Hone, P. Kim, and C. Nuckolls, Science **311**, 356 (2006).

[130] X. Guo, A. A. Gorodetsky, J. Hone, J. K. Barton, and C. Nuckolls, Nat. Nanotechnol. **3**, 163 (2008).

[131] L. S. Liyanage, H. Lee, N. Patil, S. Park, S. Mitra, Z. Bao, and H.-S. P. Wong, ACS Nano **6**, 451 (2012).

[132] E. S. Snow, J. P. Novak, P. M. Campbell, and D. Park, Appl. Phys. Lett. **82**, 2145 (2003).

[133] I. Martin-Fernandez, M. Sansa, M. J. Esplandiu, E. Lora-Tamayo, F. Perez-Murano, and P. Godignon, Microelectron. Eng. **87**, 1554 (2010).

[134] X. Wang, Q. Li, J. Xie, Z. Jin, J. Wang, Y. Li, K. Jiang, and S. Fan, Nano Lett. **9**, 3137 (2009).

[135] M. S. Purewal, B. H. Hong, A. Ravi, B. Chandra, J. Hone, and P. Kim, Phys. Rev. Lett. **98**, 186808 (2007).

[136] A. Müller, S. K. Das, P. Kögerler, H. Bögge, M. Schmidtmann, A. X. Trautwein, V. Schunemann, E. Krickemeyer, and W. Preetz, Angew. Chem. Int. Ed. **39**, 3413 (2000).

[137] L. An, J. M. Owens, L. E. McNeil, and J. Liu, J. Am. Chem. Soc. **124**, 13688 (2002).

[138] A. Javey, J. Guo, Q. Wang, M. Lundstrom, and H. Dai, Nature **424**, 654 (2003).

[139] D. Mann, A. Javey, J. Kong, Q. Wang, and H. Dai, Nano Lett. **3**, 1541 (2003).

[140] B. Chandra, V. Perebeinos, S. Berciaud, J. Katoch, M. Ishigami, P. Kim, T. F. Heinz, and J. Hone, Phys. Rev. Lett. **107**, 146601 (2011).

[141] Q. Cao, S.-J. Han, G. S. Tulevski, A. D. Franklin, and W. Haensch, ACS Nano **6**, 6471 (2012).

[142] N. B. Muren, E. D. Olmon, and J. K. Barton, Phys. Chem. Chem. Phys. **14**, 13754 (2012).

[143] J. D. Slinker, N. B. Muren, S. E. Renfrew, and J. K. Barton, Nat. Chem. **3**, 228 (2011).

[144] S. O. Kelley, R. E. Holmlin, E. D. A. Stemp, and J. K. Barton, J. Am. Chem. Soc. **119**, 9861 (1997).

[145] S. O. Kelley, and J. K. Barton, Science **283**, 375 (1999).

[146] E. M. Boon, J. E. Salas, and J. K. Barton, Nat. Biotechnol. **20**, 282 (2002).

[147] H. Wang, N. B. Muren, D. Ordinario, A. A. Gorodetsky, J. K. Barton, and C. Nuckolls, Chem. Sci. **3**, 62 (2012).

[148] J. C. Genereux, A. K. Boal, and J. K. Barton, J. Am. Chem. Soc. **132**, 891 (2010).

[149] P. A. Sontz, N. B. Muren, and J. K. Barton, Acc. Chem. Res. **45**, 1792 (2012).

[150] C. J. Murphy, M. R. Arkin, Y. Jenkins, N. D. Ghatlia, S. H. Bossmann, N. J. Turro, and J. K. Barton, Science **262**, 1025 (1993).

[151] S. O. Kelley, E. M. Boon, J. K. Barton, N. M. Jackson, and M. G. Hill, Nucleic Acids Res. **27**, 4830 (1999).

[152] X. Guo, M. Myers, S. Xiao, M. Lefenfeld, R. Steiner, G. S. Tulevski, J. Tang, J. Baumert, F. Leibfarth, J. T. Yardley, M. L. Steigerwald, P. Kim, and C. Nuckolls, Proc. Natl. Acad. Sci. U. S. A. **103**, 11452 (2006).

[153] A. K. Feldman, M. L. Steigerwald, X. Guo, and C. Nuckolls, Acc. Chem. Res. **41**, 1731 (2008).

[154] S. Roy, H. Vedala, A. D. Roy, D.-h. Kim, M. Doud, K. Mathee, H.-k. Shin, N. Shimamoto, V. Prasad, and W. Choi, Nano Lett. **8**, 26 (2008).

[155] S. Liu, G. H. Clever, Y. Takezawa, M. Kaneko, K. Tanaka, X. Guo, and M. Shionoya, Angew. Chem. Int. Ed. **50**, 8886 (2011).

[156] E. Penzo, M. Palma, R. Wang, H. Cai, M. Zheng, and S. J. Wind, Nano Lett. **15**, 6547 (2015).

[157] S. H. Choi, B. Kim, and C. D. Frisbie, Science **320**, 1482 (2008).

[158] N. Tuccitto, V. Ferri, M. Cavazzini, S. Quici, G. Zhavnerko, A. Licciardello, and M. A. Rampi, Nat. Mater. **8**, 41 (2009).

[159] R. Søndergaard, S. Strobel, E. Bundgaard, K. Norrman, A. G. Hansen, E. Albert, G. Csaba, P. Lugli, M. Tornow, and F. C. Krebs, J. Mater. Chem. **19**, 3899 (2009).

[160] F. Chen, and N. J. Tao, Acc. Chem. Res. **42**, 429 (2009).

[161] Q. Lu, K. Liu, H. Zhang, Z. Du, X. Wang, and F. Wang, ACS Nano **3**, 3861 (2009).

[162] Z.-L. Cheng, R. Skouta, H. Vazquez, J. R. Widawsky, S. Schneebeli, W. Chen, M. S. Hybertsen, R. Breslow, and L. Venkataraman, Nat. Nanotechnol. **6**, 353 (2011).

[163] D. Bouilly, J. Hon, N. S. Daly, S. Trocchia, S. Vernick, J. Yu, S. Warren, Y. Wu, R. L. Gonzalez, K. L. Shepard, and C. Nuckolls, Nano Lett. **16**, 4679 (2016).

[164] M. Palma, W. Wang, E. Penzo, J. Brathwaite, M. Zheng, J. Hone, C. Nuckolls, and S. J. Wind, J. Am. Chem. Soc. **135**, 8440 (2013).

[165] J. Zhu, J. McMorrow, R. Crespo-Otero, G. Ao, M. Zheng, W. P. Gillin, and M. Palma, J. Am. Chem. Soc. **138**, 2905 (2016).

[166] H. Li, B. C.-K. Tee, J. J. Cha, Y. Cui, J. W. Chung, S. Y. Lee, and Z. Bao, J. Am. Chem. Soc. **134**, 2760 (2012).

[167] L. Venkataraman, J. E. Klare, I. W. Tam, C. Nuckolls, M. S. Hybertsen, and M. L. Steigerwald, Nano Lett. **6**, 458 (2006).

[168] T. Kim, Z.-F. Liu, C. Lee, J. B. Neaton, and L. Venkataraman, Proc. Natl. Acad. Sci. U. S. A. **111**, 10928 (2014).

[169] S. Kubatkin, A. Danilov, M. Hjort, J. Cornil, J.-L. Brédas, N. Stuhr-Hansen, P. Hedegård, and T. Bjørnholm, Nature **425**, 698 (2003).

[170] E. A. Osorio, K. O'Neill, N. Stuhr-Hansen, O. F. Nielsen, T. Bjømholm, and H. S. J. van der Zant, Adv. Mater. **19**, 281 (2007).

[171] F. Prins, A. Barreiro, J. W. Ruitenberg, J. S. Seldenthuis, N. Aliaga-Alcalde, L. M. K. Vandersypen, and H. S. J. van der Zant, Nano Lett. **11**, 4607 (2011).

[172] E. Penzo, M. Palma, D. A. Chenet, G. Ao, M. Zheng, J. C. Hone, and S. J. Wind, ACS Nano **10**, 2975 (2016).

Appendix: Molecular devices using solution-processable carbon nanoelectrodes

A.1 Motivation

In Chapter 4, we discussed fabrication of molecular devices via top-down approach (Figure 4.6 in Section 4.4): CNT FETs were prepared prior to the formation of molecular junctions and nanogap electrodes were fabricated by e-beam lithography. Here, we describe the bottom-up approach to fabricate molecular devices using solution-processable carbon nanoelectrodes.[4]

Palma *et al.* reported the controlled formation of CNT junctions by varying the geometry of the linkers.[164] This approach used single-stranded DNA wrapped CNTs and these nanotubes were functionalized with diamine molecular bridges in aqueous solution. In par-

---

[4] I performed device fabrication, AFM characterization, and electrical measurements with assistance from Delphine Bouilly and Campbell Weaver. Solution-based assemblies of CNT junctions were prepared by Matteo Palma group.

APPENDIX: MOLECULAR DEVICES USING SOLUTION-PROCESSABLE CARBON NANOELECTRODES

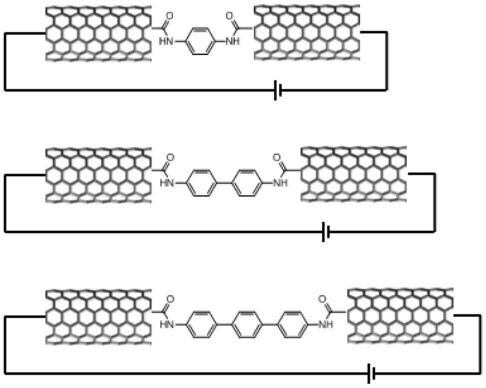

Figure A.1: Diagram illustraing oligopheneylene molecular junctions bridging CNT nanoelectrodes.

ticular, they presented linear end-to-end CNT junctions using hexamethylenediamine as a molecular linker, confirmed by increased total lengths of nanotube assemblies. Furthermore, a recent study shows that this solution-based assembly method can be applied to study single molecule conductance.[165].

In collaboration with Palma group, we utilize the method to fabricate solid-state molecular devices, which allows us to understand conductivity of individual molecules as well as to achieve miniaturization of electronic devices. The top-down etching approach limits the nanogap size as small as ∼10 nm, which is the resolution of e-beam writer. In contrast, the bottom-up assembly approach can employ any short lengths of target molecules. In addition, density functional theory (DFT) calculations in previous literature[165] shows that single molecule junctions are predominant because the formation of two molecular bridges to two CNTs is energetically and entropically unfavorable.

Figure A.1 is the schematics of molecular devices formed using oligophenylenes and carbon nanotubes. For this application, the metallic CNTs are preferred for the same reason as mentioned in Section 4.4. The metallic nanotubes are less resistive than the semiconducting ones and they show the continuous "on" behavior over the whole gate voltage range.

A.2 Design and fabrication of molecular devices

Figure A.2 shows the design of electrode arrays to fabricate FETs on top of nanotube assemblies. This design contains around 1100 devices on each chip, with 20 rows and 56 columns. The array is diagonally divided into four sections, and each section has either vertical or horizontal alignment of electrodes (Figures A.2c and A.2d) to adapt directionality of nanotube assemblies resulted from drying of a droplet.[166] The width and length of each channel are defined as 650 nm and 700 nm, respectively. Specifically, the channel length is determined based on the length of unreacted CNTs ($\sim$500 nm).

The fabrication process for oligophenylene-bridged CNT FETs generally consists of four steps: 1) thermal annealing of drop-casted CNT junctions, 2) fabrication of electrode arrays, 3) isolation of the channel area, and 4) thermal annealing of the final devices.

The solution-based CNT junctions were prepared and drop-casted on the 1×1 cm^2 SiO_2/Si substrate as described previously.[165] First, the chip was thermally annealed at 100 °C under inert gas flow. For the solution-based assembly method, we used single-stranded DNA wrapped CNTs to disperse in water. The DNA-assisted dispersion enables separation of nanotubes by chirality and lengths. However, the DNA interferes the contact between metal and nanotubes, resulting in high contact resistance. The first annealing step before lithography process leads a significant increase in the number of working devices. Figure A.3 shows the current histogram of biphenyl-bridged CNT FETs. The working devices are

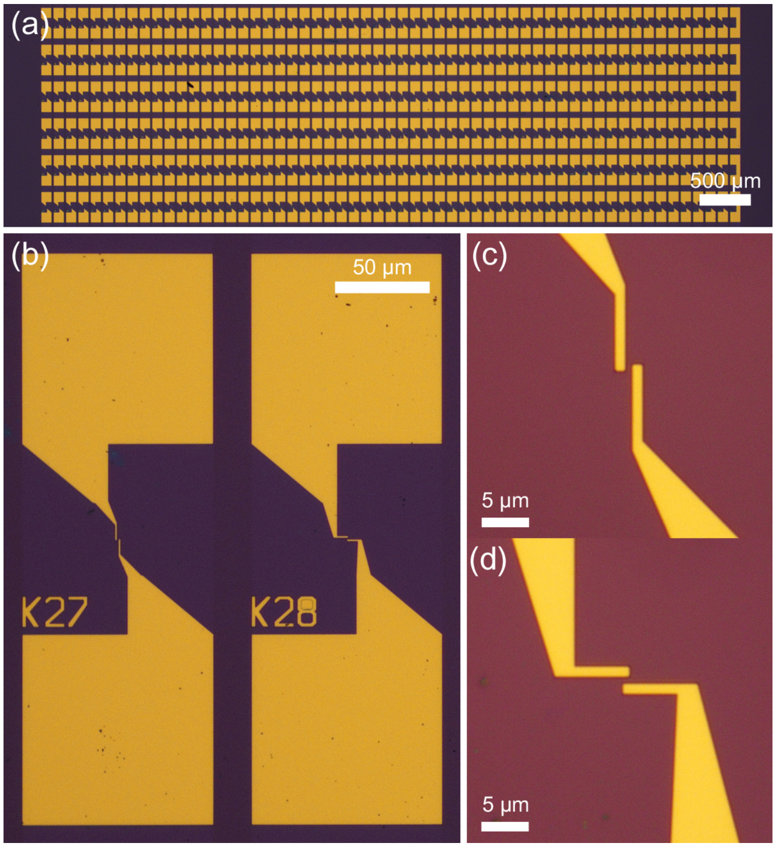

Figure A.2: (a) Optical image of the device arrays for single molecule transistors and (b,c) the zoom-in images of two types of the electrode pattern.

defined as the devices exhibit the current higher than 1×10^{-14} A. As two graphs illustrate, almost twice of working devices are fabricated in the chip with the thermal treatment. This indicates that the first thermal annealing step helps the improvement of contact resistances.

The following e-beam lithography step was performed to fabricate electrode arrays. PMMA 495k (200 nm) and PMMA 950k (100 nm) were spin-coated on the substrate. The double layer of PMMA films provides an undercut profile. The electrodes were patterned us-

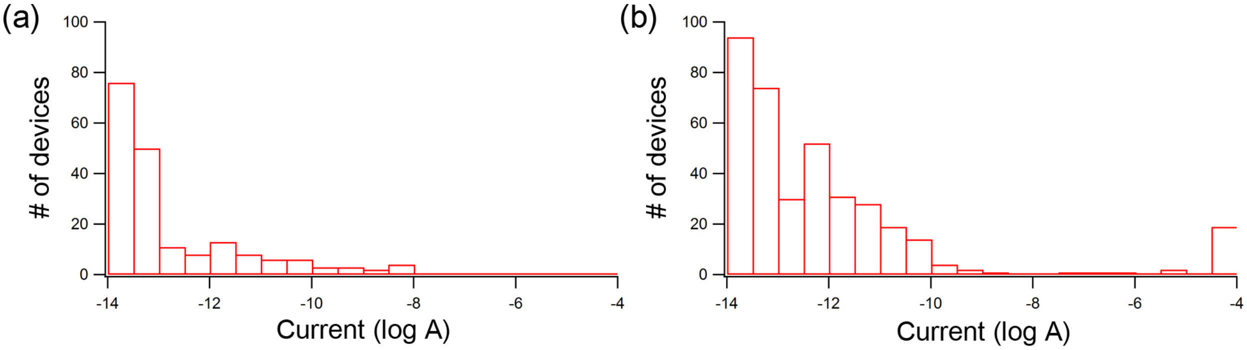

Figure A.3: Current histogram of biphenyl-bridged CNT FETs for a comparison of the first thermal annealing step. (a) The chip is fabricated without the thermal treatment and the number of devices recorded current higher than 10^{-14} A is 190 (out of 1120). (b) The other chip is thermally annealed prior to the electrode fabrication and the number of devices is 373 (out of devices).

ing NanoBeam nB5 system. The PMMA was developed by rinsing in isopropanol/DI water solution (volumetric ratio 3:1) for 2 min followed by rinsing in DI water for 15 s, with temperature below 10 °C. After development, the electrodes were formed by depositing Ti(0.5 nm)/Pd(20 nm)/Au(50 nm) by e-beam evaporation system. As mentioned in Section 4.2, Ti is applied for an adhesive layer, Pd for a good contacting layer to CNT,[138, 139] and Au as a protective layer. The lift-off was done in Remover PG at 80 °C for 1 h and in acetone at room temperature overnight.

The second e-beam lithography step was performed to confine the channel area. Some nanotube assemblies aggregate each other during drying of a droplet of the solution. This isolation step is essential to prevent false results from these CNT bundles. Particularly, CNT junctions formed with p-terphenyl linkers are likely to aggregate via van der Waals interactions among linkers as well as towards nanotubes. The current of fabricated devices without the isolation step exhibits broad distribution from 10^{-12} to 10^{-10} A. After burning extra CNT connections, most of devices recorded current higher than 10^{-11} A are eliminated. The substrate was spin-coated with PMMA (200 nm), and e-beam lithography was used to open windows in PMMA on each device. The PMMA was developed by rinsing in MIBK/IPA solution (volumetric ratio 3:1) for 3 min followed by rinsing in IPA for 15 s. The opened PMMA window was treated with O_2 plasma with 250 mTorr gas pressure and 50 W power for 20 s. The resist layer was removed in Remover PG at 80 °C for 1 h and in acetone at room temperature overnight. The final devices were further annealed at 200 °C under inert gas flow.

A.3 Electrical characteristics of molecular devices

The electrical measurements were conducted under ambient conditions. A semi-automatic probe station (Cascade Microtech Summit 12000B-S) and a semiconductor device analyzer (Agilent 4155C) were used to probe transistors and to collect electrical data. We performed two steps of electrical measurements. First, a single sweep measurement was performed on all devices. A double sweep measurement was then conducted on selected working devices, whose maximum current lies between 5×10^{-14} A and 1×10^{-5} A. For transfer characteristics, the gate sweep voltage was -20 to 20 V and the bias voltages were 0 V and 0.3 V. For output characteristics, the source-drain voltage was -1 to 1 V at the gate voltage of -20 V.

Figure A.4 displays the current histograms of oligophenylene-bridged CNT FETs. Although each device might have multiple junctions in a channel, a series of current histograms

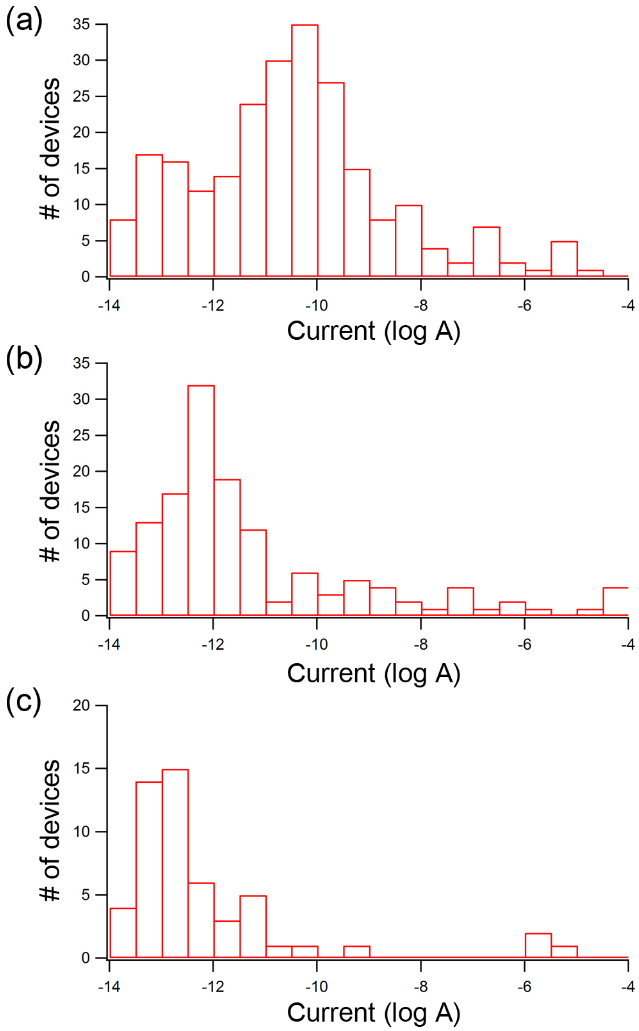

Figure A.4: Current histograms of oligophenylene-bridged CNT FETs: (a) monophenyl, (b) biphenyl, and (c) p-terphenyl linkers. The numbers of working devices formed with oligophenylene linkers are 238, 138, and 53 (out of 1120), respectively.

statistically demonstrates the decrease of conductance as the length of molecule increases. The peak of the number of devices shifts from 10^{-10} A for a monophenyl linker to 10^{-12} A for a biphenyl one, and finally to 10^{-13} A for a terphenyl bridge. To confirm a single molecule junction in a channel, we characterized individual devices in a range of the peak shown in the current histogram (Figure A.4) using AFM.

AFM image in the inset of Figure A.5b presents the single molecular junction within the channel of the device. The transfer and output characteristics of this device are shown in Figures A.5a and A.5b. These graphs also depict the effect of the second thermal annealing step after device fabrication. This improvement in conductance with thermal annealing is attributed to the removal of resists residues from fabrication steps. Nevertheless, the molecular device still exhibits high charge injection barrier (Figure A.5b).

The resistance of the biphenyl-bridged CNT FET is calculated from the current value at V_{ds} = 0.5 V and V_g = -20 V. The resistance is 1.21 GΩ and it is converted to multiples of the quantum conductance (G_0) as 1.07×10^{-5} using $G_0 = 2e^2/h$, where h is Planck's constant.[167] This value is plotted with reported values of oligophenylene junctions (Figure A.5d).[165, 167, 168] The black and red curves show the single molecule conductance results measured by scanning-tunneling-microscope-based break-junction (STM-BJ) technique. The black curve presents the data using typical Au electrodes,[167] While the red curve depicts the data from graphite/oligophenyl diamine/Au molecular junctions.[168] Additionally, the conductance of a series of oligophenyls was measured using conductive AFM (green curve in Figure A.5d).[165] Our value lies within the range of the reported values from various measurement platforms, showing that our CNT FET platform has a potential for basic molecular studies.

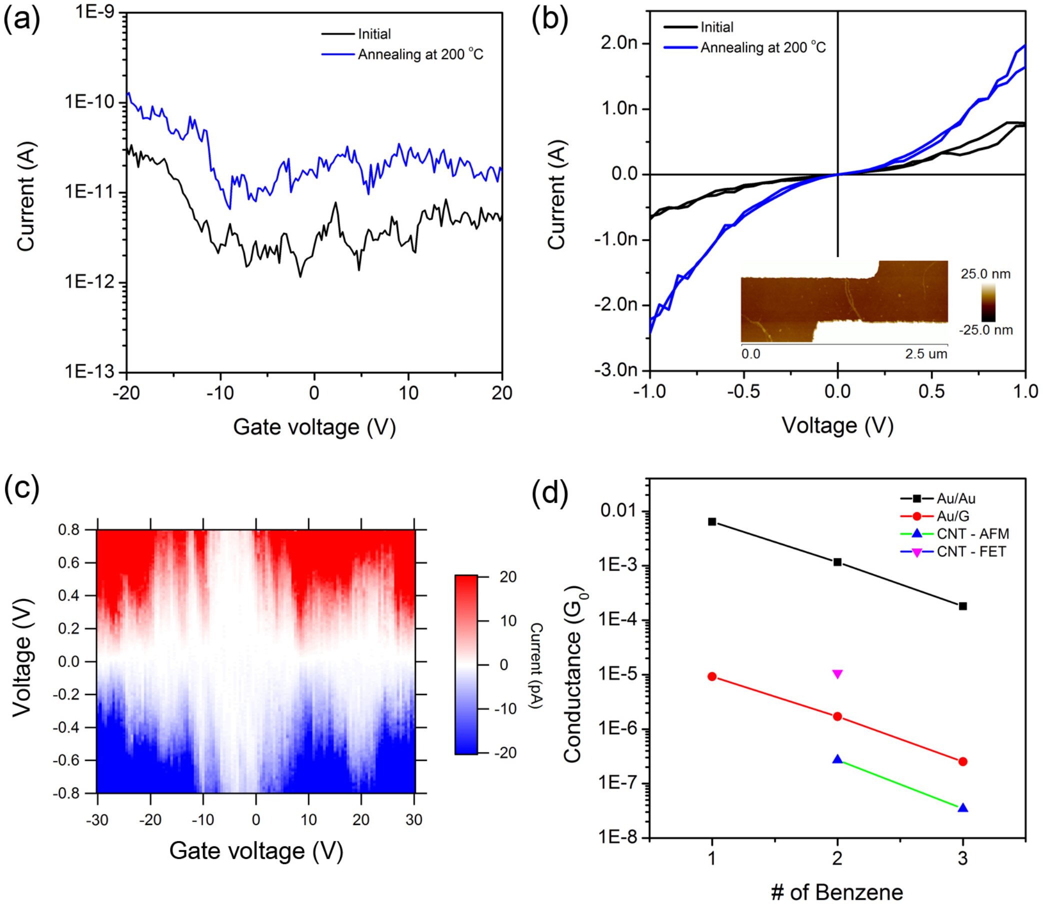

Figure A.5: (a) Transfer and (b) output characteristics of a biphenyl-bridged CNT FET. The black curve and the blue curve represent before and after the second thermal annealing step. The inset in (b) illustrates the single junction within the channel. (c) Current map of the device as a function of source-drain bias voltage and gate voltage, measured at 100 K in vacuum. (d) Comparison of the conductance measured with previously reported data.

We further studied the gate-dependent transport of biphenyl-reconnected device at low temperature in vacuum. Current measurements were conducted in a vacuum cryogenic probe station (Lakeshore TTP4), using a current preamplifier (Stanford Research System SR570) and a digital multimeter (Keysight 34401A). Computer-controlled source units were used to apply DC potentials (Yokogawa 7651 for source-drain bias and Keithley 2400 for gate bias). All device measurements were performed in vacuum ($P < 1 \times 10^{-4}$ Torr) at 100 K using liquid nitrogen cooling. The gate sweep voltage was -30 to 30 V with 0.5 V steps and the source-drain voltage was -0.8 to 0.8 V at each gate voltage.

Figure A.5c shows a 2D plot of the current for the biphenyl-bridged CNT FET as a function of the source-drain bias and the gate voltage. This map illustrates that the electrical current of the molecule is dependent on the gate voltage. In the white regions, charge transport is blocked due to the discrete electronic states in the molecule. In contrast, single-electron tunneling occurs when one state aligns within the source and drain energy separation (in the red and blue regions in Figure A.5c). These gate-dependent characteristics are typical of the Coulomb blockade effect in single-electron transistors.[169–171] The diamond-shaped domains are linked to the electronic states of the molecule. However, the result is unclear to further analyze the number of states and the addition energy.

A.4 Conclusion and future direction

We have demonstrated a new platform for single molecule studies using solution-processable CNT electrodes. The target molecules were covalently bonded to CNTs in aqueous solution and the molecular devices were fabricated on top of these end-to-end CNT assemblies. The

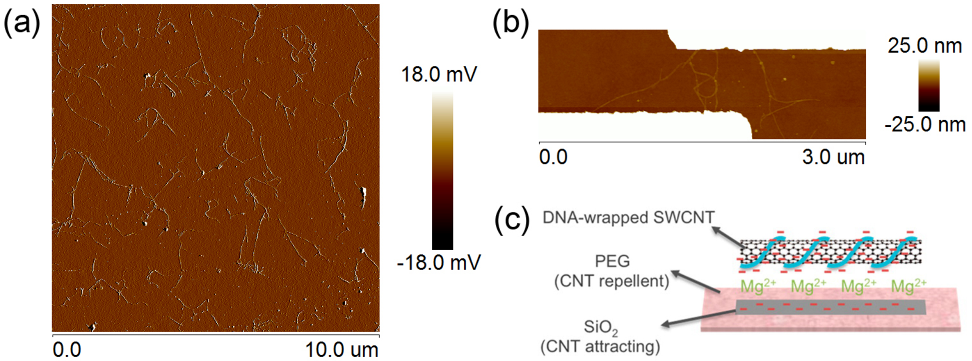

Figure A.6: (a) AFM peak force error image of as-prepared CNT assemblies. (b) AFM height sensor image of a typical device of multiple junctions within the channel. (c) Schematic illustration of the DNA-wrapped CNT binding to the hydrophilic line patterned on the PEG passivated SiO_2 substrate. Adapted from Ref. [172].

current histograms of oligophenyl-bridged CNT FETs show that the conductance decreases as the length of target molecule increases. Furthermore, we observed the gate-dependent Coulomb blockade features in the biphenyl-reconnected device, indicating single-electron tunneling in the molecular junction.

This platform has a great potential for basic molecular studies of a variety of organic molecules. However, the yield of single molecule devices is only 0.4 % (1 out of 247 devices). This low yield has mainly resulted from multiple junctions within the channel shown in Figure A.6b. Previously, the nanotube assemblies have shown ring-like structures by van der Waals interactions or hydrogen bonding among linkers bridging CNTs.[164] Although the linear assemblies are dominant with oligophenyl linkers, there are ring-like structures and some aggregation of CNTs observed in a chip (Figure A.6a). The orientation of CNT assemblies is also hard to control by the drop-casting method, which results in significantly low fabrication yield. Hence, we plan to modify the fabrication method. Penzo *et al.* have developed a technique that can directly assemble DNA-wrapped CNTs on hydrophilic lines patterned on a passivated SiO_2/Si substrate, illustrating in Figure A.6c.[172] We can utilize this technique instead of simple drop-casting of a sample solution on a chip that we applied for our current platform. With the addition of this lithography step, it will make our measurement platform robust and reliable with high fabrication yield. This improved platform will enable the miniaturization of transistors and it should be useful for integrated circuits.